

CO₂ Laser Induced Structural Changes of Dental Enamel

DISSERTATION

Submitted for the Doctorate Degree of Natural Sciences
at the Department of Earth Sciences of the University of Hamburg

By

SHENGQIANG ZHANG

From Heilongjiang, P. R. China

Hamburg 2008

The first referee: Prof. Dr. Ulrich Bismayer

The second referee: Prof. Dr. Arndt Klocke

Date of the final oral examination: 30.05.2008

Contents

Abstract

Chapter 1 Dental enamel and calcium phosphate

1.1 Tooth and enamel	1
1.1.1 Histological structural components of teeth	1
1.1.2 Chemical structure of teeth	2
1.1.3 Enamel formation	3
1.2 Enamel apatite	4
1.2.1 Structure of hydroxyapatite	4
1.2.2 Substitution of hydroxyapatite	7
1.2.3 Structure of enamel apatite	9
1.2.4 Other related calcium phosphate minerals	10

Chapter 2 Dental lasers: background and application

2.1 Laser application in dental practice	15
2.1.1 Diagnostic laser applications	15
2.1.2 Photochemical laser effects	16
2.1.3 Laser applications in the dental laboratory	17
2.1.4 Laser procedures on dental hard tissues	18
2.1.5 Soft tissue laser procedures	20
2.1.6 Other applications	21
2.2 Types of lasers	21

2.2.1 Classification	21
2.2.2 Laser type according to wavelength	21
2.3 Effect of laser treatment on enamel	24
2.3.1 Interaction of laser and enamel	24
2.3.2 Laser operating parameters	26
2.3.3 Morphological changes of enamel after laser irradiation	27
2.3.4 Chemical and structural change of enamel after laser irradiation	28
Aims of this study	30
Chapter 3 Materials and methods	
3.1 Principles of analytical methods	32
3.1.1 X-ray powder diffraction	32
3.1.2 Vibrational spectroscopy	34
3.1.2.1 Origins of infrared and Raman spectroscopy	35
3.1.2.2 Vibrational theory of molecules and crystals	37
3.1.2.3 Selection rules for infrared and Raman spectra	38
3.1.2.4 Comparison of infrared and Raman spectroscopy	39
3.1.2.5 Fourier transform infrared (FTIR) spectroscopy	40
3.1.2.6 Attenuated total reflectance infrared spectroscopy (ATR-IR)	40
3.2 Materials	42
3.2.1 Reference samples	42
3.2.2 Dental enamel	42

3.3 Laser treatment	43
3.3.1 Technical specification of the CO ₂ laser	43
3.3.2 Laser irradiation parameters	44
3.3.3 Sample analysis	45
Chapter 4 Results	
4.1 Morphological changes of lased human enamel	49
4.2 Structural changes in synthetic hydroxyapatite	51
4.3 Structural changes in human enamel	58
4.4 Structural changes in bovine enamel	65
4.5 Powder X-ray diffraction	67
Chapter 5 Discussion: structural transformations in laser-treated human dental enamel	
5.1 Effects of low-power laser irradiation (1 W)	69
5.2 Effects of high-power laser irradiation (3 W)	72
5.3 Comparison of laser and thermally treated enamel	74
Chapter 6 Conclusion and potential application	
6.1 Conclusion	78
6.2 Potential application	79
References	80
Acknowledgements	94
Curriculum Vitae	96

Abstract

Dental enamel is the hardest tissue in the human body. It is a composite material of ~85% mineral, 12% water, and 3% protein and lipid by volume. The mineral component is hydroxyapatite, with hexagonal symmetry and the general formula $\text{Ca}_{10}(\text{PO}_4)_6(\text{OH})_2$. The structure of hydroxyapatite can be considered as built up by corner-sharing PO_4 and CaO_6 polyhedra forming channels along the crystallographic *c*-axis, in which the hydroxy-groups are placed. The apatite structure is adaptive to various inclusions. Dental apatite contains a substantial amount of carbonate groups, which substitute for the OH^- groups (A-type CO_3^{2-}) or for phosphate tetrahedral (B-type CO_3^{2-}).

Lasers have been used for different types of dental treatment. These include caries removal and prevention, etching of the tooth surface, preparation of teeth for restorative purposes, soft tissue surgery, and recently for light activation of tooth bleaching materials. Laser treatment has the advantage of being painless, time saving, precise and easy to control. It has been postulated that laser treatment might be able to enhance enamel resistance to acids. Among different laser sources promoted to be used in the dental clinical practice, CO_2 lasers have attracted considerable attention because of the high absorption coefficient of the dental hard tissues in the wavelength range of the CO_2 -laser emitted light. Although different morphological zones are caused by high-energy laser irradiation, there is limited information available on the atomic-scale structural changes within those zones.

Structural studies concerning laser-treated dental enamel had been reported mostly based on data collected from powdered samples and they had integrated over the total irradiated area. The ability of Raman and IR spectroscopy for micro-structural analysis is beneficial for studying the irradiation-induced local transformations in enamel apatite in areas which distinct distance from the centre of the laser spot. Thus, complementary utilization of Raman and ATR IR micro-spectroscopy is essential to better understand the gradient of irradiation-induced changes within the morphologically altered areas.

In this work, human enamel and synthetic hydroxyapatite samples were irradiated with an Opus Duo (OpusDent) dental CO_2 -laser operating at 10.6 μm in either super pulse (SP) or continuous wave (CW) mode. The diameter of the focused beam was ~600 μm . Different combinations of laser irradiation parameters, power, irradiation time and laser operation mode,

were applied. The morphology of the irradiated areas was investigated by reflectance optical microscopy using a Leica DMRXP microscope. The gradient of the structural alteration and molecular exchange across CO₂ laser-irradiated areas was analyzed by using Raman and attenuated total reflectance (ATR) infrared micro-spectroscopy.

The type and the degree of structural changes in morphologically distinguishable zones within the laser spot vary depending on the laser-irradiation parameters power (1 and 3 W), treatment time (5 and 10 s) and operational mode (super pulse or continuous wave). Using higher power, irrespective of the operational mode, the enamel tissue ablates and a crater is formed. The prevalent phase at the bottom of the crater is dehydrated O₂²⁻-bearing apatite, however, the fundamental framework topology is preserved. Additional nonapatite calcium phosphate phases are located mainly at the slope of the laser crater. No structural transformation of the mineral component was detected aside the crater rim, only a CO₃-CO₂ exchange, which decays on increasing radial distance from the crater. A lower-power laser irradiation slightly roughens the enamel surface and the structural modification of enamel apatite is considerably weaker for the continuous wave than for the super pulse mode. Prolonged low-power laser treatment results in recrystallization. Thus structural recovery of apatite might be of clinical relevance for enamel surface treatments. Laser treatment is compared with heat treatment and the effects of laser irradiation parameters as well as potential applications are discussed in this dissertation.

Chapter 1

Dental enamel and calcium phosphate

1.1 Tooth and enamel

Teeth are the body's hardest, most durable organ structure. Humans use teeth to tear, grind, and chew food in the first step of digestion. Teeth also play a role in human speech—the teeth, lips, and tongue are used to form words by controlling airflow through the mouth. Additionally, teeth provide structural support to muscles in the face and form the human smile.

1.1.1 Histological structural components of teeth

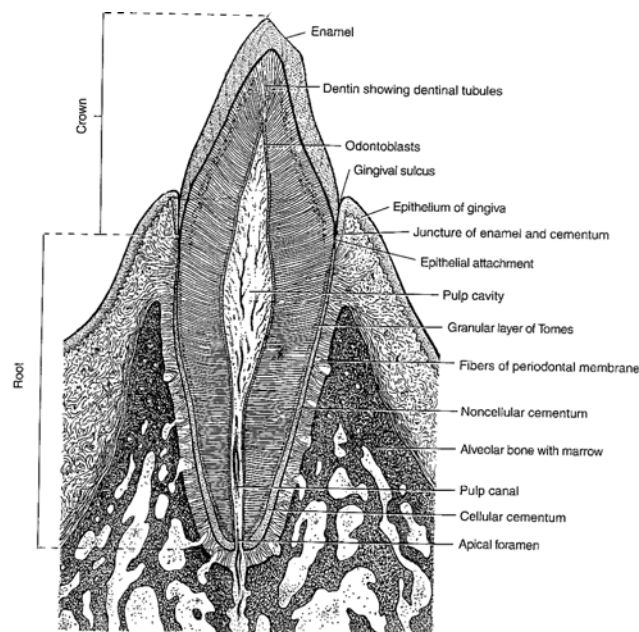


Fig. 1. Sagittal section through an incisor tooth and its mucosal supporting structure [Ross et al., 2002].

The visible portion of the tooth is called the crown. Projections on the top of each crown, used

primarily for chewing and grinding, are called cusps. The portion of the tooth that lies beneath the gum line is the root. The periodontal ligament anchors the tooth in place with fibers that connect the cementum in the root to a special socket in the jawbone called the alveolus.

Human teeth consist of four distinct types of tissue: enamel, dentin, pulp, and cementum. Enamel, the clear outer layer of the tooth above the gum line, is the hardest substance in the human body. In human teeth, the enamel layer can be as thick as 2.5 mm and protects the inner layers of the teeth from harmful bacteria and changes in temperature from hot or cold food. Directly beneath the enamel is dentin, a hard, mineral material that is similar to human bone, only stronger. Dentin surrounds and protects the pulp, the core of the tooth. The pulp contains blood vessels, which carry oxygen and nutrients to the tooth, and nerves, which transmit pain and temperature sensations to the brain. The outer layer of the tooth that lies below the gum line is cementum, a bone like substance that anchors the tooth to the jawbone [Wu, 1979; Jones, 2001].

1.1.2 Chemical structure of teeth

Teeth are highly mineralized tissues in human body. Mature tooth enamel consists of 96% inorganic material, less than 1% organic material and about 3% water by weight (85%, 3% and 12% by volume). Inorganic material is mainly biological apatite, which is carbonated hydroxyapatite (CAP) with a variety of ion-substitutions. Organic materials are protein (amelogenin and enamelin) and lipid [Fried et al., 2002; Glimcher et al., 1961]. Dental enamel appears to consist of a mass of rod-like crystallite, oriented essentially with their long axes parallel to the direction of the enamel prisms (outward to the enamel surface from the dentin-enamel junction, DEJ) and separated by exceedingly narrow spaces. The average crystallite size was measured at 160 nm in length and 20 nm in width for human enamel by transmission electron microscopy. This is more than 200 times that of dentine and bone crystallite [Wu, 1979]. Approximately 25% of the water in enamel and almost all the protein and lipid are located in the interprismatic space located between the prisms. Additionally, water in enamel is incorporated as a hydration shell surrounding individual CAP crystals [Sakae et al., 1997].

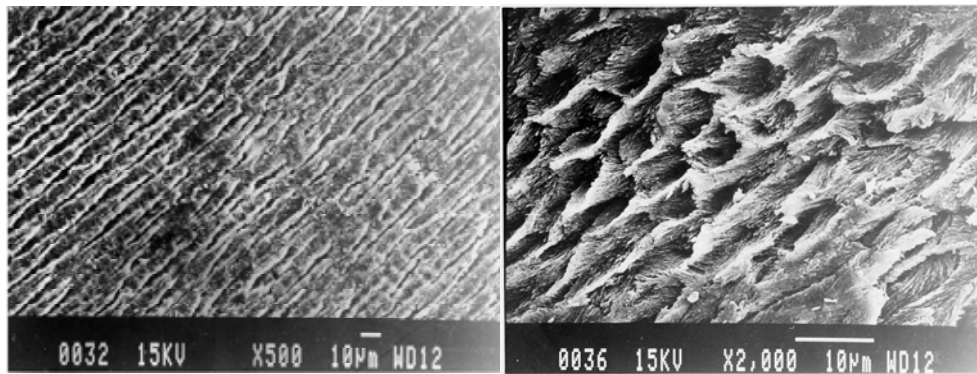


Fig. 2. SEM images of enamel surface. Left: longitudinally sectioned enamel rods; Right: cross sectioned enamel rods. Crystallite and interrods can easily be seen [Shi, 2004].

Dentin contains less inorganic material but more organic material and water. CAP in dentin is 70% by weight. Organic material and water constitute 30%. The principle organic in dentin is type I collagen which is not found in enamel [Wentrup-Byrne et al., 1997]. Across the DEJ, the mineral content decreases from enamel to dentin while the organic component increases [Schulze et al., 2004].

The physical properties of enamel are unique due to its structural components. The hardness of enamel is 5-8 MH (Motus hardness). It cracks easily and is very brittle. The carbonate content results in low thermal stability, e.g. decomposition at high temperature. Carbonate substituted hydroxyapatite is more soluble than pure hydroxyapatite in acid solution.

1.1.3 Enamel formation

Enamel formation is also called amelogenesis and occurs in the crown stage of tooth development. Enamel formation is followed by the formation of dentin. Enamel formation occurs in two stages: the secretory and maturation stages. Proteins and an organic matrix form partially mineralized enamel in the secretory stage; the maturation stage completes enamel mineralization.

In the secretory stage, ameloblasts release enamel proteins that contribute to the enamel

matrix, which is then partially mineralized by the enzyme alkaline phosphates. The appearance of this mineralized tissue, which occurs usually around the third or fourth month of pregnancy, marks the first appearance of enamel in the body. Ameloblasts deposit enamel at the location of what become cusps of teeth alongside dentin. Enamel formation then continues outward, away from the center of the tooth. In the maturation stage, the ameloblasts transport some of the substances used in enamel formation out of the enamel. Thus, the function of ameloblasts changes from enamel production, as occurs in the secretory stage, to transportation of substances. Most of the materials transported by ameloblasts in this stage are proteins used to complete mineralization. By the end of this stage, the enamel has completed its mineralization [Ross et al., 2002; Mann, 1997].

1.2 Enamel apatite

1.2.1 Structure of hydroxyapatite

Since enamel apatite is mainly hydroxyapatite, partially substituted by other ions, it is important to understand the structure of hydroxyapatite [Wen, 1989]. The known pure calcium phosphates have been classified into three major structural types:

- a) The apatite type, $\text{Ca}_{10}(\text{PO}_4)_6\text{X}_2$, which includes the derivatives of hydroxyapatite ($\text{X} = \text{OH}$)(HAP) and fluorapatite ($\text{X} = \text{F}$) (FAP) as well as those related to apatite-type structures such as octacalcium phosphate (OCP), Octacalcium bis(hydrogenphosphate) tetrakis(phosphate) pentahydrate, $\text{Ca}_8(\text{HPO}_4)_2(\text{PO}_4)_4 \cdot 5\text{H}_2\text{O}$ and tetracalcium phosphate (TTCP), $\text{Ca}_4(\text{PO}_4)_2\text{O}$.
- b) The glaserite type, which can be considered to include all polymorphs of tricalcium phosphates (TCP), $\text{Ca}_3(\text{PO}_4)_2$.
- c) The Ca- PO_4 sheet-containing compounds, which include dicalcium phosphate dihydrate (DCPD), $\text{CaHPO}_4 \cdot 2\text{H}_2\text{O}$, dicalcium phosphate anhydrous (DCPA), CaHPO_4 , and monocalcium phosphates, $\text{Ca}(\text{H}_2\text{PO}_4)_2 \cdot \text{H}_2\text{O}$ and $\text{Ca}(\text{H}_2\text{PO}_4)_2$ [Calderin and Scott, 2003].

Apatites are a structural type for compounds of the general formula $\text{M}_{10}(\text{XO}_4)_6\text{Y}_2$ rather than

specific compounds. In general, they are known to be capable of accommodating a wide variety of modifications and combinations of substitutions of ions and groups within the apatitic lattice. However, the term “apatite” has been extensively and synonymously used to represent the calcium phosphates, $\text{Ca}_{10}(\text{PO}_4)_6\text{X}_2$, where $\text{X} = \text{F}^-$, OH^- , or Cl^- and this concept will be followed in this review. Apatites are thermodynamically the most stable phases among the calcium phosphates and, therefore, can be considered as the probable end product in many reactions.

Hydroxyapatite (HAP), $\text{Ca}_{10}(\text{PO}_4)_6(\text{OH})_2$, is used as a model for inorganic components of bones and teeth. However, apatites as they occur in biological tissues, mineral formations and laboratory products can incorporate a wide variety of impurities and are seldom found in pure stoichiometric form. The most common form is hexagonal and the crystal structure has been described in the space group $\text{P6}_3/\text{m}$ (No. 176) with lattice parameters $a = b = 9.432 \text{ \AA}$ and $c = 6.881 \text{ \AA}$, $Z = 1$. The structure is depicted in Fig. 3 and Fig. 4. The 10 Ca^{2+} ions occupy two crystallographically different symmetry sites, 4f and 6h. Four Ca^{2+} ions (4f) are located in columns along the three-fold axes at $1/3, 2/3, 0$ and $2/3, 1/3, 0$ separated by approximately one half of the c-axis. These are commonly referred to as Ca1 (or column Ca). Ca1 is coordinated to nine O atoms, with six shorter bonds that define an approximate trigonal prism and three longer bonds capping the prism faces. The Ca-O_9 polyhedra share the trigonal faces to form chains parallel to the c-axis. The remaining six Ca^{2+} ions (6h sites, referred to as Ca2 or triangular Ca) form two triangular sets at $z = 1/4$ and $3/4$ on the mirror planes. The Ca2 ions are seven-coordinated, with six O atoms and one OH^- ion. The six PO_4^{3-} ions occupy 6h positions similar to the Ca2 ions, in expanded triangular positions. Adjacent Ca1 and Ca2 polyhedra are linked through oxygen atoms of the PO_4^{3-} tetrahedra. Because of the crystallographic mirror symmetry imposed by the space group, each OH^- ion has to be considered at statistically disordered positions (4e) both above and below the mirror planes at $z = 1/4$ and $3/4$. It has been shown by neutron diffraction studies that the oxygen atoms in hydroxide ions are 0.34 \AA away from the mirror plane with the OH^- direction pointing away from the mirror planes. An averaged structure could imply that in approximately half the unit cells the OH^- ions are pointed upward from the mirror plane and in the remaining unit cells

they are pointed downward. However, this statistical disordering does not have to be completely random. At least some short range ordering is to be invoked such as OH-OH-OH...HO-HO. The reversal of the OH⁻ direction can be achieved by replacement of an OH⁻ by F⁻ or Cl⁻ etc. or by a vacancy. Thus, the hexagonal HAP is probably never strictly stoichiometric [Calderin, 2003; Tsuda and Arends, 1994].

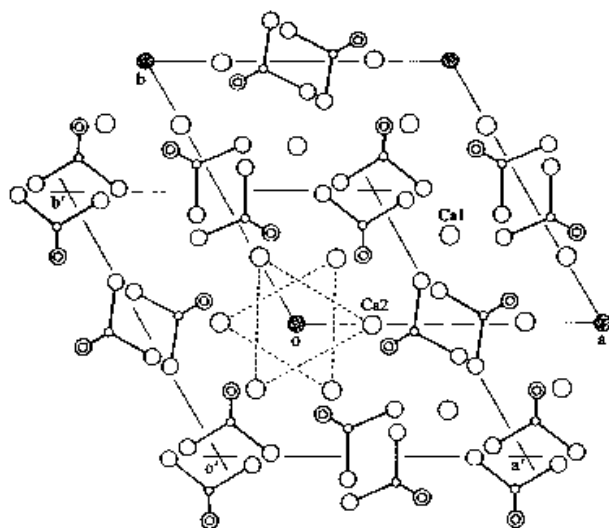


Fig. 3. Crystal structure of FAP or hexagonal HAP projected down the c -axis. The corners of the unit cell (marked by shaded circles) are occupied by F⁻ in FAP and by OH⁻ in HAP. An alternate choice of unit cell is identified as a' and b' .

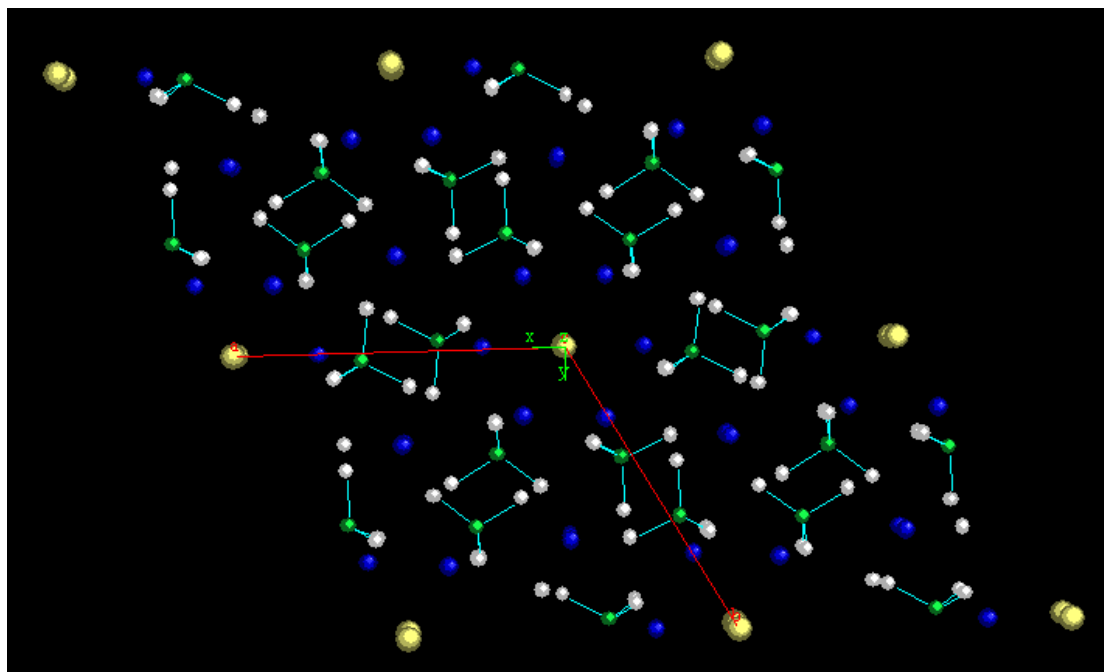


Fig. 4. Crystal structure of hydroxyapatite. Yellow ball: OH group; White ball: O atom; Green ball: P atom; Blue ball: Ca atom.

Stoichiometric HAP has been described as monoclinic, space group $P2_1/b$ having cell parameters $a = 9.4214(8) \text{ \AA}$, $b = 2a$, $c = 6.8814(7) \text{ \AA}$, $\gamma = 120^\circ$, with twice as many formula units per unit cell as in the hexagonal unit. The structure is closely related to that of the hexagonal form, but with no restrictions imposed by the mirror symmetry. The Ca^{2+} and PO_4^{3-} ions occupy similar positions as in the hexagonal form. However, the OH^- ions are located in two different columns. Within each column all the OH^- ions have the same direction of displacements from $z = 1/4$ as in the hexagonal form. All the OH^- ions in one column point upward, while those in the other column point downward. Thus, there is no disordering of the OH^- ions in the monoclinic form. The monoclinic form is formed only under favorable thermal conditions [Mathew and Takagi, 2001; Gomez-Morales et al., 2001].

1.2.2 Substitution of hydroxyapatite

HAP can incorporate a wide variety of substitutions for Ca^{2+} , PO_4^{3-} , and/or OH^- ions. Substitution of other elements for Ca^{2+} and PO_4^{3-} is relatively minor in most natural mineral samples. Natural minerals of the composition, $\text{Ca}_{10}(\text{PO}_4)_6(\text{F},\text{OH},\text{Cl})_2$ exhibit large variations in F^- , OH^- , and Cl^- contents. Pure end-members are uncommon in nature, but binary and ternary compositions are widely reported [Elliott et al., 1973].

The X^- ion positions in apatites or the “X ion channels”, as they are often referred to, appear to be the sites of a great deal of interesting activity in apatites. The X^- ion positions in apatites are substituted by a variety of ions, frequently by OH^- , F^- , and Cl^- , but also by CO_3^{2-} and O^{2-} , or by vacancies or any combination of these. In pure form each X^- ion takes up its own particular location, as noted above. However, when two or more of these ions are present at the same time, they interact with each other to produce effects not predicted from the knowledge of the structures of the end-member alone. The positional z -parameters of the X^- ions are shifted from their normal positions in the pure form, but the effects are more pronounced when the larger Cl^- ions are involved. A monoclinic form of a natural ternary apatite, $\text{Ca}_5(\text{PO}_4)_3(\text{F}_{0.29}, \text{Cl}_{0.47}, \text{OH}_{0.24})$, space group $P2_1/b$, has been reported. There are two anion columns in the unit cell and both columns contain all three anions. The reduction in

symmetry from hexagonal to monoclinic results from ordering of the column anions in each column in one of the two symmetry equivalent anion sites present in the hexagonal ternary apatite. Table 1 shows the difference of apatite group unit cells after X ion substitution.

Table 1. Apatite Group Unit Cells.

End-Member	Hydroxyapatite	Fluorapatite	Chlorapatite
Formula	$\text{Ca}_5(\text{PO}_4)_3\text{OH}$	$\text{Ca}_5(\text{PO}_4)_3\text{F}$	$\text{Ca}_5(\text{PO}_4)_3\text{Cl}$
Form. Wt.	502.322	504.313	520.767
Density	3.153	3.201	3.185
Mol Volume	159.334	157.527	163.527
z	2	2	2
Cryst. Sys.	Hexagonal	Hexagonal	Hexagonal
Cryst. Class	6/m	6/m	6/m
Space Group	$\text{P6}_3/\text{m}$	$\text{P6}_3/\text{m}$	$\text{P6}_3/\text{m}$
Cell Parameters			
a	9.424	9.367	9.628
c	6.879	6.884	6.764
Vol.	529.09	523.09	543.01
Ref.	Sudarsanan and Young, 1969	Sudarsanan et.al., 1972	Mackie et. al., 1972

The incorporation of foreign cations in the apatite lattice is expected to change the bulk properties of the apatite. The structure of a number of synthetic substituted apatites was investigated to evaluate the structural changes associated with the substitution. Lead is known as a “bone seeker” in that it accumulates in bone and tooth mineral. In a lead apatite study, a short Pb-O distance observed indicating a covalent bond may account for this lead incorporation. The structure of calcium-lanthanum apatite shows that cation ordering in apatites is strongly dependent on the properties of the constituent ions. However, in a series of Ba-rare earth-Na apatites the results indicate the substitutions to be unexpectedly complex to

derive any general prediction [Mathew and Takagi, 2001].

1.2.3 Structure of enamel apatite

Enamel apatite is crystal chemically and mineralogically more complicated than the ideal formula suggested for hydroxylapatite ($\text{Ca}_{10}(\text{PO}_4)_6\text{OH}_2$). The formula of enamel apatite, $(\text{Ca},\text{Na},\text{Mg},\text{Sr},\text{Pb},\dots)_{10}(\text{PO}_4,\text{CO}_3,\text{SO}_4\dots)_6 (\text{OH},\text{F},\text{Cl},\text{CO}_3)_2$, expresses the range found in members of the calcium phosphate apatite mineral group, and the mineral matter from vertebrate tissues. Tables 2 and 3 show the inorganic content of dental enamel and the real expressed enamel apatite formula [Anderson et al., 1996; Markovic et al., 2004; Skinner, 2005].

Table 2. Inorganic composition of dental enamel.

Reference	Component in dry weight (wt %)									Ca/P
	Ca	P	CO ₂	Na	K	Mg	Sr	Cl	F	
Patel and Brown, 1975	37.6	18.3	3.0	0.7	0.05	0.2	0.03	0.4	0.01	1.59
Weatherell et al., 1973	36.4	17.4	2.7	0.66	0.03	0.4		0.23	0.01	1.62

Table 3. Unit cell formula of enamel apatites from chemical analyses, OH from charge balance.

Formula	Reference
$\text{Ca}_{9.48}\text{Mg}_{0.18}\text{Na}_{0.11}(\text{PO}_4)_{5.67}(\text{CO}_3)_{0.45}(\text{OH})_{1.54}$	Hendricks and Hill, 1942
$\text{Ca}_{9.26}(\text{HPO}_4)_{0.22}(\text{CO}_3)_{0.5}(\text{PO}_4)_{5.63}(\text{OH})_{1.26}$	Aoba & Meoreno, 1992
$\text{Ca}_{9.23}\text{Na}_{0.26}\text{K}_{0.03}(\text{PO}_4)_{5.53}(\text{CO}_3)_{0.47}(\text{OH})_{1.15}\text{Cl}_{0.06}\text{F}_{0.01}$	Driessens, 1978
$\text{Ca}_{8.856}\text{Mg}_{0.088}\text{Na}_{0.292}\text{K}_{0.010}(\text{PO}_4)_{5.312}$ $(\text{HPO}_4)_{0.280}(\text{CO}_3)_{0.407}(\text{OH})_{0.702}\text{Cl}_{0.0708}(\text{CO}_3)_{0.050}$	Elliott, 1997

Except the trapped organic components, the major difference of enamel apatite from hydroxyapatite is in the presence of about 3 wt% CO₃. So the dental enamel apatite is carbonated hydroxyapatite [Sydney et al., 1991]. Details of the crystallographic structures of carbonate-containing apatites (including minerals) are important because CO₃²⁻ ions increase their reactivity, both in thermal and aqueous systems [Shellis and Wilson, 2004; Tang et al., 2003]. The OH⁻ ion content in Table 3 is deduced from the requirement for balance assuming that CO₃²⁻ ions only replace PO₄³⁻ ions (except the last formula in which a small fraction also replaces OH⁻ ions). Compared to hydroxyapatite, these formulae show a deficiency of ions in Ca²⁺ and OH⁻ ion sites. The loss of negative charge from the loss of OH⁻ ions and replacement of PO₄³⁻ by CO₃²⁻ ions is balanced by loss of positive charge from Ca²⁺ sites [Elliott, 1997; Featherstone et al., 1984; McClellan, 1980].

Polarized infrared (IR) spectroscopy of sections of enamel shows that the OH⁻ ions lie parallel to the c-axis, with evidence for perturbation of some OH⁻ by neighboring Cl⁻ ions. Such studies also show that the CO₃²⁻ ions are oriented with respect to the apatite lattice and are probably in two different environments. The majority of the CO₃²⁻ ions has their planes oblique to the c-axis and are thought to occupy the sloping faces of tetrahedral sites. This is the B-type substitute, e.g. CO₃²⁻ ions substitute for PO₄³⁻ ions. The minority of ions, comprising about 10% of the total, has their planes nearly parallel to the c-axis and are thought to occupy sites in the hexed axis channel. This is A-type substitute, e.g. CO₃²⁻ ions substitute for OH⁻ ions. The ratio of A-type versus B-type CO₃²⁻ substitution is around 10/90 [Elliott, 1985; El Feki et al., 1991; Sfihi and Rey, 2002; Wilson et al., 1999].

1.2.4 Other related calcium phosphate minerals

Chlorapatite

Chlorapatite (ClAP), Ca₁₀(PO₄)₆(Cl)₂, has been described in the hexagonal space group P6₃/m, with cell parameters, a = b = 9.598(2) Å, c = 6.776(4) Å, Z = 1. Like OH⁻ in HAP, the Cl⁻ is also disordered, displaced from the midpoint of the Ca₂ triangles, and in positions 1.2 Å above and below the mirror planes. The Cl⁻ is so far removed from the mirror plane towards

the midway point between the two Ca₂ triangles, that an additional weak bond develops between the Ca₂ and a second Cl⁻ ion. Stoichiometric ClAP has also been found to crystallize in the monoclinic space group with space group P21/b having cell parameters $a = 9.628(5) \text{ \AA}$, $b = 2a$, $c = 6.764(5) \text{ \AA}$, $\gamma = 120^\circ$, $Z = 2$. The structure is very similar to the hexagonal one, but the Cl⁻ ions are ordered in two columns on pseudo-hexagonal axes as in the case of the monoclinic HAP [Devarajan and Klee, 1981].

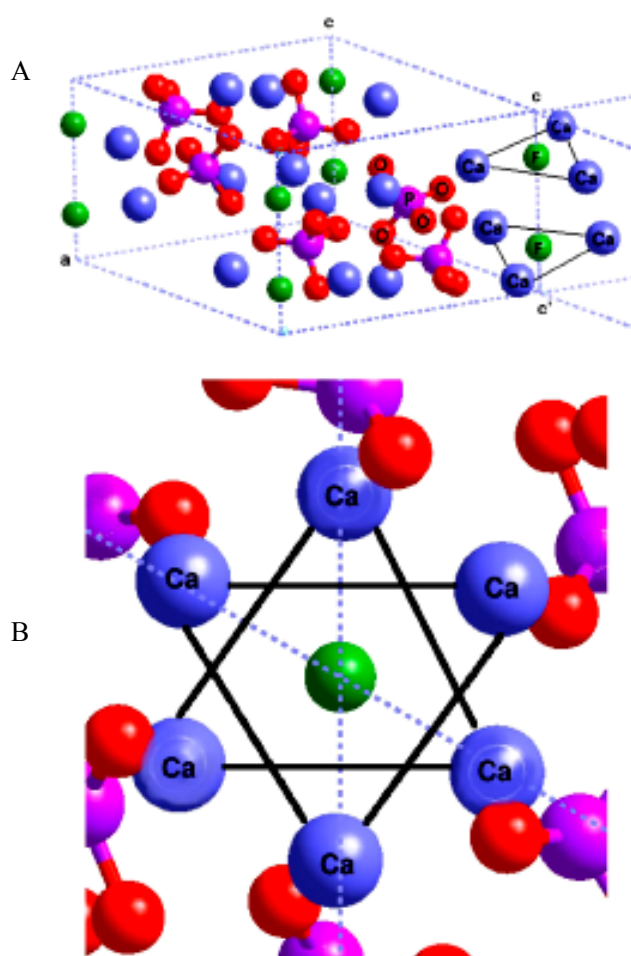


Fig. 5. A: General view of the fluorapatite structure including calcium triangles. B: Top view of four unit cells along c-c' showing the calcium triangles. The phosphorus triangles can also be seen [Calderin and Scott, 2003].

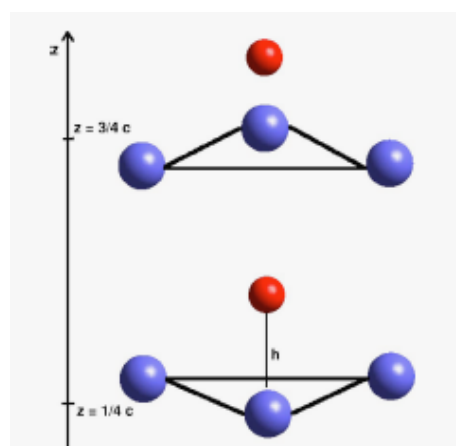


Fig. 6. Close up of the region around the c axis. The two calcium triangles rotated by 60° and the anion are shown. For FAP the F ion is at $z=1/4$ in the plane of the calcium triangles, for ClAP the Cl ion is close to the $z=0.5 c$ position, for HAP the OH is just off the calcium triangles while for oxyapatite (OAP, $\text{Ca}_5(\text{PO}_4)_3\text{O}_{0.5}$) the O ion is at $z=0$ [Calderin and Scott, 2003].

Fluorapatite

Fluorapatite (FAP) is important in dental treatment. Fluorapatite is much less soluble than HAP. Fluorapatite, $\text{Ca}_{10}(\text{PO}_4)_6\text{F}_2$, is the most stable among the apatites. FAP is hexagonal with the space group $P6_3/m$ and lattice parameters, $a = b = 9.367(1) \text{ \AA}$ and $c = 6.884(1) \text{ \AA}$, $Z = 1$. The positions of the two sets of Ca^{2+} ions and the PO_4^{3-} ions are nearly identical to those of HAP. However, the F^- ions occupy the center of the Ca2 triangles (6h positions), on the mirror planes at $z = 1/4$ and $3/4$. Fig. 5, Fig. 6 and Table 4 show FAP structure different from HAP and ClAP [Devarajan and Klee, 1981].

Table 4. Height h of the anions with respect to the calcium triangle and length of the side of the smaller triangle perpendicular to the c axis formed by calcium and phosphorus atoms.

Apatite	h (\AA)		Calcium triangle (\AA)		Phosphorus triangle (\AA)	
	Calc	Expt	Calc	Expt	Calc	Expt
Fluorapatite	0.01	0	3.85	3.99	5.97	6.25
Chlorapatite	1.33	1.22	4.06	4.17	6.16	6.54
Hydroxyapatite	0.27	0.3	4	4.08	6.02	6.27
Oxyapatite	1.46		3.67		6	
c empty			3.82		6.02	

[Calderin and Scott, 2003]

Octacalcium phosphate

Octacalcium phosphate (OCP, $\text{Ca}_8(\text{HPO}_4)_2(\text{PO}_4)_4 \cdot 5\text{H}_2\text{O}$) is often found as an intermediate phase during the precipitation of the thermodynamically more stable calcium phosphates (e. g. HAP) from aqueous solutions. OCP is triclinic, space group $P\bar{1}$ with 2 asymmetric units per unit cell. It consists of apatitic layers separated by hydrated layers. The presence of the apatite layer explains the similarities of the lattice parameters with those of HA. An apatite layer consists of alternating sheets of phosphate ions interspersed with Ca^{2+} ions; and the hydrated layers consist of more widely spaced phosphate and Ca^{2+} ions with a slightly variable number

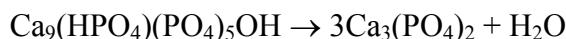
of water molecules between them. OCP is of great biological importance because it is one of the stable components of human dental and urinary calculi. It plays an important role in the in vivo formation of apatite biominerals. A central OCP inclusion, also known as central dark line is seen by transmission electron microscopy in many biological apatites and in some synthetically precipitated hydroxyapatites [Shi, 2004; Mathew and Takagi, 2001].

Tetracalcium phosphate

Tetracalcium phosphate (TTCP), $\text{Ca}_4(\text{PO}_4)_2\text{O}$, is monoclinic, space group $P2_1$, with unit cell parameters $a = 7.023(1) \text{ \AA}$, $b = 11.986(4) \text{ \AA}$, $c = 9.473(2) \text{ \AA}$ and $\beta = 90.90(1)^\circ$. The Ca^{2+} and PO_4^{3-} ions in TTCP are located in four sheets perpendicular to the b-axis. Each sheet contains two Ca- PO_4 columns and one Ca-Ca column. The solubility of TTCP in water is higher than HAP. This property results in the difficulty of separating it from aqueous solution. The solid state reaction at high temperature can be used to prepare TTCP intended for bone repair [Shi, 2004; Mathew and Takagi, 2001].

Tricalcium phosphate (TCP)

β -TCP ($\beta\text{-Ca}_3(\text{PO}_4)_2$) is the true calcium orthophosphate of the stoichiometric composition $\text{Ca}_3(\text{PO}_4)_2$. β -TCP has the rhombohedral space group $R3_cH$ with 21 formula units per hexagonal unit cell. It can not be precipitated from solution, but may only be prepared by calcinations of calcium deficient hydroxyapatite (CDHA) at temperatures above 800°C :



Near 1125°C , it transforms into the high-temperature phase α -TCP. Being the stable phase at room temperature, β -TCP is less soluble in water than α -TCP. Pure β -TCP never occurs in biological calcification. Only the magnesium-containing form called whitlockite ($\beta\text{-(Ca, Mg)}_3(\text{PO}_4)_2$) is found in dental calculi and urinary stones, dental caries, salivary stones, arthritic cartilage, as well as in some soft-tissue deposits [Le Geros, 1994; Dias et al., 2005]. α -TCP ($\alpha\text{-Ca}_3(\text{PO}_4)_2$) is a metastable phase at room temperature, prepared from β -TCP at above 1125°C . α -TCP has a monoclinic space group $P2_1/a$, with 24 formula units per unit cell. α -TCP is more reactive in aqueous systems than β -TCP and can be hydrolyzed to a mixture of other calcium phosphates [Donadel et al., 2002; Gibson et al., 2000].

α -TCP and β -TCP play important roles in present day bone grafting procedures. β -TCP is more stable than the α phase. β -TCP with uniformly distributed Ca vacancies is the most stable structure [Yin et al., 2003].

Amorphous calcium phosphate (ACP)

Amorphous means non-crystalline. Amorphous materials lack the long-range, periodic order of crystalline materials. The ordered atomic arrangements which can exist in ACP are highly localized, occurring within domains that do not exceed 0.9 nm in diameter. Regularity in the local environment of individual Ca^{2+} ions in ACP appears to be limited within a distance of 0.3 nm. The morphology seen in electron microscopy consists of roughly spherical $\text{Ca}_9(\text{PO}_4)_6$ clusters aggregated randomly with their inter-cluster spaces filled with water [Mathew and Takagi, 2001].

ACP is usually considered as a postulated precursor in the formation of biological hydroxyapatite. ACP has a higher solubility in aqueous environment than HAP. It releases calcium and phosphate ions in aqueous environments, which may lead to deposition of apatite mineral in tooth structure. Thus it may play an important role in the remineralization of enamel, a calcium and phosphate ion reservoir. During the assembly of hydroxyapatite, ACP links HAP nanocrystals in uniform orientation and finally into a large HAP crystal particle [Schumacher et al., 2007; Skrtic et al., 2003; Tao et al., 2007].

ACP is highly bioactive and biodegradable, so it can be used as an implant coating, sealant, filler and bone cement. The most common preparation method is synthesis of calcium phosphate in aqueous solution. Sometimes stabilizers are needed. ACP is not stable in aqueous solution. It will dissolve, forms the nucleus of HAP crystal following by the growth of HAP crystal. Many parameters can affect this transformation, such as CAP size, temperature, pH value, additive type and concentration. ACP can also be prepared by quenching of molten calcium phosphates [Li et al., 2006].

Chapter 2

Dental laser: background and applications

2.1 Laser application in dental practice

The pioneering work on the effect of laser on dental hard tissue was published by Stern and Sognnaes in 1964. By now, various laser types have been applied for dental treatment of both soft and hard tissue.

2.1.1 Diagnostic laser applications

Low power laser energy has been utilized for different dental applications, both in a clinical setting (Table 5) and in dental research (Table 6). Low power lasers typically operate at powers of 100 milliwatts or less, and may produce energy in the visible, (400-700nm wavelength), ultraviolet (200-400nm), or near infrared regions (700-1500nm). There are few purpose built low power lasers for the middle infrared (1500-4000nm) or far infrared regions (4000-15000nm). Lasers operating in the middle and far-infrared regions are used in health care primarily for hard and soft tissue procedures [Featherstone, 2000, 2003; Walsh, 2003].

Table 5. Diagnostic laser applications for clinical practice [Walsh, 2003].

	Argon 488nm	Helium-neon 633nm	Diode 633nm	Diode 655nm	CO ₂ 10600nm
Laser fluorescence detection of dental caries	×			×	
Laser fluorescence detection of subgingival calculus				×	
Detection of fissure caries lesions by optical changes					×
Laser doppler flowmetry to assess pulpal blood flow		×	×	×	
Scanning of phosphor plate digital radiographs					
Scanning of conventional radiographs for teleradiology		×			

Laser fluorescence systems for detection of dental caries have been described in the first stage of developing this technique for caries detection, an argon laser with visible blue light was used to show the presence of the lesion. At the beginning of this development stage, since there is no fluorescence coming out from carious enamel and dentine, the utilization of visible light is a must. Subsequent development focused on the fluorescence from bacterial deposit. A visible red laser light from a semiconductor diode was used to produce fluorescence from bacterial deposits [Walsh, 2003]. Fluorescence for early caries detection has been done by a red laser device, ‘Diagnodent’ (KaVo Dental Corporation, Illinois, the U. S.). The red laser can easily penetrate into the tooth. When an undersurface lesion is reached, fluorescence is created. The fluorescent light is read by a detector, which gives out a digital display and sound. The advantage of this instrument is that it can detect the hidden lesion better than the visible light [Featherstone, 2000, 2003]. The light is narrow focused so that the interference of position and angulation artifacts can be avoided. This method does not require tooth preparation and can give out in situ date [Barbour and Rees, 2004].

Table 6. Diagnostic laser applications used as research tools [Walsh, 2003].

	Nd:YAG 1064nm	Er:YAG 2940nm	Argon 488; 515nm	Helium-neon 633nm	Diode 633; 670nm
Raman spectroscopic analysis of tooth structure	×				
Terahertz imaging of internal tooth structure	×				
Breakdown spectroscopic analysis of tooth structure	×	×			
Confocal microscopic imaging of soft and hard tissues				×	
Flow cytometric analysis of cells and cell sorting				×	
Profiling of tooth surfaces and dental restorations				×	×

2.1.2 Photochemical laser effects

The Argon laser produces high intensity visible blue light (488nm) which is able to initiate photopolymerization of light-cured dental restorative materials. Compared with conventional quartz tungsten halogen lamp units, the pulp temperature increase is much less with argon

laser curing. The curing time can be reduced and the depth of cure can be improved with Argon laser. This makes sense in dental practice [Lin et al. 2001; Walsh, 2003].

Dental lasers have been shown to facilitate tooth bleaching procedure. The principle of bleaching is based on the decomposition of color compounds in tooth. These chelate compounds are formed between apatite, porphyrins, and tetracycline compounds. When a narrow spectral range of green light (510-540nm) is irradiated on these compounds, light energy is absorbed and destroys the chelate bonds. The argon laser (515nm) and the potassium titanyl phosphate (KTP) laser (532nm) can both be used for photochemical bleaching, since their wavelengths approximate the absorption maxima of the chelate compounds (525-530nm). Diode (810-980 nm) and CO₂ (10600nm) lasers can also be used for bleaching, but are not as efficient as argon and KTP lasers [Walsh, 2003].

2.1.3 Laser applications in the dental laboratory

Along with the development of laser and computer techniques, laser applications in the dental laboratories are on the rise (Table 7). Laser 3-D imaging is a well established technique: laser holographic imaging can be used for storing topographic information, such as crown preparations, occlusal tables, and facial forms. The principle is based on interferometry of two laser beams so that it can map more complex surface into detail. Combining laser with computer technique can be applied for more precise measurement and complex processing. One example is the laser scanning of casts for the fabrication of restorations from porcelain and other materials. Lasers are further used to sinter ceramic materials in order to create a solid restoration from a powder of alumina or hydroxyapatite. The laser type used for sintering is the CO₂ laser (10600nm) [Walsh, 2003].

Table 7. Laser applications in the dental laboratory [Walsh, 2003]

	Helium neon	Diode	Nd:YAG	CO2	Helium-Cadmium
	633 nm	635 nm	1064 nm	10600 nm	300 nm
Scanning of models for orthodontics or holographic storage	×	×			
Scanning of crown preparations for CAD-CAM	×	×			
Welding of metals (Co:Cr, titanium)			×		
Sintering of ceramics				×	
CAD-sintering fabrication				×	
CAD-polymer fabrications of splints or surgical models					×
Cutting of ceramics			×		

2.1.4 Laser procedures on dental hard tissues

At the present time, several laser types with similar wavelengths in the middle infrared region of the electromagnetic spectrum are used commonly for cavity preparation and caries removal. The Er:YAG, Er:YSGG and Er,Cr:YSGG lasers operate at wavelengths of 2940, 2790, and 2780nm, respectively. These wavelengths correspond to the peak absorption range of water in the infrared spectrum (Fig. 7), although the absorption of the Er:YAG laser (absorption value 13000) is much higher than that of the Er:YSGG (absorption value 7000) and Er,Cr:YSGG (absorption value 4000). Since all three lasers rely on water-based absorption for cutting enamel and dentine, the efficiency of ablation (measured in terms of volume and mass loss of tooth structure for identical energy parameters) is greatest for the Er:YAG laser [Anderson et al., 2002; Apel et al., 2004; Keller and Hibst, 1997].

A probable ablation mechanism of these laser systems is the micro-explosion of under-enamel surface trapped water by laser irradiation. Normal dental enamel contains approximately 12% water by volume. Water cooling can be used to reduce the temperature of the enamel and the tooth [Courrol et al., 2004; Walsh, 2003; Tokonabe et al., 1999].

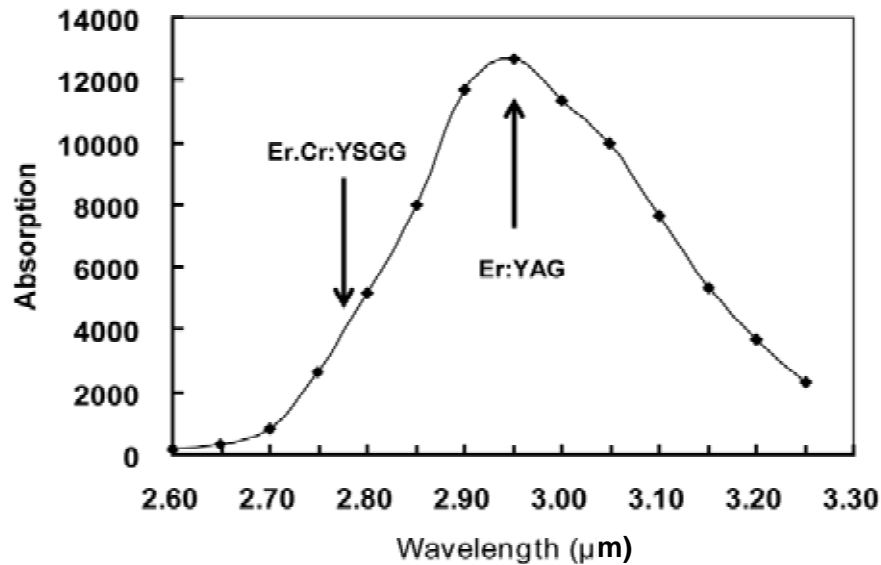


Fig. 7. The absorption curve of water in the middle infrared region. Data on the vertical axis are units of absorption, while the horizontal axis shows the wavelength in micrometers. The plot demonstrates the position of two laser wavelengths used for cavity preparation: Er,Cr:YSGG 2.78 micrometers, and Er:YAG 2.94 micrometers.

Other non-Erbium laser-based cavity preparation systems have been studied for several decades. These laser systems include Argon, super-pulsed CO₂, Ho:YAG, Ho:YSGG, Nd:YAG, Nd:NLF, diode lasers and excimers laser [Featherstone et al., 1998; Harayaki et al., 2001; Harris et al., 2002; Hicks et al., 1990; Hsu et al., 2000; Kantorowitz et al., 1998; Klein et al., 2005; Lakshmi et al., 2001; Nelson et al., 1986; Noel et al., 2003; Tsai et al., 2002; Zezell et al., 1995; Patel and Damle, 1996].

There is a range of other well established laser hard tissue procedures including desensitization of cervical dentine (using Nd:YAG, Er:YAG, Er,Cr:YSGG CO₂, KTP, and diode lasers), laser analgesia (using Nd:YAG, Er:YAG, and Er,Cr:YSGG lasers) and laser-enhanced fluoride uptake (using Er:YAG, Er,Cr:YSGG, CO₂, argon, and KTP lasers). Furthermore, there is a considerable range of periodontal procedures (Table 8), and endodontic procedures (Table 9) which can be undertaken with lasers as an alternative to conventional approaches [Akova et al., 2005; Alexander et al., 2002; Fox et al., 1992; Willms et al., 1996; Yu et al., 2001; Zezell et al., 1998].

Table 8. Periodontal laser procedures [Walsh, 2003].

	Er:YAG 2940 nm	Er,Cr: YSGG 2780 nm	KTP 532 nm	Argon 488 or 515 nm	Diode 810-980 nm	Nd:YAG 1064 nm	Diode 635, 670 or 830 nm	CO ₂ 10600 nm
Calculus removal	×							
Periodontal pocket disinfection	×	×	×	×	×	×		
Photoactivated dye disinfection of pockets							×	
De-epithelialization to assist regeneration	×	×						×

Table 9. Endodontic laser procedures [Walsh, 2003].

	Er:YAG 2940 nm	Er,Cr: YSGG 2780 nm	KTP 532 nm	Argon 488 or 515 nm	Diode 810-980 nm	Nd:YAG 1064 nm	Diode 635, 670 or 830 nm	CO ₂ 10600 nm
Direct pulp capping	×							×
Drying of the root canal	×	×						×
Removal of smear layer	×	×						
Root canal disinfection	×	×	×	×	×	×		
Photoactivated dye disinfection of pockets							×	

Table 10. Surgical laser applications [Walsh, 2003].

	Er:YAG 2940 nm (least haemostasis)	Er,Cr: YSGG 2780 nm	CO ₂ 10600 nm	KTP 532 nm	Diode 810-980 nm	Argon 488 or 515 nm	Nd:YAG 1064 nm (most haemostasis)
Minor soft tissue surgery	×	×	×	×		×	×
Major soft tissue surgery			×				
Surgical treatment of large vascular lesion						×	
Bone cutting	×	×					
Implant exposure with bone removal	×	×	×				

2.1.5 Soft tissue laser procedures

Soft tissue procedures performed with lasers include removing excess gum tissue and exposing teeth and dental implants. Four types of lasers have been used: CO₂, Nd:YAG, Argon and Holmium:YAG. The advantages of laser surgery are reduced bleeding and pain compared with conventional technique. Laser might be better suited in patients with bleeding disorders (Table 10) [Lewis, 1995; Walsh, 2003].

2.1.6 Other applications

Laser etching of enamel surfaces might be adequate for orthodontic bonding [Fuhrmann et al., 2001; Groth et al., 2001; Obata et al., 1999; Shahabi et al., 1997; Usumez et al., 2002]. CO₂ lasers have been used for bracket debonding in orthodontics [Fried et al., 2001; Subramanya et al., 1992; Malmstrom et al., 2001]. Laser irradiation of enamel surfaces might be able to improve the resistance of enamel to acid environment and prevent demineralization of dental enamel [Attrill et al., 2000; Azzeh and Feldon, 2003; Corpas-Pastor et al., 1997; Delbem et al., 2003; Flaitz et al., 1995; Fraunhofer et al., 1993; Hsu et al., 2001; Kwon et al., 2005; Meurman et al., 1997; Nammour et al., 2005; Santaella et al., 2004; Huang et al., 2001].

2.2 Type of lasers

2.2.1 Classification

Traditionally, lasers have been classified according to the physical construction of the laser (e.g., gas, liquid, solid state, or semiconductor diode), the type of medium which undergoes lasing (e.g., Erbium: Yttrium Aluminium Garnet (Er:YAG)) (Table 11), and the degree of hazard to the skin or eyes following inadvertent exposure (Table 12).

2.2.2 Laser type according to wavelength

There are four classes of laser wavelengths: 1) ultraviolet or excimer lasers, 2) visible light lasers, 3) infrared lasers, 4) tunable lasers.

a) Ultraviolet or excimer lasers: The wavelength range is approximately 150 nm to 350 nm. The term excimer is derived from the two terms "excited dimer" which is an elevated energy state known for rapid dissociation into small particles of energy. Excimer lasers exhibit high peak power levels, at approximately 10 - 15 Hz and produce remarkably clean cuts in tissue. However, they have a great potential for causing mutagenicity and cytotoxicity in various types of soft tissue [Arcoria, 2005].

Table 11. Common laser types used in dentistry [Walsh, 2003].

Laser type	Construction	Wavelength(s)	Delivery system(s)
Argon	Gas laser	488, 515nm	Optical fibre
KTP	Solid state	532nm	Optical fibre
Helium-neon	Gas laser	633nm	Optical fibre
Diode	Semiconductor	635, 670, 810, 830, 980nm	Optical fibre
Nd:YAG	Solid state	1064nm	Optical fibre
Er,Cr:YSGG	Solid state	2780nm	Optical fibre
Er:YAG	Solid state	2940nm	Optical fibre, waveguide, articulated arm
CO ₂	Gas laser	9600, 10300, 10600nm	Waveguide, articulated arm

Table 12. Laser classification according to potential hazards [Walsh, 2003].

Class	Risk	Examples
I	Fully enclosed system	Nd:YAG laser welding system used in a dental laboratory
II	Visible low power laser protected by the blink	Visible red aiming beam of a reflex surgical laser
IIIa	Visible laser above 1 milliwatt	No dental examples
IIIb	Higher power laser unit (up to 0.5 watts) which may or may not be visible Direct viewing hazardous to the eyes	Low power (50 milliwatt) diode laser used for biostimulation
IV	Damage to eyes and skin possible. Direct or indirect viewing hazardous to the eyes.	All lasers used for oral surgery, whitening, and cavity preparation

b) Visible light lasers: The visible light range is between 350 nm and 730 nm. The first laser made was a ruby laser, emitting at 693 nm. Argon ($\lambda = 488.5$ nm, blue; $\lambda = 514.5$ nm, green) laser is in the middle of the visible light portion of the electromagnetic spectrum. Argon lasers are heavily absorbed into red pigmentation (especially blood) and have a pronounced coagulative or hemostatic effect without affecting bone or tooth structure. Dye ($\lambda = 590$ nm) is most readily absorbed by blue pigmentation. He:Ne ($\lambda = 632$

nm) is one of the more common types of low-powered (0.5W) visible light lasers used in a variety of industrial and biomedical areas [Arcoria, 2005].

c) Infrared lasers: This class of lasers encompasses the most common types that are readily available in the marketplace. The wavelength range is between 730 nm and 12,000 nm. Nd:YAG (Neodymium:Yttrium-Aluminum-Garnet laser, $\lambda = 1064$ nm) lasers are the most popular type of dental lasers. The wavelength is most readily absorbed into black pigmentation and has a high degree of penetration into light-colored tissues using the continuous wave (CW) mode. Ho:YAG (Holmium:Yttrium-Aluminum-Garnet, $\lambda = 2100$ nm) lasers exhibit the greater potential to absorb into hydroxyapatite than the 1064 nm wavelength and can minimally "cut" tooth structure or recontour bone. The Er:YAG (Erbium:Yttrium-Aluminum-Garnet, $\lambda = 2900$ nm) laser is one of the newest and most promising types of "hard-tissue" lasers. This wavelength is the most readily absorbed into water and hydroxyapatite of all existing wavelengths and is considered a highly surface cutting laser. Energy levels needed to cut hard-tissue with an Er:YAG laser are approximately 150 to 200 mJ. Etching of tooth structure is seen at approximately 45 mJ of energy. CO₂ ($\lambda = 9300, 9600, 10300, 10,600$ nm) laser is the oldest of the dental lasers. This wavelength is readily absorbed into water and hydroxyapatite (although not to the degree of the Er:YAG laser) and is primarily a surface-cutting system. It possesses a coagulative-hemostatic effect, especially if bleeding involves vessels no larger than 0.5 mm in diameter, and can be used for treatment of hard and soft tissue. CO₂ laser with the wavelength of 10600 nm are more common even though 9300 and 9600 nm wavelength have higher absorption coefficient with dental enamel. Power levels needed to produce significant effects in hard and soft tissue are in the range of 2 to 4 Watts, CW [Arcoria, 2005; Featherstone and Fried, 2001].

d) Tunable lasers: Are known for not having a wavelength range because these lasers can access a wide-variety of wavelengths.

2.3 Effect of laser on dental enamel

2.3.1 Interaction of laser and dental hard tissues

When laser light interacts with tissue, it will be absorbed, penetrated or reflected. These interactions depend on the optical characteristics and laser wavelength (Table 13). Only absorbed laser can have effect on tissue. There are three types of absorption: absorption by mineral, by the organic component in teeth (protein and lipid) and by water. For early caries detection, the laser must have a wavelength where the transmission is at the highest level and light will scatter in the caries area or have fluorescence properties. As for caries removal or ablation, the wavelength must ensure interaction with either the mineral or the water or with both. For caries prevention, the laser should alter the mineral from a more acid soluble form to a less soluble form.

A higher absorption coefficient means smaller absorption depth. For materials with high absorption coefficients ($>100 \text{ cm}^{-1}$), the laser energy is absorbed within about $100\mu\text{m}$ of the surface and converted to heat. In the case of a pulsed laser, if the pulse duration is short, all the energy is deposited as heat in this region, whereas if it is long, some heat is deposited and the remaining energy is transmitted deeper into the tissue [Arcoria, 2005; Featherstone and Fried, 2001; Duplain et al., 1987].

For enamel, strong absorption can be seen at wavelengths in the mid-infrared spectrum region. Fig. 8 is an infrared transmission spectra of enamel illustrating the primary absorption bands at approximately $3 \mu\text{m}$, at approximately $7 \mu\text{m}$, and between 9 and $11 \mu\text{m}$. The absorption at $3\mu\text{m}$ is related primarily to water in the tissue, but there is also a spike at about $2.8 \mu\text{m}$ related to the OH^- ion in the hydroxyapatite mineral. The band at approximately $7 \mu\text{m}$ is due to the absorption of carbonate ions that substitute in dental mineral for phosphate. In the region of 9 through $11 \mu\text{m}$, the primary absorption is the phosphate ion. The carbonate ion also absorbs in the same region. This means laser light coincident with 9 to $11 \mu\text{m}$ wavelength is likely to have a rapid and major effect on the mineral. Laser light around $3 \mu\text{m}$ will have a major effect

on water. The rapid expansion and explosion of heated water will cause ablation of tissue. At wavelength in the region of 9 to 11 μm , there is also significant water absorption, so the laser light in this wavelength region will not only be absorbed in the mineral, but also in the water of the tissue. The absorption spectrum for proteins is not shown in Fig. 8, but there are specific bands due to the amide groups of the proteins also around 7 μm . Wavelengths in the near infrared and in the red region of the visible spectrum are poorly absorbed by dental mineral. At the blue end of the visible spectrum and into the ultraviolet region, absorption increases, especially in the protein components [Featherstone and Fried, 2001].

Table 13. Approximate absorption and scattering coefficients for enamel and dentin.

Wavelength	Absorption coefficient		Absorption depth (1/e)		Thermal relaxation		Scattering coefficient	
	$\mu \cdot \text{cm}^{-1}$				time, μs		$\mu \cdot \text{cm}^{-1}$	
	Enamel	Dentin	Enamel	Dentin	Enamel	Dentin	Enamel	Dentin
Visible light								
543 nm (green)	<1	3-4					105	280
632 nm (red)	<1	3-4					60	280
Near IR								
1053 nm (Nd: YAG=1064 nm)	<1	3-4					15	260
Mid IR								
2.79 μm Er:YSGG	480	*TBD	25	*TBD	220	*TBD	** ~ 0	** ~ 0
2.94 μm Er:YAG	800	*TBD	12	*TBD	90	*TBD	** ~ 0	** ~ 0
9.3 μm CO ₂	5,500	*TBD	2	*TBD	2	*TBD	** ~ 0	** ~ 0
9.6 μm CO ₂	8,000	*TBD	1	*TBD	1	*TBD	** ~ 0	** ~ 0
10.3 μm CO ₂	1,125	*TBD	9	*TBD	40	*TBD	** ~ 0	** ~ 0
10.6 μm CO ₂	825	*TBD	12	*TBD	90	*TBD	** ~ 0	** ~ 0

*TBD – to be determined. ** approximately zero – negligible – not measurable

[Featherstone & Fried, 2001]

Consequently, for caries detection it is desirable to choose wavelengths in the red or near infrared region to optimize transmission through sound tissue. For ablation, the choice is from lasers such as Er:YAG, Er:YSGG or CO₂, for which strong absorption by the tissue is found. For caries prevention purposes, the CO₂ laser is potentially useful.

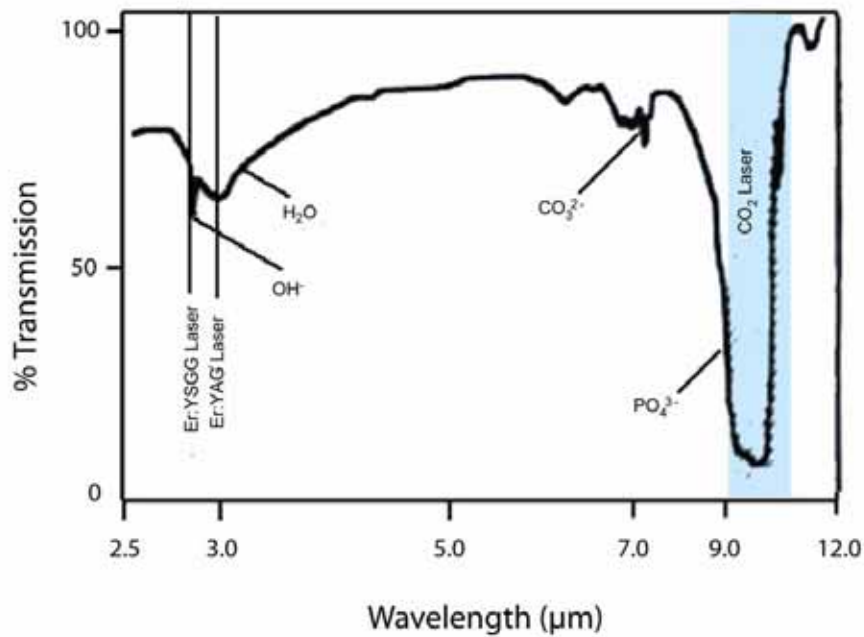


Fig. 8. Infrared transmission spectrum of dental enamel. The position of laser lines for Er:YSGG, Er: YAG, and CO₂ lasers are shown to illustrate the overlap with the absorption bands of the enamel [Fried et al. 1996].

2.3.2 Laser operating parameters

Laser interactions with tissue are complicated and no single parameter alone will determine how the laser affects the tissue. Other than wavelength, there are 7 type laser operating parameters:

- a) Energy density: The sum total of fluent energy delivered to tissue from a direct source. This parameter encompasses two factors: 1) inherent power delivered to tissue and 2) the time of exposure to the energy.
- b) Power density: The inherent power in the beam. This parameter includes the nature of the spot size, the amplitude of the wave, and the specific wavelength involved.
- c) Repetition rate: The number of times, during a given interval, that a beam is producing output onto a target. This parameter is usually measured in number of times per second that a beam produces output. Cycles per second or Hertz (Hz) are also synonyms.
- d) Pulse width: The total time that a beam is continuously producing output. This time

period determines the nature of a "true" pulsed laser vs. a gated system.

- e) Superpulse: A physical phenomenon in laser systems whereby high-peak powers, for very short time periods, are induced into tissue. In essence, the pulse width is as small as the device can physically manufacture.
- f) Q-switched: A process whereby laser energy is permitted to build up to an intense magnitude in a wait-state position, then released with high peak powers to the tissue.
- g) Total energy: The aggregate amount of energy delivered to tissue over a fixed time period.

2.3.3 Morphological changes of enamel after laser irradiation

As a result of laser interacting with dental enamel, photoablation and coagulation can change the morphology of enamel. During photoablation procedures, tissue is thermally removed when a specific wavelength of light comes into contact with it, also known as a classic light-tissue interaction that converts light energy to thermal energy because of the absorbance of the beam into a specific chromophore (pigmentation, water, hydroxyapatite, etc.) within the tissue. Results in tissue are a roughened or ulcerated appearance, generally exhibiting hemostasis. For coagulation, water and other cellular substrates from tissue are rapidly released when a specific wavelength of light interacts with it. Typical examples of this include hemostasis, tissue welding, and tissue closure [Fried et al., 1997].

Typically, a laser-irradiated enamel surface will have a temperature gradient that decreases in temperature from the irradiated point of impingement; changes in the tooth enamel along this temperature gradient are expected to be different. High energy density laser irradiant conditions cause visually observable charring and melting of tooth enamel. Even under low energy density irradiant conditions ($\sim 25\text{-}120\text{ J/cm}^2$, $10.6\mu\text{m}$ wavelength), slight surface melting has been detected which indicates very high temperatures at the tooth enamel surface [Fuhrmann et al., 2001; Kuroda and Fowler, 1984; Nelson et al., 1987; Rode et al., 2003; Jalil et al., 1997]. Impact craters with shallow centers and raised edges containing numerous pores and large, bubble-like inclusions have been observed [Hess, 1990]. Roughening of the surface,

cracks and lifting off or removal of top layer of enamel are frequently reported. Ferreira and coworkers [1989] studied the effect of a continuous wave CO₂ laser on the ultrastructure of enamel. They found enamel rods exposed, resulting from lifting off and removal of the top layer of crazed and cratered enamel. Lased enamel was also softer than unlased enamel. New homogeneous and inhomogeneous crystals of apatite with different shape and larger size than untreated enamel, and a loss of prismatic structure were found. One interesting point is that they thought the depth of the channels formed in enamel by the laser irradiation was generally more dependent on power density and irradiation time than on their product (energy density) [Mercer and Anderson, 1996; Pogrel et al., 1993; Watanabe et al., 1996; Ferreira et al., 1989]. Fuhrmann and coworkers [2001] compared the bonding tensile strength by Nd:YAG and CO₂ (10.6 μm) laser and acid etching. They concluded that laser etching was comparable to acid etching: the CO₂ laser produced craters and the Nd:YAG laser resulted in a honeycomb structure of the surface. Kuramoto et al. [2001] found that the microhardness of enamel decreased only when the input irradiation energy was larger than 30 J. All these changes differ along with different laser parameters, such as wavelength, power density, pulse width, and exposing time. In some cases, there were no observable changes at all. Wheeler et al. [2003] used a q-Switched 355nm Nd:YAG laser in the near-UV region. They reported that laser irradiation alone and topical fluoride alone did not increase the resistance to acid. The combination of laser irradiation and topical fluoride could increase the resistance to acid to 50%. Unlike CO₂ lasers which caused thermal decomposition, this laser affected protein and lipid only [Fired and Breunig, 2001; Frentzen et al. 1996; Khosroshahi and Ghasemi, 2004; Kimura et al. 1997, 2000; Wheeler et al. 2003].

2.3.4 Chemical and structural change of enamel after laser irradiation

Kinney and coworkers [1996] reported on the formation of new particles after laser irradiation indicating recrystallization. Newly formed crystals were larger and had a higher acid resistance. Pogrel et al. [1993] found structural changes in enamel induced by high energy CO₂ laser and described 3 layers: the outside layer of changed enamel is around 100μm, the middle layer is 12μm which was acid resistant amorphous, and the inside layer

was 110 μm . The width of the three zones remained constant and was independent of power density and time. In addition to water, carbonate is removed by laser irradiation. Laser irradiation was found to change the crystal phase and result in better crystal packaging, which in turn increases the resistance to caries [Oho and Morioka, 1990; Tagomori and Iwase, 1995; Wheeler et al., 2003; Wu et al., 2002; Zuerlein et al., 1999]. Aminzadeh and coworkers [1999] used Raman spectroscopy to study CO₂ laser irradiated enamel. The wavelength was 10.6 μm , pulse duration 200 ms, power 10w, power density 1700w/cm². They compared the lased enamel with heated enamel and HAP and concluded that lased enamel caused a partial conversion of HAP to TCP. Laser irradiation was not a simple local heating effect, since simple heating of enamel leads to the formation of both TCP and Ca(OH)₂, while laser treatment resulted in the formation of TCP but not Ca(OH)₂. β -TCP was one main product and OCP and α -TCP occurred at higher laser power density. The combined effect of laser and fluoride treatment and a possible formation of FAP from HAP remains unclear so far [Fried et al., 1997; Kuroda and Fowler, 1984; Kwon et al., 2005; Nelson et al., 1987; Anderson et al., 2000; Antunes et al., 2006].

Aims of this study

The laser-induced structural changes are mainly associated with the incited local heating [Palamara et al., 1992; Fowler et al., 1985]. However, the effect of monochromatic laser light differs in a certain extent from the simple heating, thus causing formation of different structural phases [Aminzadeh et al. 1999]. Besides, inhibitory effects of laser irradiation on enamel demineralization have been clearly demonstrated, although their mechanism and relationship with the local structural phenomena is still obscure [Hsu et al., 2000]. Although different morphological zones caused by high energy laser irradiation have been clearly identified, there is limited information on the atomic-scale structural changes within these zones [Pogrel et al., 1993]. The structural studies concerning laser-treated dental enamel report mostly on data collected from powdered samples or integrated over the total irradiated area.

The ability of Raman and IR spectroscopy for microprobe analysis is beneficial for studying the irradiation-induced structural transformations in enamel apatite in areas distinctly distanced from the center of the laser irradiated spot. Thus, complementary utilization of Raman and ATR IR microspectroscopy is essential to better understand the gradient of irradiation-induced changes in the atomic structure within the morphologically altered areas.

We hypothesises the laser-irradiated enamel surface will have a temperature gradient. The temperature gradient will decrease in temperature from the irradiated center to outside. Changes in enamel along this temperature gradient are expected to be different. These changes should include morphological, compositional and structural and phase change. Water, carbonate, hydroxide and possible new compounds will be examined. Raman and ATR IR microspectroscopy were applied to spatial areas of different morphology zones of laser treated human enamel. In this study, CO₂ laser will be selected as the only laser. CO₂ laser

(10.6 μm) has relative higher absorption coefficient to dental enamel and doesn't penetrate enamel deeply. This insures its efficiency of interaction with enamel and the safety of pulp without harming by high temperature. Two low energy levels will be used. Different parameter such as continuous wave mode and pulse mode, irradiation time, will be applied. Different laser parameter and their influences on enamel structure will be systematically examined. Relative high power is expected to cause bigger changes both on morphology and chemical component of enamel. An optimal laser power level which causes desirable structural changes without damage the morphology of enamel is expected. Continuous wave mode laser should have different effect on enamel compared with pulse mode laser. Longer irradiation time should change enamel more than shorter one. For comparison and as a reference, we also analyzed synthetic hydroxyapatite treated under the same conditions. Identification the overall changes and the changes along the temperature gradient will help us to understanding the interaction between laser and dental enamel, give fundamental guide to laser application in dental practice.

Chapter 3

Materials and methods

3.1 Principles of analytical methods

3.1.1 X-ray powder diffraction

X-ray powder diffraction (XRD) is used to obtain information about the structure, composition and state of polycrystalline materials. The sample may be powders, solids, films. If a monochromatic X-ray beam is directed at a crystalline material one can observe reflection or diffraction of the X-rays at various angles with respect to the primary beam. The well known Bragg equation describes the relationship between the wavelength of the X-ray beam, λ , the angle of the diffraction, 2θ , and the distance between each set of atomic planes of the crystal lattice, d (Fig. 9).

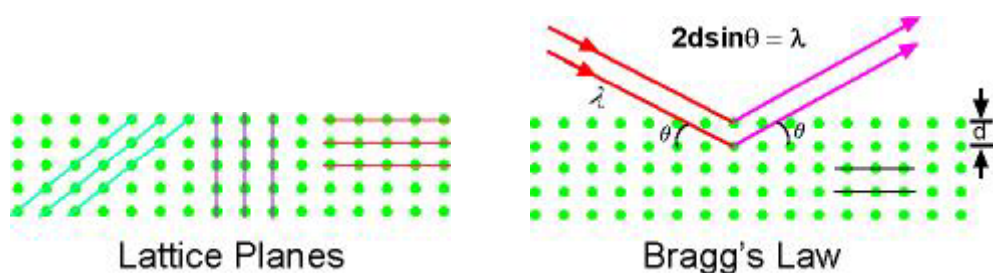


Fig. 9. X-Ray diffraction and Bragg's law

$$\text{Bragg's law: } n\lambda = 2d \sin\theta$$

where n represents the order of diffraction. From this equation the interplanar distance of the crystalline material can be calculated. The interplanar spacings depend solely on the dimension of the crystal's unit cell while the intensities of the diffracted rays are a function of the placement of the atoms in the unit cell.

The X-ray diffraction pattern of a crystalline phase is unique. An unknown phase is identified by comparing the interplanar spacings and intensities of its powder pattern to the patterns in the powder diffraction file. In addition to identification of the compounds in a powder, analysis of the diffraction pattern is also used to determine crystalline size and the degree of crystallinity of materials being studied. There are also some specific uses of powder XRD, e.g., the study of order-disorder transition using low and high temperature diffractometry; the determination of precise crystallographic lattice constants; structure determination by Rietveld refinement of a whole powder pattern [Johnson, 2005].

Powder XRD (X-ray diffraction) is perhaps the most widely used x-ray diffraction technique for characterizing materials. As the name suggests, the sample is usually in a powdery form, consisting of fine grains of single crystalline material to be studied. The technique is used also widely for studying particles in liquid suspensions or polycrystalline solids (bulk or thin film materials).

The term 'powder' really means that the crystalline domains are randomly oriented in the sample. Therefore when the 2-D diffraction pattern is recorded, it shows concentric rings of scattering peaks corresponding to the various d spacings in the crystal lattice. The positions and the intensities of the peaks are used for identifying the underlying structure (or phase) of the material. For example, the diffraction lines of graphite would be different from diamond even though they both are made of carbon atoms. This phase identification is important because the material properties are highly dependent on structure [Bish, 1989].

Powder diffraction data can be collected using either transmission or reflection geometry, as shown below (Fig. 10). Because the particles in the powder sample are randomly oriented,

these two methods will yield the same data. Data measurement in reflection mode is used mostly with solid samples while data measurement in transmission mode is more suitable for liquid phase samples [Als-Nielsen and McMorrow, 2001].

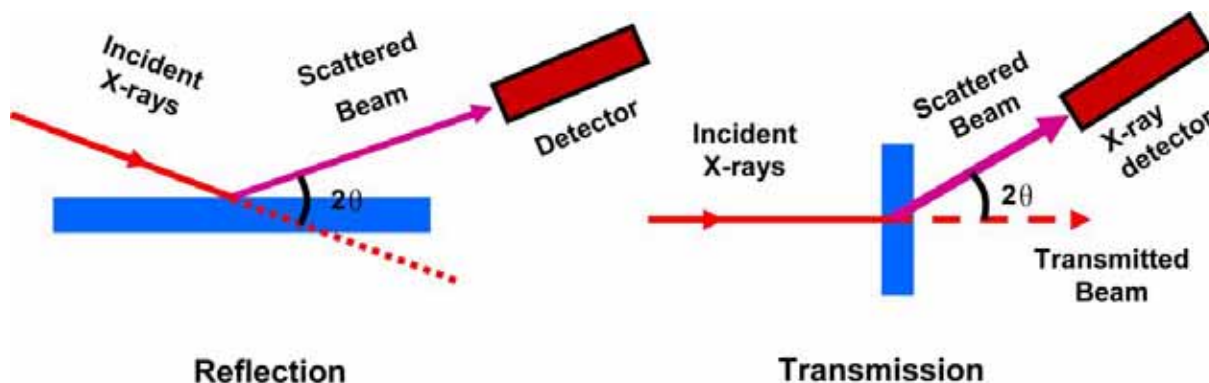


Fig. 10. Powder XRD mechanism [Als-Nielsen and McMorrow, 2001].

3.1.2 Vibrational spectroscopy

Vibrational spectroscopy involves the use of electromagnetic radiation to probe the vibrational behaviour of molecular systems via absorption or a light scattering experiment. The vibrational energy range of molecules and crystals is approximately between $0\text{-}5000\text{ cm}^{-1}$, which corresponds to the infrared region of the electromagnetic spectrum. Infrared spectroscopy (IR) studies the direct absorption of light by molecular vibrations. Raman spectroscopy or Raman scattering studies the energy changes of the incident laser light beam due to the inelastic interaction between the incident light beam and the vibrational excitation. Both infrared and Raman techniques give rise to a vibrational spectrum containing a set of absorption or scattering peaks as a function of energy. Individual peaks in the spectrum correspond to energies of vibrational transitions within the sample or to the frequencies of its vibrational modes. Vibrational spectroscopy has been qualitatively and quantitatively applied to analyse the structural or molecular group or phase in a sample in chemistry, physics,

mineralogy and many other scientific branches [Hollas, 1992; Shi, 2004].

3.1.2.1. Origins of infrared and Raman spectroscopy

In an infrared absorption experiment, infrared radiation with an intensity I_0 and frequency ν_0 is passed through a sample and the intensity of the transmitted light I is measured as a function of its frequency. Absorption of light at $\Delta E = h\nu$ occurs at frequencies corresponding to the energies of vibrational transitions. The function is described as Beer-Lambert law:

$$I = I_0 e^{-\epsilon cd}$$

Here, I_0 and I denote the intensities of the incident and transmitted beams, respectively, ϵ is the molecular absorption coefficient, and c and d are the concentration of the sample and the cell length, respectively. In IR spectroscopy, both the percentage transmission (T) or absorbance (A) are usually plotted versus the wave number. The definitions of T and A are:

$$T (\%) = I/I_0 \times 100$$

and

$$A = \log I_0/I = \epsilon cd$$

For quantitative analysis, the absorbance should be used.

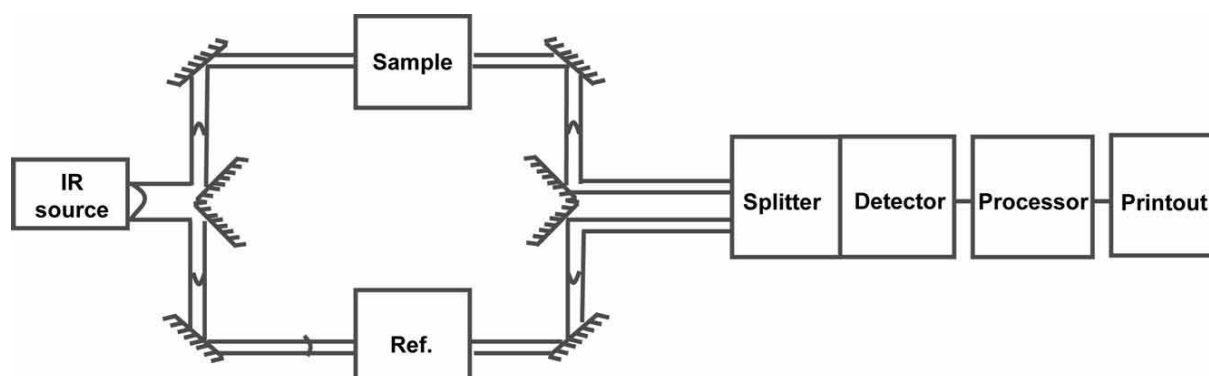


Fig. 11. Typical apparatus of IR spectroscopy.

A beam of infrared light is produced and split into two separate beams. One is passed through the sample, the other passed through a reference which is often the substance the sample is dissolved in. The beams are both reflected back towards a detector, however first they pass through a splitter which quickly alternates which of the two beams enters the detector. The two signals are then compared and a printout is obtained (Fig. 11) [Wikipedia, 2006].

The origin of Raman spectra is markedly different from that of IR spectra. In a Raman experiment, the sample is irradiated by a monochromatic laser beam (ν_0). Most of the incident light exits from the sample without change, but a small fraction (around 10^{-3} of the incident intensity) is inelastically scattered by atoms which can be observed in the direction perpendicular to the incident beam (Fig. 12). The scattered light consists of (1) Rayleigh scattering, strong and having the same frequency as the incident light beam (ν_0); (2) Raman scattering, very weak ($\sim 10^{-5}$ - 10^{-6} of the intensity of the incident laser beam) and having frequencies ($\nu_0 \pm \nu_m$), where ν_m is a vibrational frequency of a molecule. The $\nu_0 - \nu_m$ and $\nu_0 + \nu_m$ lines are called the Stokes and anti-Stokes lines, respectively. Thus the Raman lines appear as weak peaks shifted in frequency from the Rayleigh line.

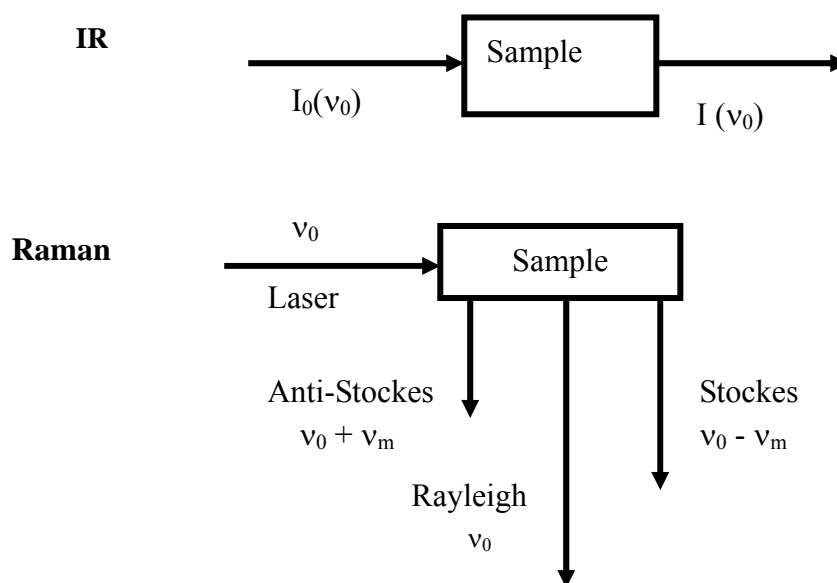


Fig. 12. Differences in mechanism of infrared and Raman spectroscopy.

3.1.2.2. Vibrational theory of molecules and crystals

a) Classical mechanical model

The model of vibrations of molecules and crystals is well established [McMillan and Hofmeister, 1988]. In this model, nuclei and the interatomic interactions are treated as point masses and springs. The atomic vibration about their equilibrium positions is described in terms of classical Newtonian mechanics. The vibrational motion is harmonic in time because the restoring force is directly proportional to displacement. Vibration corresponding to particular atomic displacement patterns (normal modes of vibrations) can be identified from the solutions of motion equations.

b) Quantum mechanical models

This advanced model describes not only the basic features of vibrational motion but also explains why vibrational spectra are line spectra rather than continuous absorptions and the interaction of vibrations with light. This model is based on Schoedinger's wave equation which is constructed in terms of the vibrational displacement coordinates q_i and a potential energy function $V(q_i)$. A set of vibrational wave function Ψ_i resolved from the partial differential equations in the vibrational wave equation describes a set of vibrational normal mode, and a set of quantized energy. In a vibrational spectroscopic experiment, a transition between vibrational levels with quantum numbers v_i and v_j is excited, and light is absorbed or emitted with an energy corresponding to the separations between the levels.

c) Crystal lattice vibration

The number of vibrational modes observed for a molecule is equal to $3N-6$ or $(3N-5$ for a linear molecule) determined by the number of degrees of vibrational freedom. In the case of crystal, N is very large, but most of the modes are not observed in infrared and Raman spectroscopy. The reason for this is the translational symmetry of the atoms in the crystal. Crystal lattice vibrations occur in the form of displacement waves travelling through the crystal. These lattice waves can be described longitudinal or transverse depending on the

nuclear displacements which are parallel or perpendicular to the wave propagation direction. The displacements of nuclei give rise to an oscillating dipole wave with the frequency equal to the oscillation frequency of individual atoms about their equilibrium positions and wavelength defined by that of the associated lattice vibration. Only the wave length of lattice vibrations is comparable to that of incident light (approximately 5×10^{-5} - 5×10^{-6} Å in IR, and usually 10^{-3} - 10^{-4} Å in Raman spectra), when an interaction of lattice vibration with incident light takes place. In these long wavelength lattice vibrations, the vibrations within adjacent unit cells are essentially in phase, so the number of vibrational modes which may be observed in IR or Raman spectroscopy is equal to $3N-3$, where N is the number of atoms in the primitive unit cell. These $3N-3$ vibrations are termed the optic modes. The three acoustic branches are responsible for the propagation of sound waves through the lattice.

3.1.2.3. Selection rules for infrared and Raman spectra

Some vibrational modes of a molecule or a crystal are IR - active and not Raman-active or vice versa, and some modes are not observable at all. To determine whether the vibration is active in the IR and Raman spectra the selection rules must be applied to each normal mode. Since the origins of IR and Raman spectra are different, their selection rules are also distinctively different. In the simple model, the selection rules can be realized by considering the interaction between the oscillating electric field vector of the light beam and a changing molecular dipole moment associated with the vibration. According to quantum mechanics, a vibration is IR-active if the dipole moment is changed during the direct interaction of light beam with an oscillating molecular dipole. In general, asymmetric vibrations tend to give stronger infrared absorption than symmetric species. Similarly highly polar molecules and crystals have stronger infrared spectra than non-polar samples.

In Raman scattering, the light beam induces an instantaneous dipole moment in molecule by deforming its electronic wave function. If the polarizability is changed during vibration, then this vibration is Raman-active. In general, molecules containing easily polarizable atoms (such as I, S, Ti) have very strong Raman spectra, while similar molecules with less

polarizable atoms (Si, C, O) have weaker spectra. Most symmetric modes tend to give the strongest Raman signals as these are associated with the largest changes in polarizability.

For more complicated molecules and crystals, IR and Raman activities of vibrational modes can be simplified by use of the molecular or unit cell symmetry, and the method of group theory [McMillan and Hofmeister, 1988]

3.1.2.4. Comparison of infrared and Raman spectroscopy

Although IR and Raman spectroscopies are similar in that both techniques provide information on vibrational frequencies, there are many advantages and disadvantages inherent to each spectroscopic technique.

- 1) Some vibrations are inherently weak in IR and strong in Raman spectra. Vibrations are generally strong in Raman if the bond is covalent and strong in IR if the bond is ionic.
- 2) Depolarisation ratios measured using Raman provide reliable information about the symmetry of a normal vibration which is difficult to obtain by IR.
- 3) The laser source of Raman spectroscopy can focus on a spot around 1 μm compared to 20 μm of IR light source, this is a great advantage for small quantity of samples.
- 4) Water is a weaker Raman scatterer and stronger IR absorber, Raman is ideal for studies of biological compounds in solutions.
- 5) In Raman spectroscopy, the region from 4000-50 cm^{-1} can be covered by a single recording while in IR grating, beam splitter and detector must be changed to cover the same region.
- 6) Local heating or photo decomposition may be caused by a high power laser source in Raman spectroscopy and fluorescence occurs in some samples when irradiated by the laser beam.

It should be noted that vibrational spectroscopy is unique in that it is applicable to solid state, gaseous state and solution. The combination of IR and Raman can provide more information on molecular structures in the sample than other techniques which usually integrate on larger

time and length scales [Hollas, 1992].

3.1.2.5. Fourier transform infrared (FTIR) spectroscopy

Fourier transform infrared (FTIR) spectroscopy is a measurement technique for collecting infrared spectra. Instead of recording the amount of energy absorbed when the frequency of the infra-red light is varied (monochromator), the IR light is guided through an interferometer. After passing the sample the measured signal is the interferogram. Performing a mathematical Fourier transform on this signal results in a spectrum identical to that from conventional (dispersive) infrared spectroscopy.

FTIR spectrometers are cheaper than conventional spectrometers because building of interferometers is easier than the fabrication of a monochromator. In addition, measurement of a single spectrum is faster for the FTIR technique because the information at all frequencies is collected simultaneously. This allows multiple samples to be collected and averaged together resulting in an improvement in sensitivity. Because of its various advantages, virtually all modern infrared spectrometers are FTIR instruments.

3.1.2.6. Attenuated total reflectance infrared spectroscopy (ATR-IR)

Attenuated total reflection infrared (ATR-IR) spectroscopy is used for analysis of the surface of materials. It is also suitable for characterization of materials which are either too thick or too strong absorbing to be analyzed by transmission spectroscopy. For the bulk material or thick film, no sample preparation is required for ATR analysis.

For the attenuated total reflection infrared (ATR-IR) spectroscopy, the infrared radiation is passed through an infrared transmitting crystal with a high refractive index, allowing the radiation to reflect within the ATR element several times (Fig.13).



Fig. 13. Sceme of ATR experiment

The sampling surface is pressed into intimate optical contact with the top surface of the crystal such as ZnSe or Ge. The IR radiation from the spectrometer enters the crystal. It then reflects through the crystal and penetrates “into” the sample a finite amount with each reflection along the top surface via the so-called “evanescent” wave. At the output end of the crystal, the beam is directed out of the crystal and back into the normal beam path of the spectrometer.

To obtain internal reflectance, the angle of incidence must exceed the so-called ‘critical’ angle. This angle is a function of the real parts of the refractive indices of both the sample and the ATR crystal:

$$\theta_c = \sin^{-1} (n_2/n_1)$$

Where n_2 is the refractive index of the sample and n_1 is the refractive index of the crystal. The evanescent wave decays into the sample exponentially with distance from the surface of the crystal over a distance on the order of microns. The depth of penetration of the evanescent wave d is defined as the distance from the crystal-sample interface where the intensity of the evanescent decays to $1/e$ (37%) of its original value. It can be given by:

$$d = \lambda / \{2\pi n_1 [\sin^2 \theta - (n_2/n_1)^2]^{1/2}\}$$

Where l is the wavelength of the IR radiation. The depth of penetration and the total number of reflections along the crystal can be controlled either by varying the angle of incidence or by selection of crystals. Different crystals have different refractive index of the crystal material. Different crystals are applied to different transmission range [Hollas, 1992].

3.2 Materials

3.2.1 Reference samples

Since enamel is mainly carbonated hydroxyapatite, synthetic hydroxyapatite was used as a reference material: pellets of dense ceramic CO_3 -poor hydroxyapatite with a grain size of 1-3 μm (Berkeley Advanced Biomaterials, U.S.A.) were prepared. Pellets were fitted in resin with up-surface polished.

3.2.2 Dental enamel

Bovine dental enamel

Bovine lower incisor teeth are often used to investigate dental enamel in vitro. Bovine teeth are easy to obtain, and have a bigger surface area than human teeth. Because bovine enamel and dentin develop more rapidly during tooth formation, bovine enamel has larger crystal grains and more lattice defects than human enamel. This may contribute to a lower critical surface tension in bovine enamel than in human enamel. Despite the difference, bovine enamel has been reported to be a reliable substitute for human enamel in bonding studies with no statistically significant difference in enamel bond strength, although values were found to be slight lower [Sydney-Zax et al., 1990; Oesterle et al., 1998]. For the present study, bovine lower incisors from a nearby slaughter house were cut into thin slices (around 5×10 mm, 2 mm thickness) and one surface was finely polished for laser irradiation.

Human dental enamel

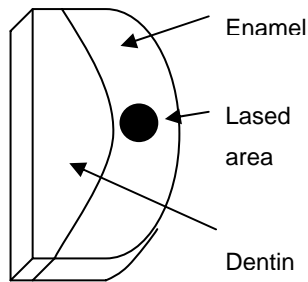


Fig. 14. Human enamel sample with lased area.

Extracted human molars were used in our present investigation. The extracted teeth were stored in 0.5% chloramine solution prior to the experiment. To facilitate the optical microspectroscopic measurements, we prepared cross-section tooth cuts with two mutually parallel sides, approximately 4×8 mm, 2mm thick, one side finely polished.

3.3 Laser treatment

3.3.1 Technical specification of the CO₂ laser

As described earlier, CO₂ lasers have the wavelength that is most strongly absorbed by the mineral, carbonate and water in dental enamel. For this reason, the CO₂ laser was used as the irradiation source. In this study, the feasibility of using CO₂ laser as a tool to modify dental enamel was investigated. While CO₂ lasers with a wavelength of 9.3 and 9.6 μm have a higher absorption coefficient, CO₂ lasers with 10.6 μm wavelength are more readily commercially available and the absorption coefficient is high enough compared with other types of lasers. When pulse mode is applied, the competition of pulse duration and enamel thermal relaxation time is another fact that needs to be taken into account [Schouten, 1999; Nelson et al., 1986; Zuerlein et al., 1999].

The Opus Duo (OpusDent, Santa Clara, U.S.A.) dental laser is a dual laser source system (see Fig. 15). The Er:YAG source has a wavelength of 2.94 μm with a red diode laser as aiming beam. The CO₂ laser was used in this study operating at 10.6 μm in either super pulse (SP) or continuous wave (CW) mode, with a diameter of the focused beam of 600 μm . The duration of the pulse in the SP mode was 125 μs , with a pulse repetition rate of 400 Hz (pulse on/off=5:100). This apparatus was designed for dental soft tissue ablation, enamel etching and removal of caries.

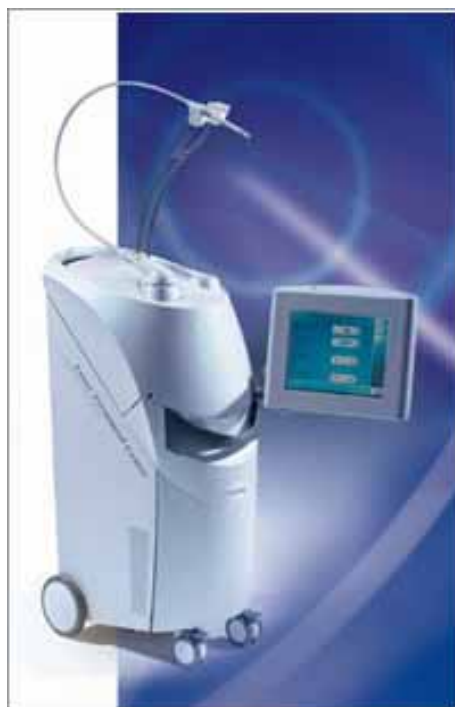


Fig. 15. Opus Duo dental CO₂ laser.

3.3.2 Laser irradiation parameters

Both continuous wave and super pulse modes were applied at low laser power (1 and 3 W). The CO₂ laser pulse duration was 125 μs . Irradiation times were short (5 and 10 s) in order to match the clinical situation. Irradiation was performed at a working distance of 5 mm between the tip of the laser and the enamel in order to simulate the clinical intraoral environment during laser irradiation of dental hard tissue. For clarity, the laser-treatment parameters are

included in the designation of samples subjected to microspectroscopy as S(P|t|m), where S stands for E (human enamel) and A (hydroxyapatite) and B (Bovine), P is the power setting in watts, t is the time of laser treatment in seconds and m denotes the laser mode, p for SP and c for CW (Table 14).

Additionally, a large area of enamel was irradiated in super-pulse mode for 5 s with a laser power set at 3 W and, subsequently the phase composition of the irradiated dental enamel collected from the surface was checked by powder X-ray diffraction (XRD).

Table 14. Sample Nomenclature and Laser-Irradiation Parameters

Sample	Type of Material	Laser Power (W)	Treatment Time (s)	Laser Mode
E(1 5 p)	Human enamel	1	5	Super pulse
E(1 10 p)	Human enamel	1	10	Super pulse
E(3 5 p)	Human enamel	3	5	Super pulse
E(1 5 c)	Human enamel	1	5	Continuous wave
E(1 10 c)	Human enamel	1	10	Continuous wave
E(3 5 c)	Human enamel	3	5	Continuous wave
A(1 5 p)	Synthetic hydroxyapatite	1	5	Super pulse
A(1 10 p)	Synthetic hydroxyapatite	1	10	Super pulse
A(3 5 p)	Synthetic hydroxyapatite	3	5	Super pulse
A(1 5 c)	Synthetic hydroxyapatite	1	5	Continuous wave
A(1 10 c)	Synthetic hydroxyapatite	1	10	Continuous wave
A(3 5 c)	Synthetic hydroxyapatite	3	5	Continuous wave
B(1 5 p)	Bovine enamel	1	5	Super pulse
B(3 5 p)	Bovine enamel	3	5	Super pulse
B(3 5 c)	Bovine enamel	3	5	Continuous wave

3.3.3 Sample analysis

a) The morphology of the irradiated areas was investigated by reflectance optical

microscopy using a Leica DMRXP microscope equipped with a Leica DC 500 digital camera.

b) The Raman spectra were measured in backscattering geometry with a triple-grating spectroscopic system Horiba Jobin-Yvon T64000 equipped with an Olympus BH2 microscope. The Raman scattering was excited with the 514.5-nm line of an Ar⁺ laser. No analyzer was used on the scattered light. The achieved spectral resolution was 2 cm⁻¹. The use of a 50× objective led to a spatial resolution of ~2.5 μm and a laser power on the sample surface of 7 mW. The as-measured Raman spectra were subsequently corrected for the continuous luminescence background, using a nine-power polynomial function. The apatite crystallites in enamel are preferentially oriented with their crystallographic c-axis perpendicular to the enamel-dentine junction, which results in different Raman scattering intensity depending on the experimental geometry. Thus, to verify the crystallite orientation inside and in the vicinity of the CO₂-laser spot we measured the Raman spectra of enamel apatite in two different experimental geometries - when the enamel-dentine junction was parallel and perpendicular to the polarization of the incident light E_i, that is, when the crystallographic c-axis of apatite was near perpendicular and near parallel to E_i, respectively (Fig. 16).

c) The ATR IR spectroscopic measurements were performed with a Bruker 66v/S FTIR spectrometer equipped with a Bruker IRscope II microscope with a Ge ATR crystal objective and a liquid N₂-cooled MCT midband detector. The spectra were collected in a dry N₂-purged chamber, with a spectral resolution of 4 cm⁻¹, by pressing the ATR crystal onto the sample with a force of 8 N and averaging over 1024 scans. The spatial resolution of the experiment, determined from the linear size of the Ge-crystal surface and the used aperture, was 90 μm, whereas the penetration depth was ~700 nm (Fig. 17).

d) Powder X-ray diffraction data were collected at room temperature. Samples from unlased and lased enamel (3 W, 5 s, super pulse mode) were prepared by scraping off the enamel surfaces with a steel bar. These samples were powdered by grinding with an agate mortar. The samples were analyzed in the 2θ range 5-80° using a Philips X'pert diffractometer with CuK_{α1}(λ=1.5405Å) radiation (Fig.18).



Fig. 16. Horiba Jobin-Yvon T64000 Raman Microspectroscopy.



Fig. 17. Bruker 66v/S FTIR spectrometer equipped with a Bruker IRscope II microscope with a Ge ATR crystal objective and a liquid N₂-cooled MCT midband detector.

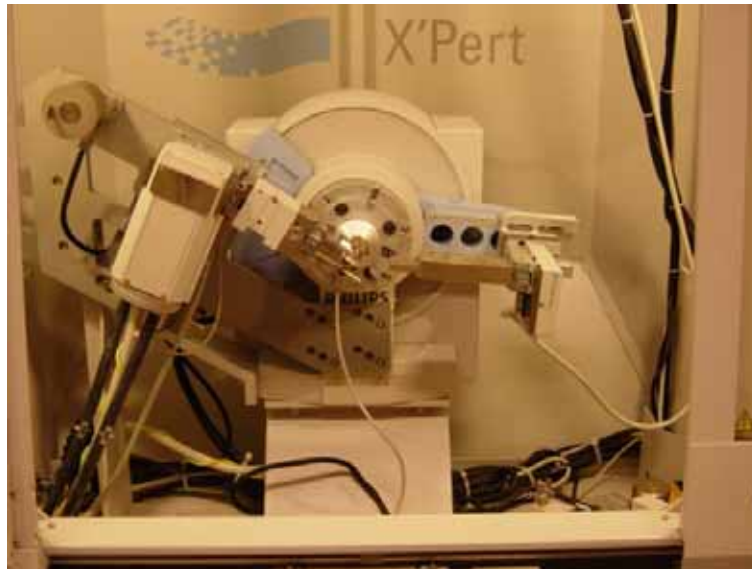


Fig. 18. Philips X'pert diffractometer.

Chapter 4

Results

4.1 Morphological changes of lased human enamel

The laser-induced morphological alteration of human dental enamel is shown in Fig. 19 – Fig. 22. The size of the morphologically altered area varies between 750 and 1250 μm . The highest depth of crater is around 500 μm (at 3 Watt power). When a CO_2 -laser power of 1 W was applied, two main zones could be distinguished - a darker zone at the centre of the laser spot and a brighter zone at the laser-spot periphery, displaying a granular morphology (see Fig. 19 and Fig. 20). For this magnitude of the CO_2 -laser power, the prolongation of the irradiation time from 5 to 10 s slightly enhances the crazing when SP mode is used, whereas no substantial morphological differences are observed in CW mode. Under the higher laser power, a crater is formed, which exhibits three morphologically distinguishable zones: (i) a zone with a melted-like appearance at the centre of the laser crater; (ii) a zone of wavy-like morphology at the slope of the laser crater; (iii) a zone of granular morphology in the vicinity of the laser-crater rim (Fig. 19, Fig. 21 and Fig. 22).

As described in Chapter 2, enamel is composed of mineral rods sized $\sim 30 \mu\text{m}$ in length and 5 μm in diameter that are oriented roughly perpendicular to the dentin-enamel junction. In turn, the rods are built up of crystallites sized $\sim 1 \mu\text{m}$ in length and 40 nm in diameter and aligned with their crystallographic c-axis along the rod length. Water and organics that fill the intercrystallite and interrod space may partially or entirely evaporate because of the local heating caused by the laser-induced temperature waves [Zuerlein et al., 1998]. Thus the “granular-like” morphology observed in the optical images should be related to release of the interrod substance in the close vicinity of the areas directly exposed to the laser action. When enamel is heated well above its melting and vaporization temperatures, which are in the range 1570-2270 K, molten droplets occur on the surface of enamel [Fried et al., 1998]. Such

molten droplets were observed for the samples irradiated with 3 W (Fig. 21 and Fig. 22), that is, the outermost surface layers were ablated under the laser irradiation. The observed wavy-like morphology at the slopes of the craters represents most probably the fronts of the ablation waves.

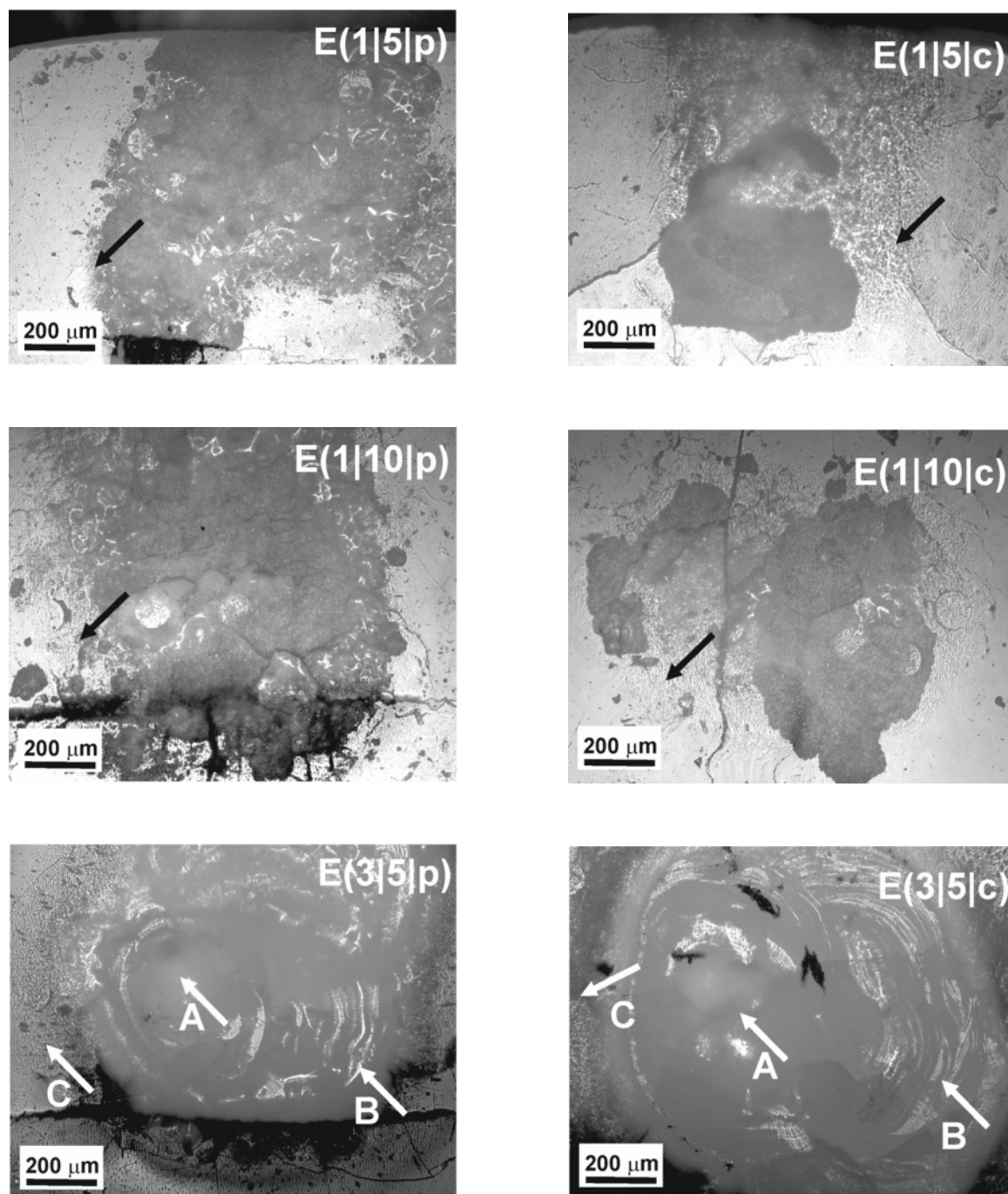


Fig. 19. Optical images of the laser spot on the enamel surface; magnification $\times 100$. Black arrows point to zones of granular morphology observed in the periphery of the CO₂-laser spot; the white arrows point to morphologically distinguished zones in samples E(3|5|p) and E(3|5|c); A, centre of the laser crater; B, wavy areas on the slope of the laser crater; C,

granular morphology in the vicinity of the laser-crater rim.

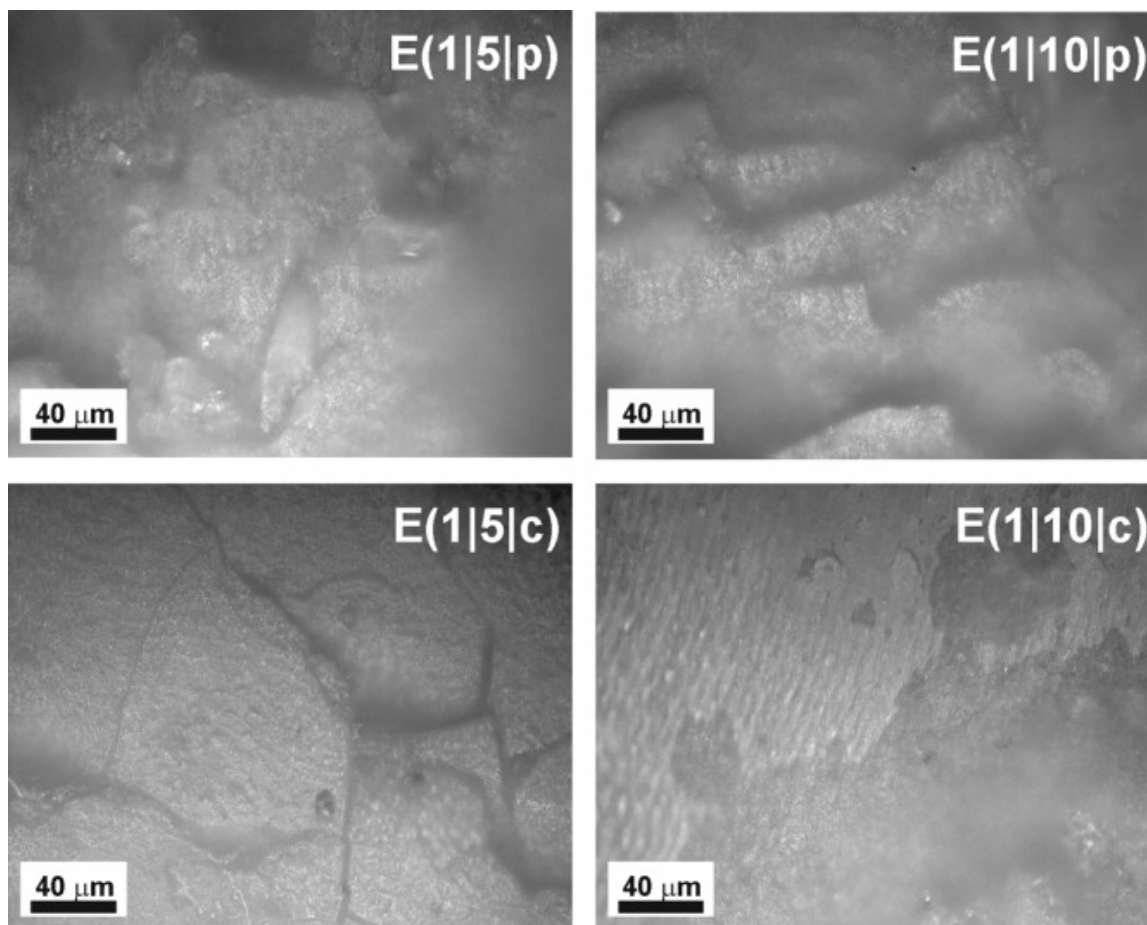


Fig. 20. Typical optical images of enamel irradiated with a power of 1 W; magnification $\times 500$. The micrographs of E(1|5|p), E(1|5|c), and E(1|10|p) are taken from the centre of the laser spot; the micrograph of E(1|10|c) is from the peripheral area, where the granular morphology is better pronounced. The appearance of the central part of E(1|10|c) is nearly the same as that for E(1|10|p). No differences in appearance of the peripheral granular zones of the four samples E(1|t|m) were observed.

4.2 Structural changes in synthetic hydroxyapatite

Prior to characterize the different morphological zones observed in irradiated enamel, the laser-induced structural alteration in dense pellets of synthetic hydroxyapatite irradiated under different conditions was analyzed. For this series of samples, no distinct zones could be

visually identified within the laser spot. Since the dense pellets are not as dense as enamel, the crystals in these pellets are not well packaged and lack uniform orientation.

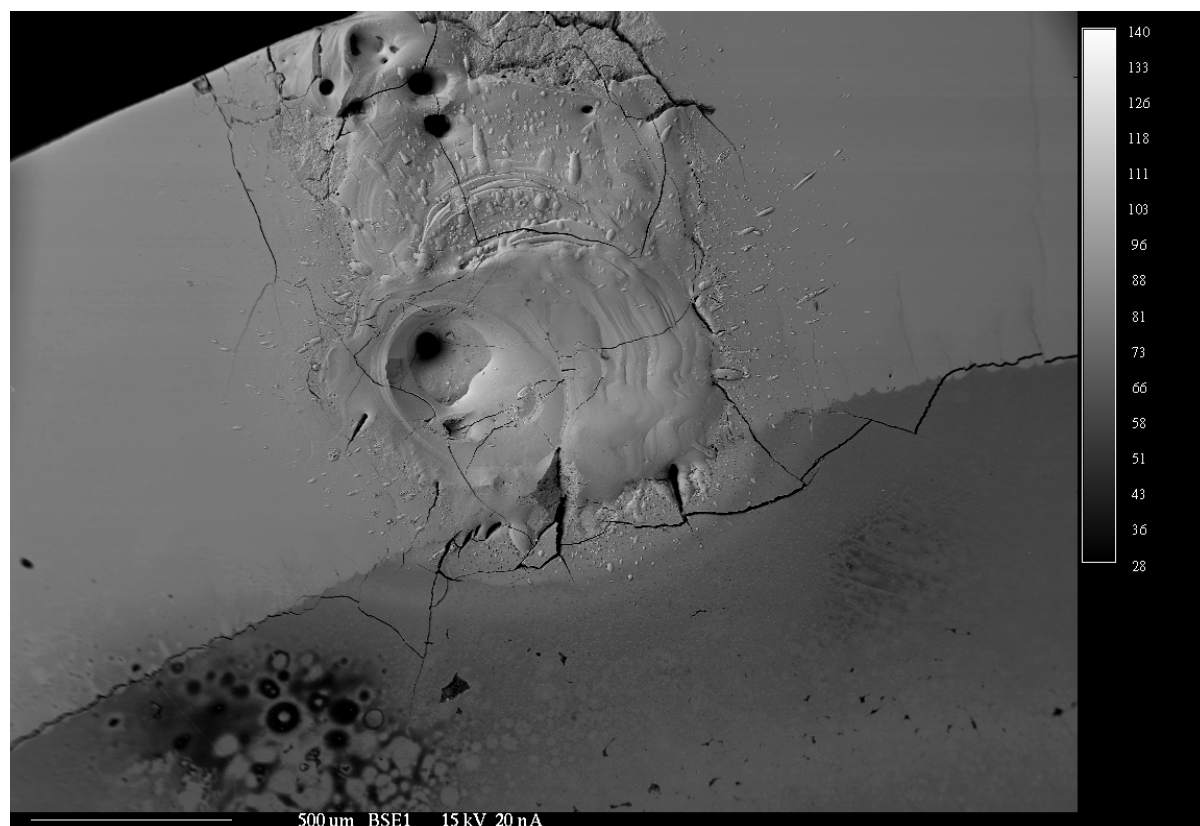


Fig. 21. Backscattered electron (BSE) image of sample E(3|5|p), enamel irradiated at 3W, 5s, sp mode. Image is taken by a Camebax microbeam SEM-system. Cracks are found in the whole irradiated area. Both shallow and deep craters are found on the enamel surface. Sputtered droplets can be seen. This is the condensate of ejected molten mineral when the threshold of enamel melting around 1280 °C was achieved. The wavy-like morphology at the slopes of the craters represents most probably the fronts of the ablation waves. A similar result has been reported by Mercer and Anderson [1996] and Nelson et al. [1987].

Tables 15, 16 and 17 show the general internal vibration modes of PO_4^{3-} , CO_3^{2-} and CO_2 . This helps understand the Raman and IR spectrum. The phosphate ion has the following vibration frequencies: a symmetric stretch (ν_1), a double degenerate symmetric bend (ν_2), a triply degenerate asymmetric stretch (ν_3), and a triply degenerate asymmetric bend (ν_4). The symmetric vibrations are both infrared and Raman active, whereas the asymmetric ones are mostly Raman active. The free carbonate ion has six modes of vibration: a symmetric

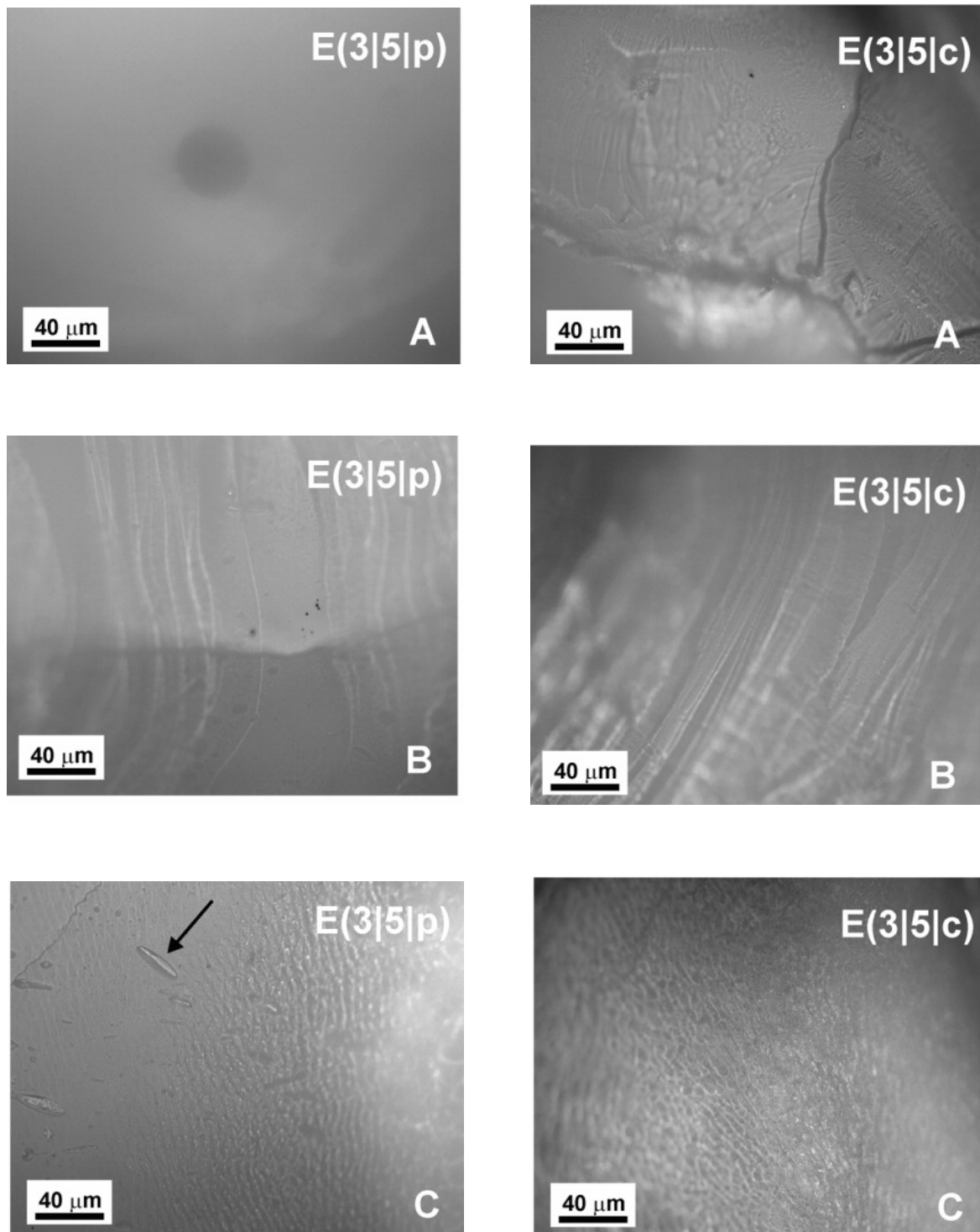


Fig. 22. Optical images of morphologically distinguished zones of enamel irradiated with 3 W; magnification $\times 500$. Micrographs (A), (B), and (C) correspond to areas pointed in Fig.19. The arrow in (C) points to molten droplets formed as a result of enamel ablation. Small well-rounded craters were observed more frequently at the central zone of E(3|5|p) than of E(3|5|c).

stretching vibration (ν_1), an out of plane vibration (ν_2) a doubly degenerate asymmetric stretch (ν_3), and a doubly degenerate bending mode (ν_4) [Santos and Clayton, 1995; Fowler, 1974]. Tables 18, 19 and 20 give the reference IR absorption and Raman shift for HAP, CAP. This helps to pick up the bands assigned to the HAP or enamel vibrations in present study.

Fig. 23 displays the Raman scattering collected from the centre of the CO₂-laser spot of synthetic hydroxyapatite. The Raman spectra of samples A(1|5|c) and A(1|10|c) are almost identical to that of A(3|5|c). The most intense Raman peak at 962 cm⁻¹ is generated by the symmetrical stretching mode of PO₄ groups [Penel et al., 1998]. There are two signals untypical for apatite in the spectrum of the nonirradiated sample, the shoulder at 951 cm⁻¹ and the weak additional scattering near 970 cm⁻¹, indicating variations in the P—O bond lengths. Substantial changes in the Raman scattering are observed for A(3|5|p): (i) a strong intensification of the peak near 970 cm⁻¹ on the account of diminishment of the peak at 962 cm⁻¹; (ii) a merging of the peaks at 1000-1100 cm⁻¹ related to the antisymmetrical PO₄ stretching modes into one unstructured halo; (iii) a strong broadening of the peaks near 440 and 600 cm⁻¹ derived from the PO₄ bending modes. The suppression of the major apatite peak as well as the loss of resolved peaks is evident for structural amorphization. Apparently, the peak at 970 cm⁻¹ originates from noncrystalline substance and thus its relative intensity can be used for estimation of the fraction of amorphous phases. Raman spectra were collected with a different intensity ratio of the peaks at 962 and 970 cm⁻¹ and a different degree of peak broadening within the CO₂-laser spot of A(3|5|p), which points to a significant structural inhomogeneity. The spectrum shown in Fig. 23 is taken from a spatial area revealing the highest degree of structural amorphization. The shoulder at 951 cm⁻¹ remains nearly unchanged under the CO₂-laser treatment, that is, it is not directly related to the amorphous material. An increase in the structural disorder revealed by the variation in the intensity ratio $I(970)/I(962)$ is observed also for A(1|10|p), whereas according to the Raman scattering data samples A(3|5|c) and A(1|10|c) are barely affected by the laser irradiation. Therefore, the CW laser mode has a much weaker effect on the atomic structure of synthetic hydroxyapatite.

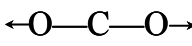
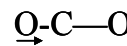
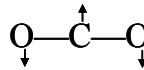
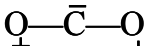
Table 15. Internal vibration modes of PO_4^{3-} ion.

$\text{P6}_3/\text{m}$	Mode	Symmetry species	Frequency cm^{-1}	Activity
Point group symmetry PO_4^{3-} ion (T_d)	ν_1 P-O symmetric stretch	A_1	938	R
	ν_2 O-P-O bend	E	420	R
	ν_3 P-O asymmetric stretch	F_2	1017	R+IR
	ν_4 O-P-O bend	F_2	567	R+IR
Site group symmetry (C_s)	$5A' (R+IR) + 4A''(R+IR)$			
Factor group symmetry (C_{6h})	$5A_g(R) + 5E_{2g}(R) + 5B_u(0) + 5E_{1u}(\text{IR}) + 4B_g(0) + 4E_{1g}(R) + 4E_{2u}(0) + 4A_u(\text{IR})$			

Table 16. Internal vibration modes of CO_3^{2-} ion.

Vibration mode						
Frequency	ν_1 1063 cm^{-1}	ν_2 879 cm^{-1}	ν_{3a} 1415 cm^{-1}	ν_{3b} 1415 cm^{-1}	ν_{4a} 680 cm^{-1}	ν_{4b} 680 cm^{-1}
Activity	D_{3h} : A_1'	R	IR	A_2''	IR+R	IR+R
Symmetry species	C_{2v} : A_1	R	IR+R	B_1	IR+R	IR+R
		A_1	IR+R	A_1	IR+R	IR+R
			IR+R	B_2	IR+R	IR+R
			IR+R	A_1	IR+R	IR+R
			IR+R	B_2	IR+R	IR+R

Table 17. Internal vibration modes of CO₂.

				
	ν_1	ν_3	ν_{2a}	ν_{2b}
Frequency	1337 cm ⁻¹	2349 cm ⁻¹	667 cm ⁻¹	667 cm ⁻¹
Activity	Raman	IR	IR	IR
Vibration mode	Symmetric stretch	Asymmetric stretch	Symmetric bend	Symmetric bend

The ATR spectra of synthetic hydroxyapatite (Fig. 24) are in accordance with the Raman spectroscopic results. For the samples treated in SP mode, one observes poorly resolved 2nd order absorption peaks (1900-2200 cm⁻¹), which give further evidence for a lowering of the degree of crystallinity. In addition, the strong decrease in intensity of the peak at 3575 cm⁻¹ for the samples irradiated in SP mode points to a substantial decrease in the content of the OH groups occupying the (2a) Wyckoff position of apatite. The broad band between 3000 and 3500 cm⁻¹ originating from the H₂O stretching modes changes under certain laser-treatment parameters, independently of the applied CO₂ laser mode. As expected, it decreases in intensity, that is, the water content is reduced, when the samples are treated at 1 W for a longer time (10 s). The increase in intensity for the samples treated at 3 W is most probably due to physisorbed water in cavities formed under a higher-fluence laser treatment. An additional IR absorption peak at 3750 cm⁻¹ is observed for irradiated hydroxyapatite, as it is better pronounced in the spectra of samples treated at 3 W. This peak was ascribed to terminal OH groups on the surface of the apatite grains and similarly to the peak observed at the same wavenumber in silicates [Montanari et al., 2004]. Hence, its intensity is related to the size of the apatite grains; an increase in the intensity indicates an increase in the ratio between the surface area and the bulk volume, that is, reduction of the grain size under irradiation. Thus, both Raman and ATR IR spectroscopic data point out that the super-pulse irradiation causes heavier damages on the structure of hydroxyapatite than the continuous-wave irradiation.

Table 18. Infrared absorption spectroscopy for HAP; Bands and assignments

Peak (cm ⁻¹)	Assignment
3572 (w)	Stretching mode, ν_s , of the hydroxyl group
2070 (w)	Harmonic overtone or combination band
2000 (w)	Harmonic overtone $2 \cdot \nu_3$ or combination band $\nu_1 + \nu_{3b}$
1154 (w)	Harmonic overtone or combination band
1087 (s)	Triply degenerated asymmetric stretching mode, ν_{3a} , of the P–O bond of the phosphate group
1046 (s)	Triply degenerated asymmetric stretching mode, ν_{3b} , of the P–O bond of the phosphate group
1032 (sh)	Triply degenerated asymmetric stretching mode, ν_{3c} , of the P–O bond of the phosphate group
962 (w)	Nondegenerated symmetric stretching mode, ν_1 , of the P–O bonds of the phosphate group
631 (m)	Librational mode, ν_L , of the hydroxyl group
602 (s,shp)	Triply degenerated bending mode, ν_{4a} , of the O–P–O bonds of the phosphate group
574 (s,sh)	Triply degenerated bending mode, ν_{4b} , of the O–P–O bonds of the phosphate group
561 (s)	Triply degenerated bending mode, ν_{4c} , of the O–P–O bonds of the phosphate group
472 (w)	Double degenerated bending mode, ν_{2a} , of the O–P–O bonds of the phosphate group
462 (w,sh)	Double degenerated bending mode, ν_{2b} , of the O–P–O bonds of the phosphate group
361 (w,sh)	HAP lattice vibration mode or combination band, $\nu_1 - \nu_4$
355 (sh)	Translational mode, ν_T , of the hydroxyl group (ν_3)
342 (w,sh)	Translational mode, ν_T , of the hydroxyl group (ν_3)

w: weak, m: medium, s: strong, sh: shoulder, shp: sharp [Koutsopoulos, 2002]

Table 19. Infrared absorption spectroscopy data for carbonate apatite, CAP.

Peak (cm ⁻¹)	Assignment
1550	Bending mode (ν_4) of the CO ₃ ²⁻ group in A-type CAP
1500	Characteristic stretching mode (ν_3) of the CO ₃ ²⁻ group in CAP
1465	Characteristic stretching mode (ν_1) of the CO ₃ ²⁻ group in A-type CAP
1452–5	Bending mode (ν_4 or ν_3) of the CO ₃ ²⁻ group in A and B-type CAP
1430	Stretching mode (ν_1) of the CO ₃ ²⁻ group in B-type CAP
1410–5	Stretching mode (ν_3) of the CO ₃ ²⁻ group in CAP
1110	Due to the presence of CO ₃ ²⁻ in nonstoichiometric apatites
1020	Due to the presence of CO ₃ ²⁻ , HPO ₄ ²⁻ and crystal imperfections in nonstoichiometric apatites
883	Characteristic bending mode (ν_6 or ν_2) of the CO ₃ ²⁻ group in A-type CAP
875	Bending mode (ν_4 or ν_3) of the CO ₃ ²⁻ group in CAP
870	Bending mode (ν_2) of the CO ₃ ²⁻ group in CAP
864	Stretching mode (ν_3) of the CO ₃ ²⁻ group in CAP

[Koutsopoulos, 2002]

Table 20. Raman shifts observed and assignment for HAP

Peak (cm ⁻¹)	Assignment
1076 (w), 1054 (w), 1046 (m), 1030 (w)	Triply degenerate asymmetric stretching mode (ν_3) of the PO ₄ group (P–O bond)
961 (vs)	Totally symmetric stretching mode (ν_1) of the tetrahedral PO ₄ group (P–O bond)
620 (vw), 610 (w), 594 (m), 582 (w)	Triply degenerate bending mode (ν_4) of the PO ₄ group (O–P–O bond)
447 (m), 433 (w)	Doubly degenerate bending mode (ν_2) of the PO ₄ group (O–P–O bond)

v: very, w: weak, m: medium, s: strong, sh: shoulder [Koutsopoulos, 2002]

4.3 Structural changes in human enamel

We applied Raman and IR microspectroscopy to irradiated human enamel. Fig. 25 shows the Raman spectra of samples exposed to a laser power of 1 W. The spectra were measured from areas at the centre of the CO₂-laser spot, which appear darker in the optical images.

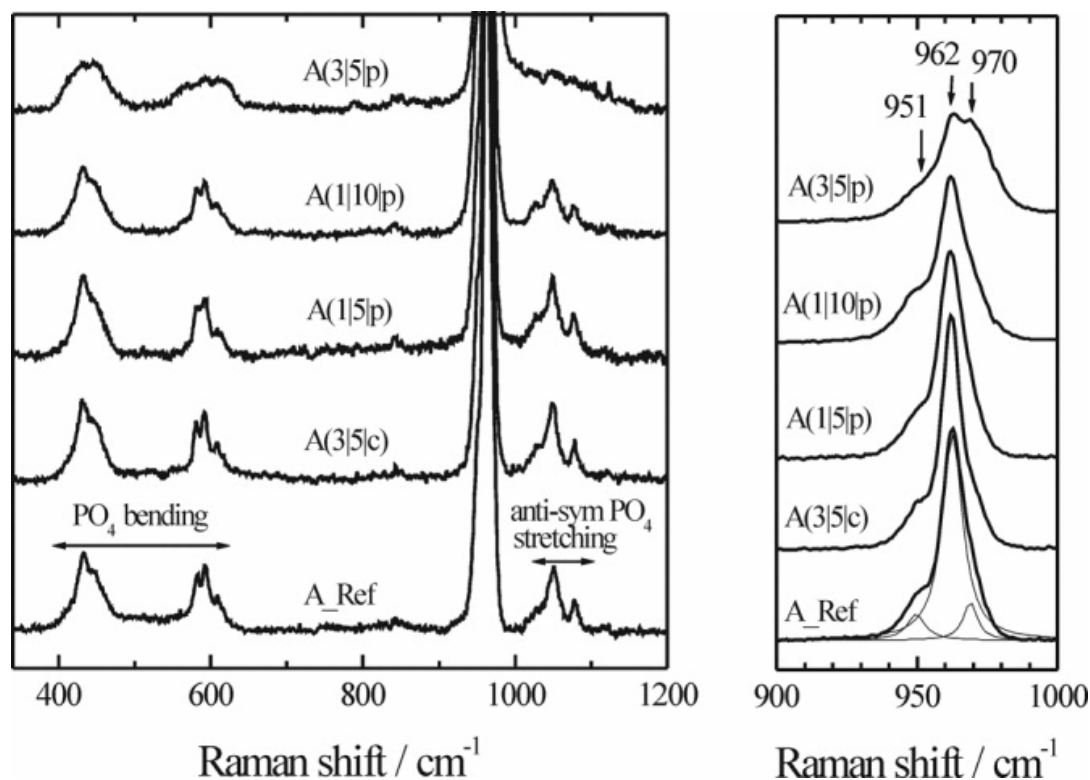


Fig. 23. Raman spectra of synthetic hydroxyapatite irradiated under different conditions. The Raman spectra of samples A(1|5|c) and A(1|10|c) are nearly the same as that of A(3|5|c).

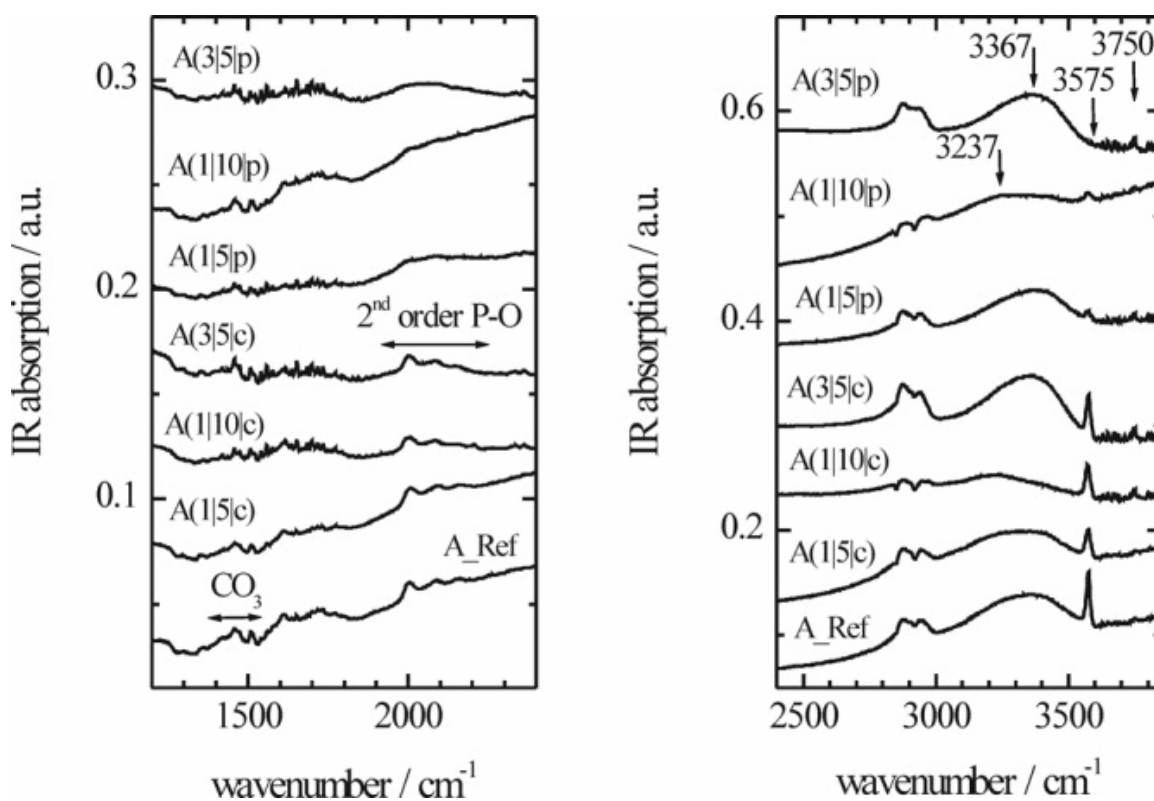


Fig. 24. Infrared absorption spectra of synthetic hydroxyapatite irradiated under different conditions; the spectra are vertically shifted for clarity.

To verify the sensitivity of the Raman probe to the orientation of the enamel apatite crystallites, we also measured the Raman scattering of a single crystal of fluorapatite with a well-defined crystal habitus (Fig. 26). The orientation dependence is best pronounced in the spectral ranges 580-620 and 1010-1080 cm^{-1} resulting from the asymmetrical bending and stretching modes of the PO_4 tetrahedra, respectively [Penel et al., 1998]. The preferred orientation of the apatite crystallites in nonirradiated enamel can be deduced from both spectral ranges, although the peak at 1070 cm^{-1} generated by carbonate groups [Markovic et al., 2004] partially overlaps the antisymmetrical stretching modes of PO_4 .

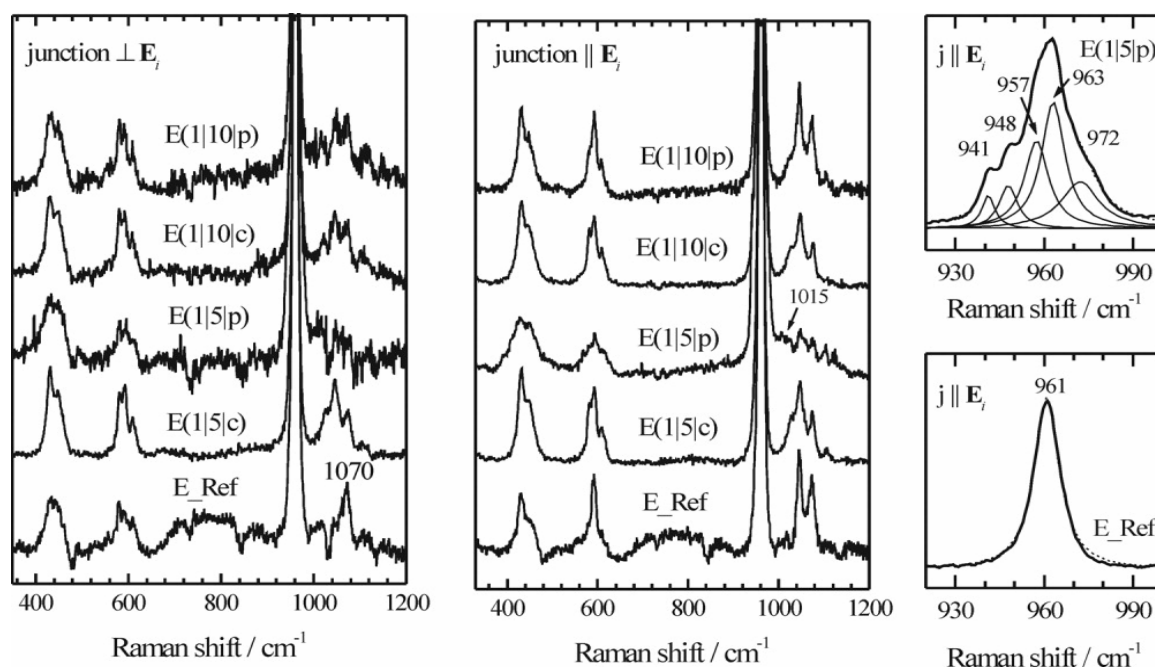


Fig. 25. Raman scattering of E(1|5|p), E(1|5|c), E(1|10|p), and E(1|10|c) collected from the centre of the CO_2 -laser spot; E_i denotes the polarization of the incident light, j stands for junction. The reference Raman spectra collected from areas far away from the CO_2 -laser spot was identical for all the samples. The dashed lines in the right-hand plots correspond to the Lorentzian-fit resultant profiles.

The ATR IR spectra of the samples irradiated with 1 W show different content of molecular inclusions in the morphologically distinct zones (Fig. 27 and Fig. 28). A common feature for all samples E(1|t|m) is the occurrence of CO_3 - CO_2 exchange in the zones of granular

morphology, as revealed by the decrease of the IR absorption in the range $1400\text{-}1550\text{ cm}^{-1}$, related to CO_3 groups and the appearance of an additional peak at 2343 cm^{-1} , arising from CO_2 . For samples E(1|t|c), the $\text{CO}_3\text{-CO}_2$ exchange is accompanied by rearrangement of the carbonate groups in the apatite crystal structure. As the IR absorption at 1412 and 1547 cm^{-1} is associated with carbonate groups substituting for PO_4 (B-type CO_3) and OH (A-type CO_3) species, respectively [Markovic et al., 2004], the observed change in the relative intensities shows a decrease in the amount of B-type and an increase in the amount of A-type CO_3 groups.

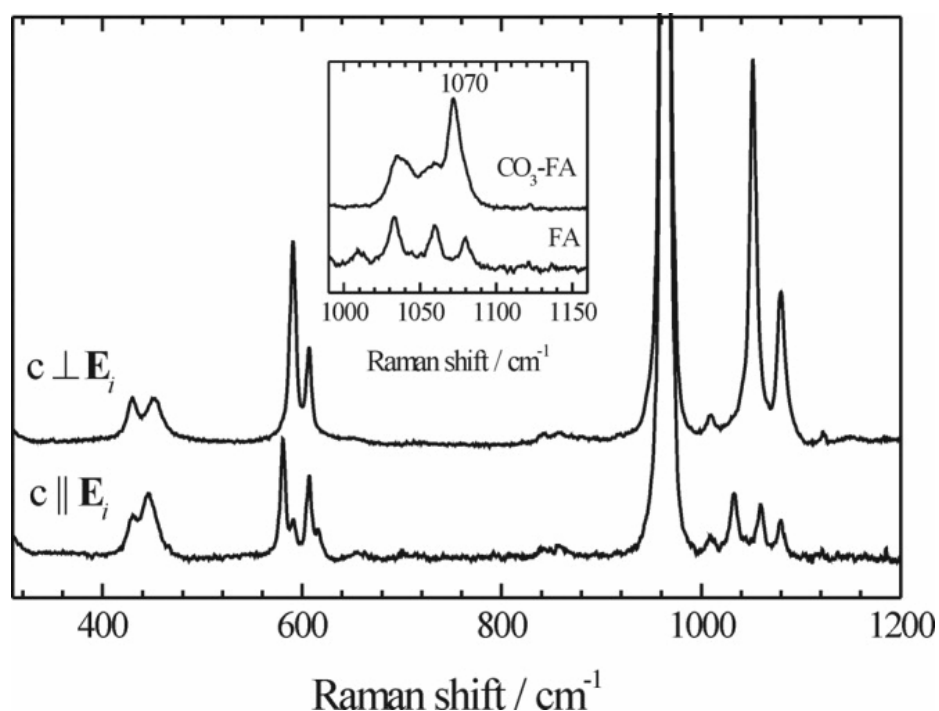


Fig. 26. Raman spectra of CO_3 -poor single crystal of fluorapatite measured in two different scattering geometries - when the c -axis is perpendicular and parallel to the polarization of the incident light E_i , which correspond to the Raman spectra of enamel apatite measured when the junction is parallel and perpendicular to E_i , respectively. The insert displays the Raman spectra of CO_3 -poor fluorapatite (FA) and CO_3 -rich fluorapatite ($\text{CO}_3\text{-FA}$), demonstrating that the peak at 1070 cm^{-1} arises from carbonate groups.

The Raman and IR spectra measured in the morphologically distinguishable zones of E(3|5|c) are presented in Fig. 29 and Fig. 30, respectively. The spectra clearly reveal different degrees of structural alteration depending on the distance from the centre of the laser crater.

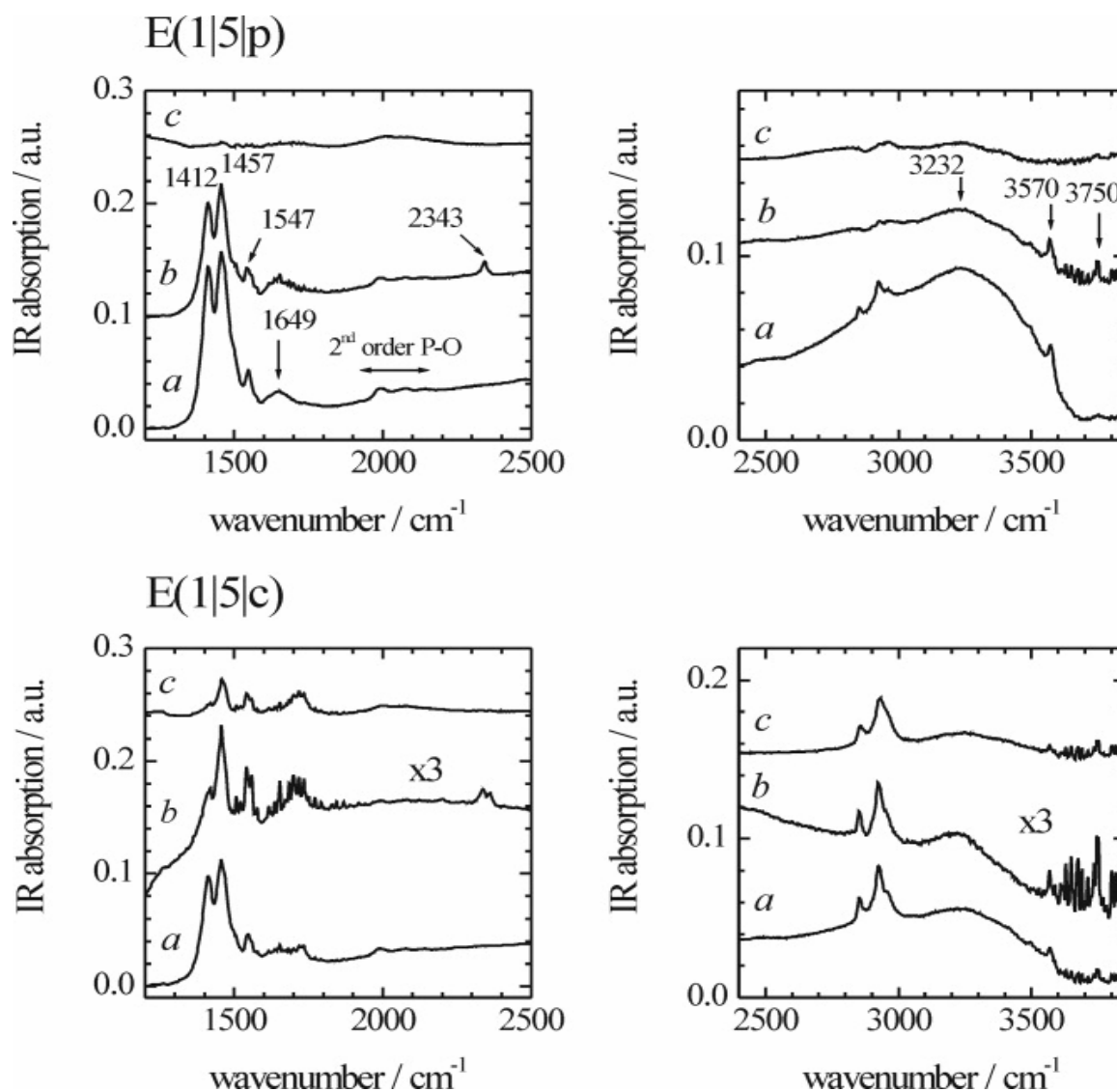


Fig. 27. Infrared absorption spectra of E(1|5|p) and E(1|5|c) collected outside (curves a), at the periphery (curves b) and inside (curves c) of the CO₂-laser spot; because of the high sensitivity of ATR IR spectroscopy to molecular inclusions, the reference spectra (curves a) were measured for each individual tooth.

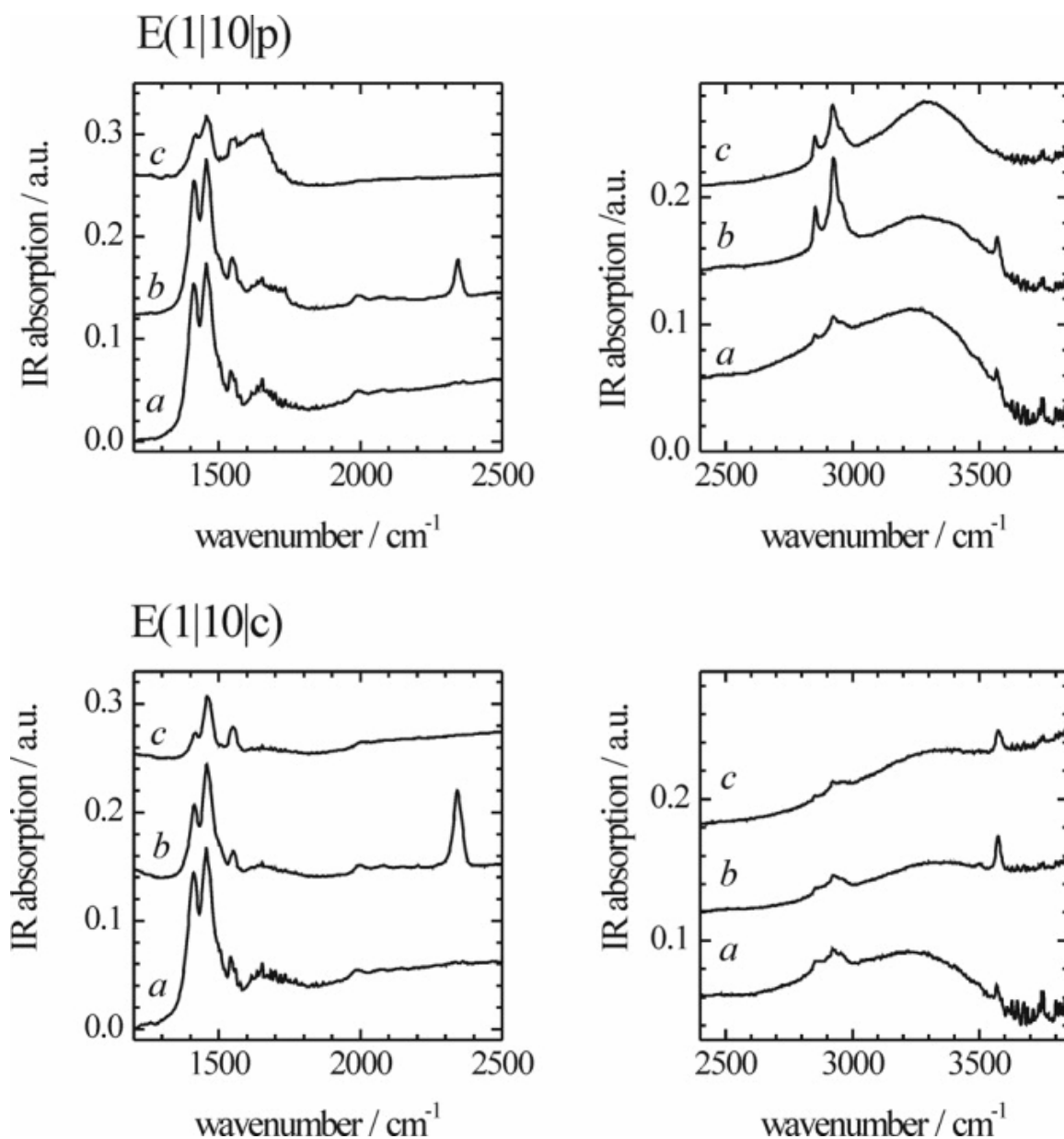


Fig. 28. Infrared absorption spectra of $E(1|10|p)$ and $E(1|10|c)$ collected outside (curves *a*), at the periphery (curves *b*) and inside (curves *c*) of the CO_2 -laser spot; because of the high sensitivity of ATR IR spectroscopy to molecular inclusions, the reference spectra (curves *a*) were measured for each individual tooth.

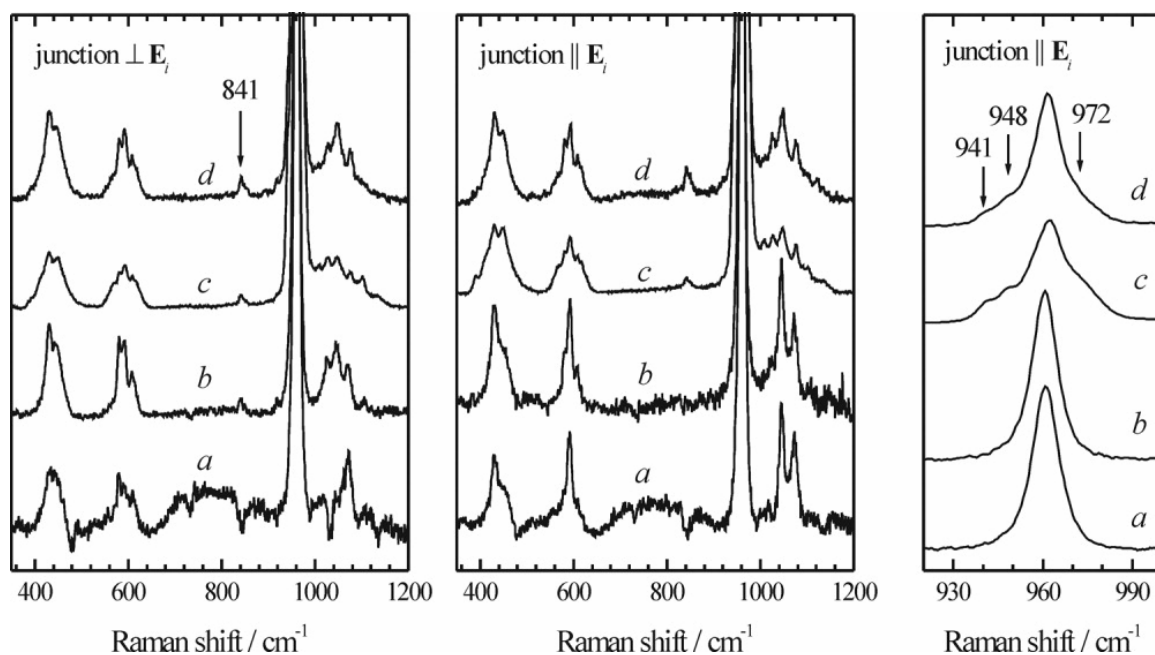


Fig. 29. Raman scattering of E(3|5|c) collected from untreated enamel (curves a); areas of granular morphology (curves b); areas of the wavy-like morphology (curves c); and the center of the laser crater (curves d); E_i denotes the polarization of the incident light. The corresponding Raman spectra of E(3|5|p) exhibit the same features as those of E(3|5|c).

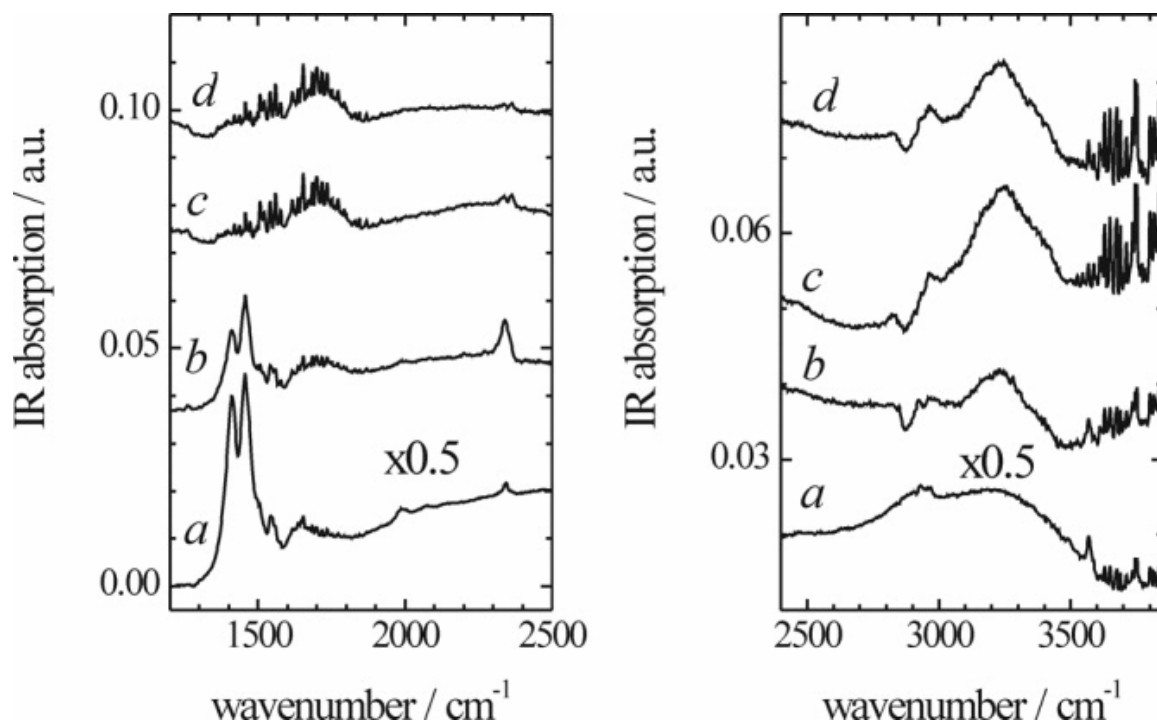


Fig. 30. Infrared absorption spectra of E(3|5|c) collected from untreated enamel distanced at about 300 μm far from the laser-crater rim (curves a); areas of granular morphology (curves b); areas of wavy-like morphology (curves c); and the centre of the laser crater (curves d).

4.4 Structural changes in bovine enamel

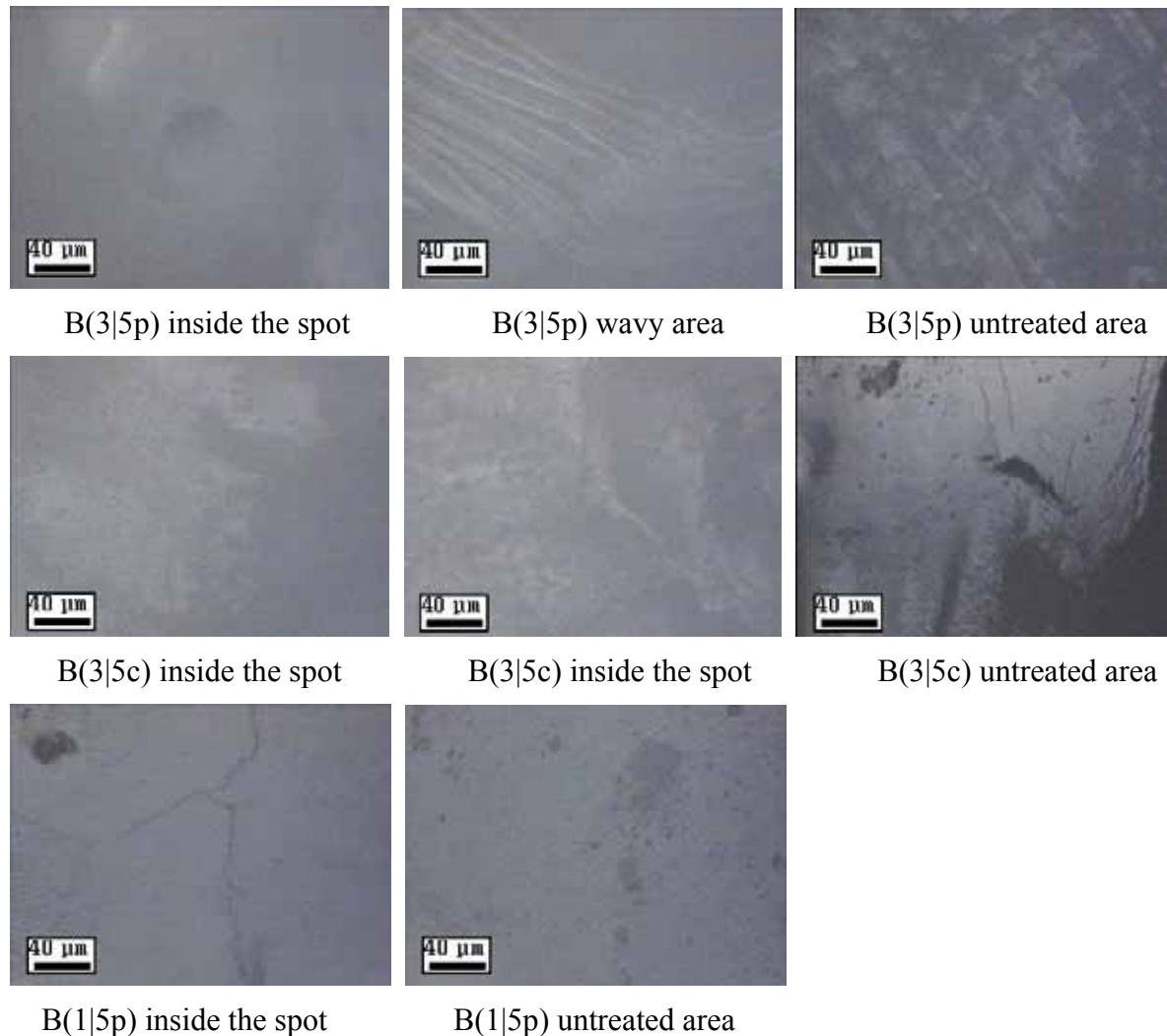


Fig. 31. Optical images of the laser spot on the bovine enamel surface; magnification $\times 500$. At 3 W and in super pulse mode, the lased spot has the same morphology as in human enamel. Some smaller craters can be seen. At 3 W and in continuous mode, no wavy area is found. When the power is as low as 1 W in super pulse mode, the lased surface remains almost unchanged. Only thin cracks and tiny droplets can be observed.

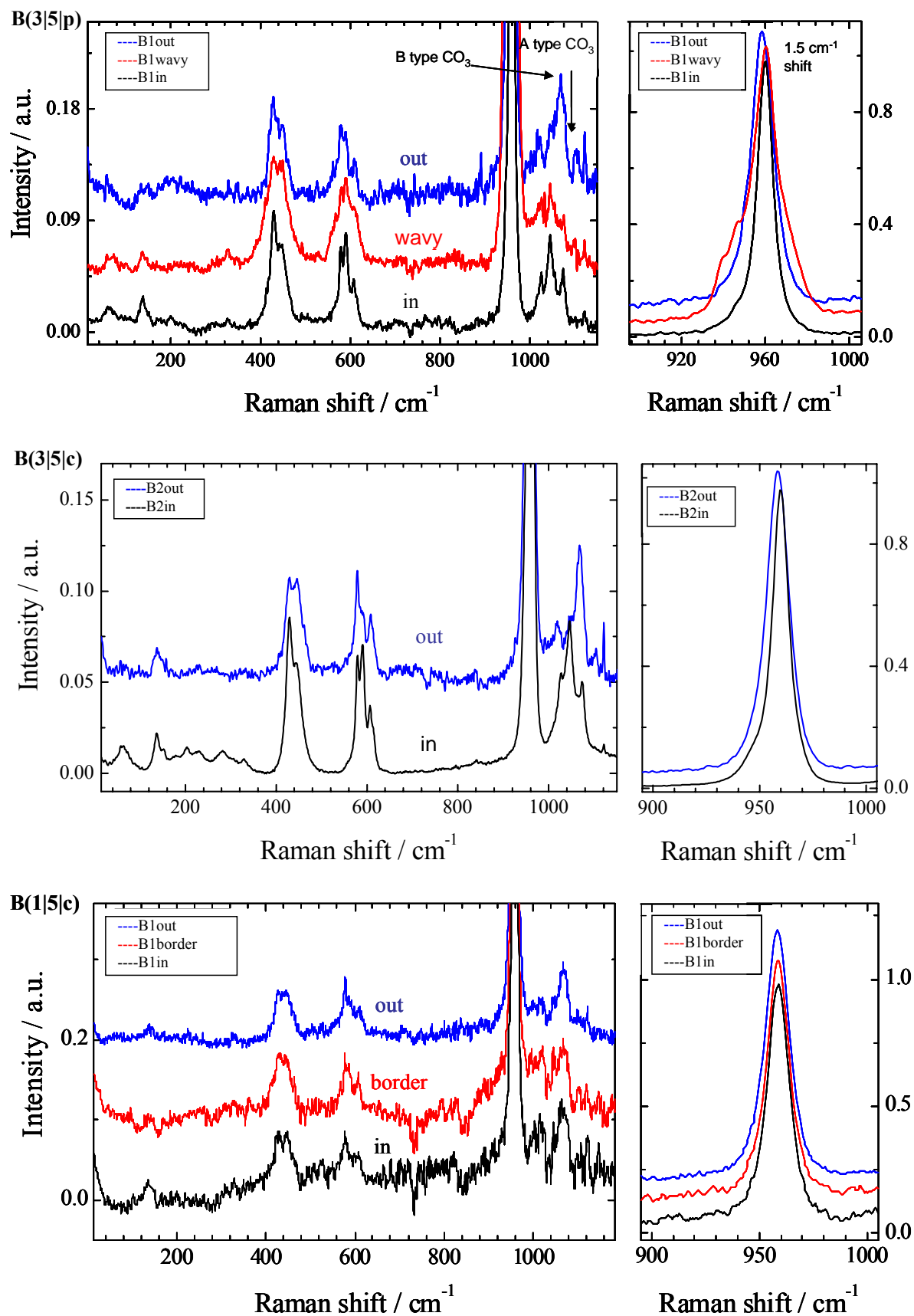


Fig. 32. Raman spectrum of bovine enamel irradiated under different conditions.

Out: outside of lased area; wavy: wavy area; in: inside lased area; border: border of lased area.

Bovine teeth and human teeth showed similar changes at 3W, 5s, both in super pulse and continuous wave laser mode. When the power was reduced to 1W, human teeth exhibited changes while bovine teeth showed no change except for cracks (Fig. 31). Raman spectrum shows that bovine enamel has a similar structural change as human enamel under 3W power, both under continuous wave and super pulse mode conditions. Peaks around 1071 and 1103 cm^{-1} should be B-type and A-type carbonate vibrations. The changes of their relative intensity ratio reveal the content change of these two types of carbonates [Timlin et al., 2000]. At 1W, unlike in human enamel, no structural change can be seen from the Raman spectra.

4.5 Powder X-ray diffraction

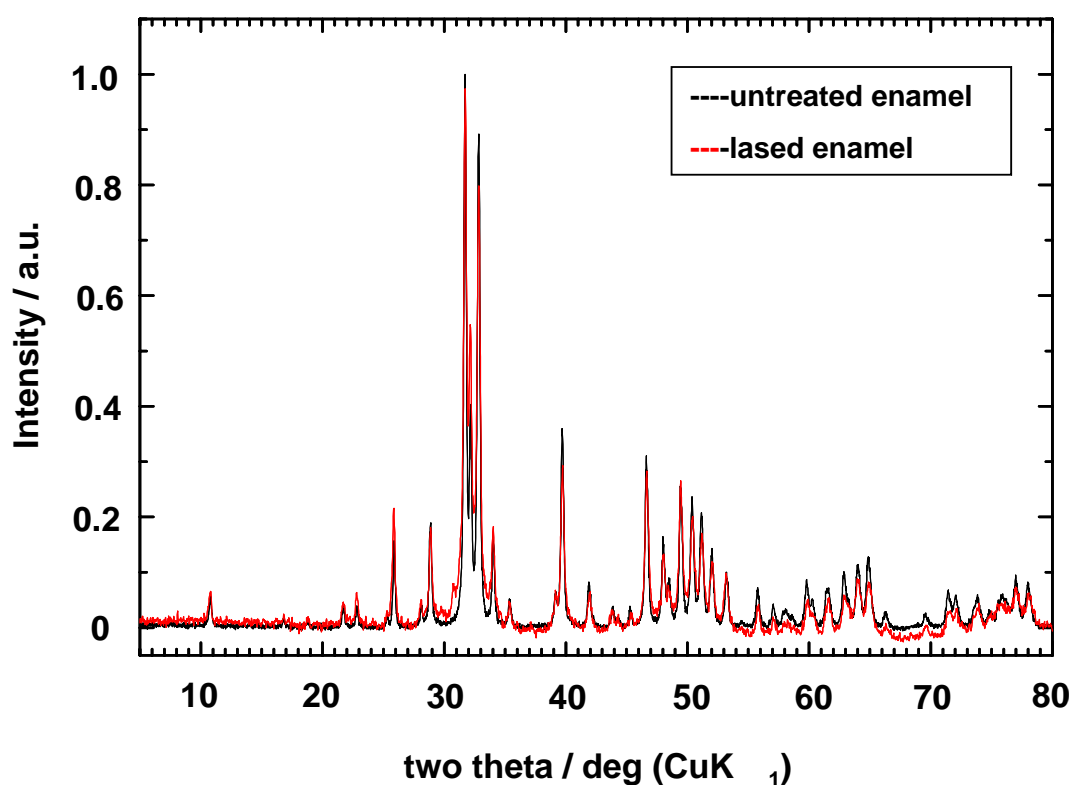


Fig. 33. XRD patterns of human enamel irradiated under the 3 W, 5 s and super pulse mode condition.

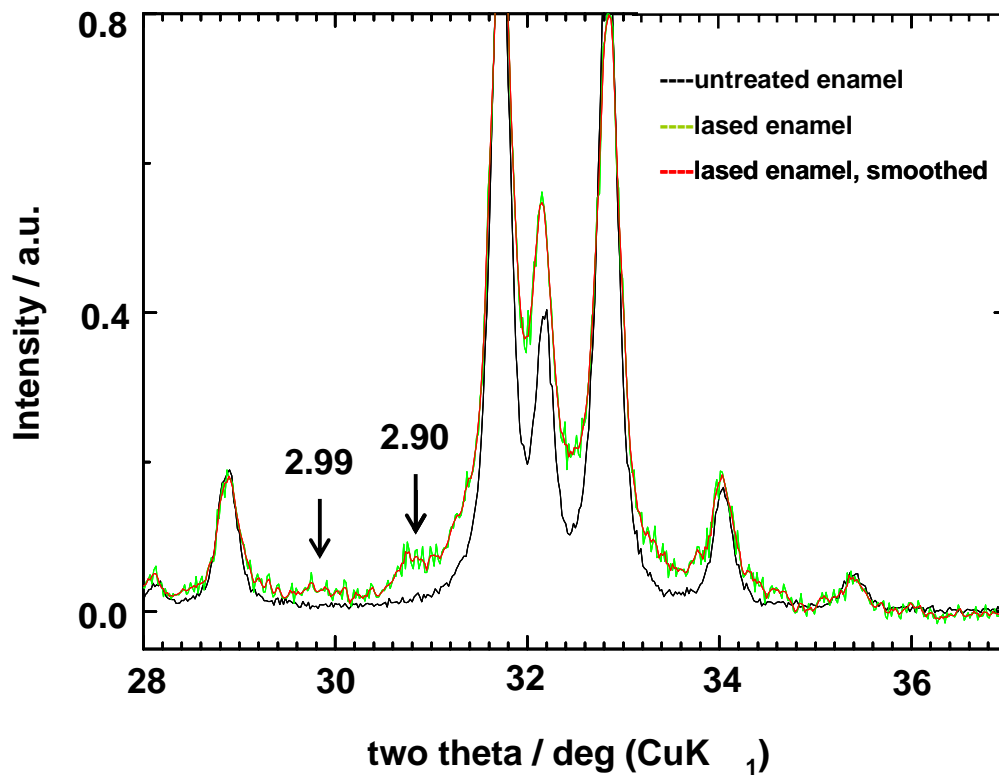


Fig. 34. XRD patterns of the human enamel irradiated under the 3 W, 5 s and super pulse mode condition. The as-measured XRD pattern is smoothed by the adjacent average method, 3 points (red line).

From the powder X-ray diffraction data, two peaks indicate a new phase in the enamel apatite (Figure 33 and 34). The calculated distance between two adjacent planes of two is 2.90 and 2.99 respectively. These values are close to that of β -TCP, 2.88 and 3.01. This suggests that β -TCP is formed [Koutsopoulos, 2002].

Chapter 5

Discussion: structural transformations in laser treated human dental enamel

5.1 Effects of low-power laser irradiation (1 W)

When relative low power laser was used, the morphological change of dental enamel is less than that used relative high power laser. The comparison between the Raman spectra of E(1|5|p) and E(1|5|c) reveals that the SP mode has a stronger effect on the crystal structure of enamel apatite (Fig. 25). The appearance of additional Raman scattering near 970 cm^{-1} and the broadening of the bending and antisymmetrical stretching modes of the phosphate groups for E(1|5|p) point to a partial vitrification of the enamel structure. At the same time, extra well-resolved Raman peaks, the positions of which do not correspond to any hydroxyapatite peak, are observed in the spectral range $900\text{-}1200\text{ cm}^{-1}$ dominated from the PO_4 symmetrical and antisymmetrical stretching modes. Therefore, under SP laser irradiation of 1 W for 5 s, dental enamel is partially vitrified and partially converted into other crystalline phases. The absence of pronounced IR absorption peaks originating from OH or H_2O in the spectra collected from the centre of the laser spot of E(1|5|p) (see Fig. 27, the corresponding curves c) evidences that these phases are anhydrous calcium phosphates. Further, the existence of two split components at 941 and 948 cm^{-1} in the Raman spectrum, arising from the symmetrical stretching of PO_4 , and additional scattering near 1015 cm^{-1} suggests that one of these phases may be β -TCP [de Aza et al., 1997]. Such structural transformations are not observed for E(1|5|c), which is in accord with the XRD data. The Raman spectrum exhibits neither additional signals near the major peak at 963 cm^{-1} nor peak broadening. We cut our samples along the longitude of tooth, which is parallel to the c-axis, so that we have the sample surface always parallel to c-axis of hydroxyapatite crystal. We applied our Raman measurement at two different sample orientations, e.g. one for the polarization direction of incident light parallel to enamel-dentin junction (\parallel a-axis) and one perpendicular to the enamel-dentin

junction (\perp a-axis). According to Tsuda and Arends, hydroxyapatite crystal is highly oriented. Raman scatter bands are solely depend on the c-axis, but invariant to the orientation of the a-axis or b-axis. In our study, the Raman scattering measured in the two different scattering geometries is the same, which confirm the conclusion of Tsuda and Arends [1994].

In Fig. 27 and Fig. 28, peaks in the range $1400\text{-}1550\text{ cm}^{-1}$ relate carbonate group. For all the E(1|t|m) samples, carbonate content decrease from outside of lased spot to inside the spot. At the periphery (curve b), peak 2343 cm^{-1} , indicates the CO_2 formation from carbonate. In the center of all samples, no CO_2 exit at all. At 5 s and SP mode, there is no carbonate at all. At longer time, 10 s, SP mode, carbonate appears again. This could be the carbonate substitution occurred again during the recrystallization process. The mechanism is unclear. The bands at 1412 cm^{-1} is associated with B-type carbonate (substitute for PO_4), while 1547 cm^{-1} is associated with A-type carbonate (substitute for OH). At the CW mode, the B-type carbonate decreases while A-type carbonate increase. All these change suggest a possible change from B-type to A-type carbonate, then CO_2 and all escape from enamel in the end. This exchange happens from outside to the inside of lased spot.

The presence of an IR absorption peak at 3570 cm^{-1} (Fig. 27), typical of apatite OH groups, points also to preservation of apatite crystalline structure for E(1|5|c). This apatite OH band is diminished in the spot center of sample E(1|5|p). The absorption peak at 1649 cm^{-1} is associated with amide I. It disappears in the center of sample E(1|5|p) as well. The organic component of dental enamel is removed by laser only at this condition [Shi. et al., 2005]. Therefore, like synthetic hydroxyapatite, dental enamel is altered more, when a super pulse rather than a continuous wave mode is used. Our results are consistent with the work of Featherstone and Fried, who pointed out that maximum heat at the surface and optimum substance ablation is produced if the laser pulse duration and the thermal relaxation time of the teeth are similar. The pulse duration in our study was $125\text{ }\mu\text{s}$, close to $90\text{ }\mu\text{s}$, which is the thermal relaxation of enamel for a CO_2 laser operating at a wavelength of $10.6\text{ }\mu\text{m}$, while the CW mode can be thought as having a "pulse-duration time" much longer than the thermal relaxation time. Hence, the interaction processes between the laser beam and the enamel

apatite, and consequently the local heating should be much more efficient for SP rather than for CW mode. Thus, when the same power and irradiation time are used one should expect stronger structural alteration in the irradiated area in SP than in CW mode. Fig. 20 shows more melting area in enamel irradiated by SP laser than by CW laser [Featherstone and Fried, 2001; Zuerlin et al., 1999; Nelson et al., 1987].

Interestingly, the Raman spectra of the samples irradiated with 1 W for a longer time (10 s) are orientation-dependent and do not reveal substantial deviation from the spectra of untreated enamel (Fig. 25). This observation is indicative of a recrystallization of apatite taking place when the irradiation time increases from 5 to 10 s. The surface looks the same or more smooth as irradiation time increased. This possible structure-recovering mechanism under prolonged low-power laser irradiation might explain the improved clinical properties of enamel after CO₂ laser irradiation; the CO₂-laser was suggested to be convenient for surface treatment of dental enamel and enhanced acid resistance has been reported [Hsu et al., 2000]. Structural recovery and recrystallization might be the basis for the uniformity of CO₂ laser-treated surfaces and for the purification of a beneficial, purer hydroxyapatite phase as observed by Fried and Breunig [2001]. For samples E(1|5|m), an intensification of the IR absorption peak at 3750 cm⁻¹ is observed for the zones of granular morphology, thus suggesting a reduction of the grain size. Such an increase in intensity of this peak is not characteristic for samples E(1|10|m), which supports the assumption of an occurrence of structure recovery under prolonged low-power irradiation time. Considering the IR absorption of samples E(1|10|m), one can also see that the content of physical absorbed water in the central zones of the laser spot is much higher for the sample treated in SP mode compared with that in the CW mode. This is an indirect evidence of a higher degree of crazing or porous when SP mode is used. From Fig. 19 and Fig. 20, visible crack can be seen in CW mode, both 5 s and 10 s. This suggests there are must be much bigger spaces in the enamel irradiated by pulsed laser than by CW laser. These micro-space or porous can trap water from environment. In clinic, this might be a possible mechanism of reminerallization or self caries repair: more calcium, phosphate and fluoride ion will be uptaken into enamel which enhance the reminerallization of enamel and results caries prevention [Oho and Morioka, 1990].

5.2 Effect of high-power laser irradiation (3 W)

The Raman spectra of dental enamel irradiated with 3 W shows that, in the peripheral zone of granular morphology, the crystallinity and the preferred orientation of the apatite crystallites are preserved (Fig. 29, curves b). The ATR IR spectra indicate that, similar to the samples treated at 1 W, a decomposition of CO_3 groups and formation of CO_2 occur in this zone (Fig. 30, curves b). Such molecular exchange, but to a lesser degree, was detected also in spatial regions distanced at $\sim 300 \mu\text{m}$ far from the rim of the laser crater, which appear unchanged in the optical image. Therefore, laser irradiation can cause a temperature increase and thus mobilization of molecular inclusions even in areas with preserved morphology. According to the Raman data, the zone of wavy morphology at the slope of the laser crater is characterized by decomposition of apatite and co-formation of amorphous substance and additional crystalline phases (Fig. 29, curves c). Since the IR absorption shows no presence of “apatite” OH groups (peak at 3570 cm^{-1}), these crystalline phases should be anhydrous calcium phosphates, like the central zone of E(1|5|p).

The Raman scattering measured in the central zone of the laser crater reveals occurrence of devitrification (suppression of the signal near 970 cm^{-1} and the peak broadening) and a reduction of additional anhydrous crystalline phases (suppression of the peaks near 941 and 948 cm^{-1}). The Raman spectra collected in the two scattering geometries are identical and resemble most the spectrum of synthetic hydroxyapatite. However, the absence of the IR absorption peak at 3570 cm^{-1} indicates that the dominant phase in the centre of the laser crater is dehydrated apatite. Most probably the prevalent phase in the central zone is oxygenated apatite [Trombe & Montel, 1978] with abundance of incorporated O_2^{2-} ions. This assumption is based on the appearance of the additional Raman scattering at 841 cm^{-1} . The position of this peak is close to the bond stretching mode of O_2^{2-} as well as to the out-of-plane mode of embedded CO_3^{2-} [Giuere and Srinivasan, 1974; Nakamoto, 1997]. However, the ATR IR data give no evidence for the presence of carbonate groups, thus suggesting that the Raman peak at 841 cm^{-1} arises from O_2^{2-} species incorporated into irradiated enamel. Therefore, O_2^{2-} -bearing

apatite is the major structural component of the central zone of the laser crater. Under water-free conditions oxyapatite, which contains O^{2-} instead of OH^- , exists at temperatures between 1030 and 1230 K [Trombe and Montel, 1978]. Peroxyapatites, bearing O_2^{2-} ions, are formed at high temperatures from oxyapatites by reaction between O^{2-} ions and O_2 molecules in atmosphere sufficiently free of water. Rapid cooling favors the occurrence of O_2^{2-} ions on the account of O^{2-} [Trombe and Montel, 1978]. Thus, the formation of O_2^{2-} -bearing apatite at the bottom of the crater is not surprising, since the substance just below the ablated layers should experience high temperatures, water-free conditions, and a fast rate of cooling.

The ATR IR spectra from the central zone and from the zone of wavy morphology of E(3|5|p) were not able to be collected, because of the substantial roughness of the surface in those areas, which hindered good contact between the ATR crystal and the sample. However, the zone of granular morphology exhibits the same features for both E(3|5|p) and E(3|5|c). Also, the Raman spectra collected from all of the three morphologically distinct zones of E(3|5|p) exhibit the same peculiarities as the corresponding zones of E(3|5|c). Therefore, for higher laser power (3 W), the power itself is the primary factor rather than the laser operational mode for the induced structural modifications.

Kuroda and Fowler used a CW CO_2 laser (10.6 μm) to irradiate enamel 1 second under power of 20 W. The laser energy density was 10000 J/cm^2 . The crater formed at this condition is similar to our results under 3 watt power. They reported α -tricalcium phosphate ($\alpha-Ca_3(PO_4)_2$) and tetracalcium phosphate ($Ca_4(PO_4)_2O$) in melting enamel. Nelson and coworker found tetracalcium phosphate as well. The CO_2 (10.6 μm) laser pulse duration was 100 ns. Energy density was 50 J/cm^2 , e.g. 0.67 Hz for 400 pulses. Kwon and coworker worked on a laser used in Kuroda's study. The enamel surface was scanned at a speed of 7 cm/sec, 12 W. They concluded α -tricalcium phosphate formation and reduction of calcium loss after laser irradiation. In our study, the laser energy density is around 5000 J/cm^2 , but no α -tricalcium phosphate and tetracalcium phosphate are found [Kuroda and Fowler, 1984; Nelson et al., 1987; Kwon et al., 2005].

5.3 Comparison of laser and thermally treated enamel

Shi and coworker studied the structural and chemical modification of dental enamel apatite after heat treatment in air for 1 hour from 300 to 1193 K. Both IR and XRD results show a high degree of crystallinity of apatite that is enhanced with increasing temperature. The loss of B-type and A-type carbonate was studied; the amount of B-type carbonate and the total carbonate content decrease on heating while the amount of A-type carbonate first decreases up to 573 K and then increases from 573 to 973 K. Almost 50 % of the carbonate ions were released from dental enamel with the formation of β -tricalcium phosphate phase (β -TCP) after heat treatment at 973 K for 1 h. The incorporation of CO_2 and cyanate species in dental enamel was observed in the temperature range of 273–973 K and 673–1073 K, respectively. The content of CO_2 in dental enamel increases from 473 K to a maximum near 773 K and decreases thereafter [Shi et al., 2005].

Fowler and Kuroda gave a good review on changes in heat and in laser-irradiated human tooth enamel. Since the laser-induced changes are expected to primarily arise from localized heating, previously reported thermally induced changes in tooth enamel on heating in conventional furnaces were utilized to infer corollary changes along the gradient in laser-irradiated tooth enamel. These thermally inferred changes which resulted in modifications in the tooth enamel apatite and/or newly formed phases were correlated with their probable effects on altering solubility. A temperature gradient range from 100-1600°C was considered with subdivisions as follows: I, 100-650°C II, 650-1100°C and III, >1100°C Two of the products formed in range III, α - $\text{Ca}_3(\text{PO}_4)_2$ and $\text{Ca}_4(\text{PO}_4)_2\text{O}$, and also identified in the fused-melted material from laser-irradiated tooth enamel, are expected to markedly increase solubility in those regions that contain considerable amounts of these compounds. Products and changes occurring in range II, separate phases of α - and/or β - $\text{Ca}_3(\text{PO}_4)_2$ and a modified phase of apatite, may increase or decrease the solubility depending on the Ca/P ratio and the resultant amounts of α -, β - $\text{Ca}_3(\text{PO}_4)_2$ formed. Modifications in tooth enamel apatite effected in range I are expected to decrease its solubility; the formation of pyrophosphate in this range may have a substantial effect on reducing the solubility rate. It appears that

laser-irradiant conditions that produce localized temperatures above about 650°C may have a deleterious effect on tooth enamel solubility unless calcium is introduced to increase the Ca/P ratio to near that of hydroxyapatite (Table 21) [Fowler & Kuroda, 1986].

Palamara and coworker examined the effect on the ultrastructure of dental enamel of excimer-dye, argon-ion and CO₂ laser. In their study, the CW CO₂ laser produced shallow craters, surface crazing and lifting off and removal of the surface layer to expose the underlying roughened enamel. The ultrastructure revealed inter- and intra-crystalline porosity, a mixture of small but variable size irregularly packed large crystallized enamel crystals and also well packed large crystal which indicated further grain growth. The porosity in lased enamel was overall very similar to that seen in enamel heated in an electric furnace to a temperature of 600 °C. The presence of recrystallized enamel crystals indicated a temperature rise of ~1000°C and the grain growth indicated that a temperature $\geq 1000^\circ\text{C}$ existed for some time after laser irradiation. It is known that the recrystallization temperature for metal and alloys varies from 0.3 to 0.7 of the absolute melting temperature. The variation depends upon several factors including the amount of prior cold work and the purity of the metal or alloy. For a ceramic type material such as dental enamel, the recrystallization temperature would lie at the higher end of the range namely 0.7 of the absolute melting point for enamel (1280°C). Hence the temperature reached in enamel where recrystallization was observed would be approximately 1000°C. In the absence of cold work in enamel crystals, the recrystallization can result from the surface poisoning of the grains by impurities, organic material and CO₂ released from non stoichiometric hydroxyapatite. Moreover the vapor and the gases released at high temperature may exert extreme pressures at elevated temperatures causing deformation in the original enamel crystals. Such deformation would promote recrystallization [Palamara et al., 1992].

In our study, comparison between the structural changes in heated and irradiated enamel shows that under laser treatment the achieved average temperature at the bottom and near the CO₂-laser crater was about 1100 and 700 K, respectively. Our data are in good agreement with the results of Zuerlein et al. who found that carbonate loss was initiated at 670 K, but

complete carbonate loss did not occur until melting is achieved at temperatures greater than 1070 K. [Zuerlein et al. 1999] CO_2 formed at the periphery where the temperature is medium, with the appearance of enamel unchanged. The transformation of B-type carbonate to A-type carbonate only occurred clearly in CW mode. This is agreed with Shi's work. The β -TCP and recrystallization can be seen in our work as well.

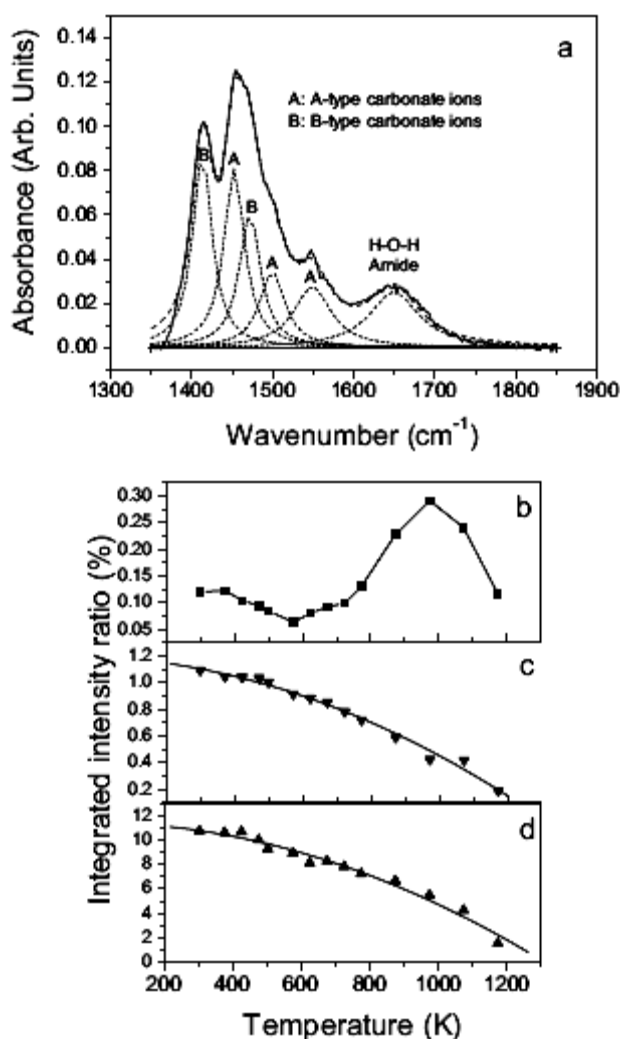


Fig. 35. (a) Deconvolution of the IR absorbance spectrum of dental enamel apatite between 1350 and 1850 cm^{-1} using six bands of Lorentzian profile. Integrated intensity ratios of A-type carbonate ions to phosphate ions (b), B-type carbonate ions to phosphate ions (c), and total carbonate ions to phosphate ions (d) as a function of temperature (from 300 to 1173 K) [Shi et al., 2005]

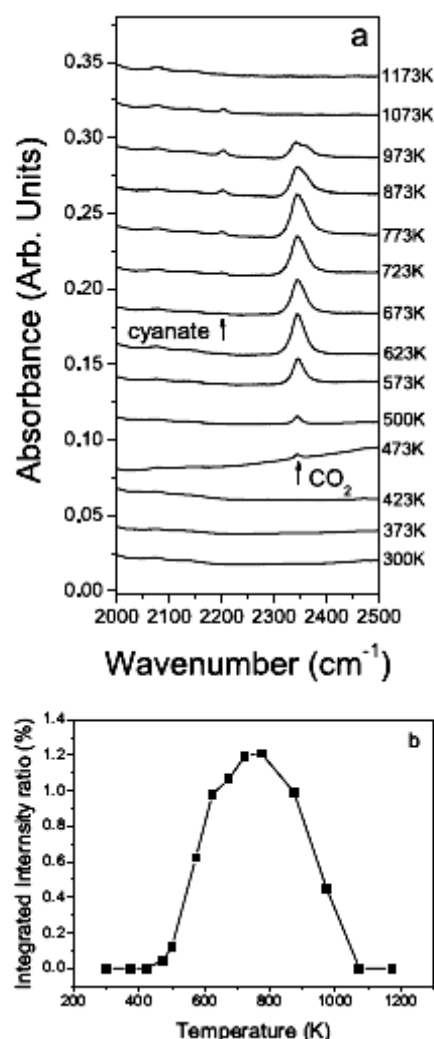


Fig. 36. (a) Infrared spectra of dental enamel between 2000 and 2500 cm^{-1} as a function of temperature. The absorbance bands of cyanate ions and CO_2 near 2200 cm^{-1} and 2344 cm^{-1} respectively, indicate the incorporation of the two species into dental enamel. (b) Integrated intensity ratio of CO_2 to phosphate groups as a function of temperature [Shi et al., 2005].

Table 21. Physical and chemical changes that occur during the heating of tooth enamel.

Temperature (°C)	Physical and chemical changes
100-650	Loss of H ₂ O (~30% of total H ₂ O content) Carbonate loss (~66% of total CO ₂ content) and rearrangement to phosphate and hydroxy ion positions Pyrolysis of organics
650-1,100	Sintering and recrystallization Formation of β-TCP Loss of remaining water and carbonate
1280	Melting of hydroxyapatite
1450	Hydroxyapatite disproportionates to α-TCP and Ca ₄ (PO ₄) ₂ O
1600	α-TCP and Ca ₄ (PO ₄) ₂ O melt

Chapter 6

Conclusion and potential application

6.1 Conclusion

While the laser power is the primary factor determining the effect of laser irradiation on enamel apatite, in particular for lower power of irradiation the operational mode considerably influences the type and the degree of morphological and structural changes. By tuning the treatment time of the low-power irradiation one can minimize the structural damage in irradiated enamel.

A relatively high power of laser irradiation (3 W), regardless of the operational mode, leads to a formation of a crater with three clearly distinguishable zones from the centre to the periphery: (i) a bottom zone, the structure of which consists of dehydrated O_2^{2-} -bearing apatite as a major component and traces of additional anhydrous calcium phosphate phases; (ii) a wavy-like zone at the inner slope of the crater, which is abundant with anhydrous calcium phosphate crystalline and amorphous phases and (iii) a granular-like zone on the outer side of the crater rim, which is characterized by CO_3-CO_2 exchange, preserving the crystalline structure of hydroxyapatite.

The operational mode is of major significance for the degree of structural damage, if a relatively low power (1 W) is used; the super pulse laser irradiation with pulse duration of 125 μs for a 10.6 μm wavelength CO_2 laser has a stronger impact on the biological hydroxyapatite structure than the continuous wave mode. By tuning the treatment time of the low-power irradiation, one can minimize the structural damage in irradiated enamel. The structure-recovery phenomenon occurring upon prolonged laser irradiation might present the basis for laser treatment applications aimed at enhancing surface enamel characteristics such as acid resistance.

6.2 Potential application of this study

The CO₂ laser result melting and lift off of surface enamel when relative high power is used. Since it usually causes crack and leaves more heat residue on the tooth, its application of ablation is limited. This kind of ablation effect gives this CO₂ laser the potential application for shallow caries removing.

When relative low power was used in this study, a recrystallization of apatite occurred when the irradiation time increases from 5 to 10 s. The surface looks the same or more smooth as irradiation time increased. This possible structure-recovering mechanism under prolonged low-power laser irradiation might explain the improved clinical properties of enamel after CO₂ laser irradiation; Decomposition of CO₃ groups occurred at both high and low power condition. Less CO₃ content means purer hydroxyapatite which is less soluble than carbonated apatite. More micro-spaces were found even in the area without a morphological change. These micro-spaces can enhance the uptake of calcium, fluorine and other ion for enamel remineralization. All these results suggest that the low power CO₂ laser is suit for improving enamel acid resistance, e.g. caries prevention.

References

Akova, T., Yoldas, O., Serdar Toroglu, M. and Uysald, H. Porcelain surface treatment by laser for bracket-porcelain bonding. *American Journal of Orthodontics and Dentofacial Orthopedics*. Vol. 128, No. 5, pp. 630-637, 2005.

Alexander, R., Xie, J. and Fried, D. Selective removal of residual composite from dental enamel surfaces using the third harmonic of a Q-Switched Nd:YAG laser. *Lasers in Surgery and Medicine*. Vol. 30, pp. 240-245, 2002.

Als-Nielsen, J. and Des McMorrow, D. *Elements of modern X-ray physics (Modern x-ray physics & new developments)*. Publisher: John Wiley & Sons Ltd., New York, 2001.

Aminzadeh, A., Shahabi, S. and Walsh, L. J. Raman spectroscopic studies of CO₂ laser-irradiated human dental enamel. *Spectrochimica Acta part A*. Vol. 55, pp. 1303-1308, 1999.

Anderson, A. M., Kao, E., Gladwin, M., Benli, O. and Ngan, P. The effects of argon laser irradiation on enamel decalcification: An in vivo study. *American Journal of Oorthodontics and Dentofacial Orthopedics*. Vol. 122, No. 3, pp. 251-259, 2002.

Anderson, J. R., Ellis, R. W., Blankenau, R. J., Beiraghi, H. M. and Westerman, G. H. Caries resistance in enamel by laser irradiation and topical fluoride treatment. *Journal of Clinical Laser Medicine & Surgery*. Vol. 18, No. 1, pp. 33-36, 2000.

Anderson, P., Elliott, J. C., Bose, U. and Jones, S. J. A comparison of the mineral content of enamel and dentine in human premolars and enamel pearls measured by X-ray microtomography. *Archives of Oral Biology*. Vol. 41, No.3, pp. 281-290, 1996.

Antunes, A., de Rossi, W. and Zezell, D. M. Spectroscopic alterations on enamel and dentin after nanosecond Nd:YAG laser irradiation. *Spectrochimica Acta part A*. Vol. 64, pp. 1142-1146, 2006.

Apel, C., Birker, L., Meister, J., Weiss, C. and Gutknecht, N. The caries-preventive potential of subablative Er:YAG and Er:YSGG laser radiation in an intraoral model: a pilot study. *Photomedicine and Laser Surgery*. Vol. 22, No. 4, pp. 312-317, 2004.

Apel, C., Franzen, R., Meister, J., Sarrafzadegan, H., Thelen, S. and Gutknecht, N. Influence of the pulse duration of an Er:YAG laser system on the ablation threshold of dental enamel. *Lasers in Medical Science*. Vol. 17, pp. 253-257, 2002.

Apel, C., Meister, J., Götz, H., Duschner, H. and Gutknecht, N. Structural changes in human dental enamel after subablative Erbium laser irradiation and its potential use for caries prevention. *Caries Research*. Vol. 39, pp. 65-70, 2005.

Arcoria, C. J. Laser tissue interactions. Baylor college of dentistry, Texas A&M University System Health Science Center. <http://www.tamcd.edu/cedental/lasetiss.htm>, 2005.

Arcoria, C. J. basic concepts of lasers and laser systems. A course materials for continuing education, Texas A&M University System Health Science Center, 2005.

Attrill, D.C., Farrar, S.R., King, T.A., Dickinson, M.R., Davies, R.M. and Blinkhorn, A.S. Er:YAG ($\lambda=2.94 \mu\text{m}$) laser etching of dental enamel as an alternative to acid etching. *Lasers in Medical Science*. Vol. 15, pp. 154-161, 2000.

de Aza, P. N., Santos, C., Pazo, A., de Aza, S., Cusco, R. and Artus, L. Vibrational properties of calcium phosphate compounds. 1. Raman spectrum of β -tricalcium phosphate. *Chemical Materials*. Vol. 9, pp. 912-915, 1997.

de Aza, P. N., Santos, C., Pazo, A., de Aza, S., Cusco, R. and Artus, L. Vibrational properties of calcium phosphate compounds. 2. Comparison between hydroxyapatite and β -tricalcium phosphate. *Chemical Materials*. Vol. 9, pp. 912-915, 1997.

Azzeh, E. and Feldon, P. J. Laser debonding of ceramic brackets: A comprehensive review. *American Journal of Orthodontics and Dentofacial Orthopedics*. Vol. 123, No. 1, pp. 79-83, 2003.

Balmain, J., Hannover, B. and Lopez, E. Fourier transform infrared spectroscopy (FTIR) and X-ray diffraction analyses of mineral and organic matrix during heating of mother of pearl (nacre) from the shell of the mollusc *Pinctada maxima*. *Journal of Biomedical Materials Research: Applied Biomaterials*. Vol 48, Issue 5, pp. 749 – 754, 1999.

Barbour, M. E. and Rees, J. S. The laboratory assessment of enamel erosion: a review. *Journal of Dentistry*. Vol. 32, pp. 591–602, 2004.

Baumer, A., Ganteaumer, M. and Klee, W. E. Determination of OH ions in FHAP by infrared spectroscopy. *Bulletin de Mineralogy*. Vol. 108, pp. 145-152, 1985.

Bish, D. L. and Post, J. E., editors. Modern powder diffraction. *Reviews in Mineralogy*, Mineralogical Society of America, Vol. 20, 1989.

Calderin, L. and Stott, M. J. Electronic and crystallographic structure of apatites. *Physical Review*. B 67, 134106, 2003.

- Corpas-Pastor, L., Moreno, J. V., Garrido, J. D. D. L., Muriel, V. P., Moore, K. and Elias, A. Comparing the tensile strength of brackets adhered to laser-etched enamel vs. acid-etched enamel. *Journal of American Dental Association*. Vol. 128, pp 732-737, 1997.
- Courrol, L. C., Zezell, D. M., Samad, R. E., Gomes, L. and Vieira, N. D. Jr. Spectroscopic characterization of sound and carious ablated dental tissue after Er:YAG laser interaction. *The Journal of Applied Research in Clinical Dentistry*. Vol. 1, No. 1, pp. 29-34, 2004.
- Dahm, S. and Risnes, S. A comparative infrared spectroscopic study of hydroxide and carbonate absorption bands in spectra of shark enameloid, shark dentin, and a geological apatite. *Calcified Tissue International*. Vol. 65, pp. 459-465, 1999.
- Delbem, A. C. B., Cury, J. A., Nakassime, C. K., Gouveia, V. G. and Theodoro, L. H. Effect of Er:YAG laser on CaF₂ formation and its anti-cariogenic action on human enamel: an in vitro study. *Journal of Clinical Laser Medicine & Surgery*. Vol. 21, No. 4, pp. 197-201, 2003.
- Devarajan, V. and Klee, W. E. A potential model for fluorapatite. *Physics and Chemistry of Minerals*. Vol. 7, pp. 35-42, 1981.
- Dias, A. G., Skakle, J. M. S., Gibson, I. R., Lopes, M. A. and Santos, J. D. In situ thermal and structural characterization of bioactive calcium phosphate glass ceramics containing TiO₂ and MgO oxides: High temperature – XRD studies. *Journal of Non-crystalline Solids*. Vol. 351, pp. 810–817, 2005.
- Donadel, K., Laranjeira, M. C. M., Goncalves, V. L. and Favere, V. T. Structural, vibrational and mechanical studies of hydroxyapatite produced by wet-chemical methods. Cornell University, New York. <http://arxiv.org/abs/physics/040>, 2002.
- Duplain, G., Boulay, R. and Belanger, P. A. Complex index of refraction of dental enamel at CO₂ laser wavelengths. *Applied Optics*. Vol. 26, No. 20, pp. 4447-4451, 1987.
- El Feki, H., Rey, C. and Vignoles, M. Carbonate ions in apatites: infrared investigations in the ν₄ CO₃ domain. *Calcified Tissue International*. Vol. 49, pp. 267-274, 1991.
- Ellies, L. G., Nelson, D. G. A. and Featherstone, J. D. B. Crystallographic structure and surface morphology of sintered carbonated apatites. *Journal of Biomedical Materials Research*. Vol. 22, pp. 541-553, 1988.
- Elliott, J. C. Structure, crystal chemistry and density of enamel apatite. *Dental enamel*. CIBA Foundation Symposium 205, pp. 54-72, 1997.
- Elliott, J. C., Holcomb, D. W. and Young, R. A. Infrared determination of the degree of substitution of hydroxyl by carbonate ions in human dental enamel. *Calcified Tissue International*. Vol. 37, pp. 372-75, 1985.

- Featherstone, J. D. B. Caries detection and prevention with laser energy. *Dental Clinics of North America*. Vol. 44, No. 4, pp. 955-969, 2000.
- Featherstone, J. D. B. The Caries Balance: Contributing Factors and Early Detection. *Journal of the California Dental Association*. Vol. 31, No. 2, pp. 129-133, 2003.
- Featherstone, J. D. B. The science and practice of caries prevention. *The Journal of American Dental Association*. Vol. 131, pp. 887-899, 2000.
- Featherstone, J.D.B., Barrett-Vespone N.A., Fried D., Kantorowitz Z., and Seka W. CO₂ laser inhibition of artificial caries-like lesion progression in dental enamel. *Journal of Dental Research*. Vol. 77, No. 6, pp. 1397-1403, 1998.
- Featherstone, J. D. B. and Fried, D. Fundamental interaction of lasers with dental hard tissues. *Medical Laser Application*. Vol. 16, pp. 181-194, 2001.
- Featherstone, J. D. B., Pearson, S. and LeGeros, R. Z. An infrared method for quantification of carbonate in carbonated apatites. *Caries Research*. Vol. 18, pp. 63-66, 1984.
- Ferreira, J. M., Palamara, P., Phakey, P. P., Rachinger, W. A. and Orams, H. J. Effects of continuous-wave CO₂ laser on the ultrastructure of human dental enamel. *Archives of oral biology*. Vol. 34, No. 7, pp. 551-562, 1989.
- Flaitz, C. M., Hicks, M. J., Westerman, G. H., Berg, J. H., Blankenau, R. J. and Powell, L. Argon laser irradiation and acidulated phosphate fluoride treatment in caries-like lesion formation in enamel: an in vitro study. *American Academy of Pediatric Dentistry*. Vol. 17, No. 1, pp. 31-35, 1995.
- Fowler, B. O. Infrared studies of apatites. I. Vibrational assignments for Calcium, Strontium, and Barium hydroxyapatites utilizing isotopic substitution. *Inorganic chemistry*. Vol. 13, No. 1, pp. 194-207, 1974.
- Fowler, B. O. Infrared studies of apatites. II. Preparation of normal and isotopically substituted Calcium, Strontium, and Barium Hydroxyapatites and spectra structure-composition Correlations. *Inorganic Chemistry*. Vol. 13, No. 1, pp. 207-214, 1974.
- Fowler, B. O. and Kuroda, S. Changes in hearted and in laser irradiated human tooth enamel and their probable effect on solubility. *Calcified Tissue International*. Vol. 38, pp. 197-208, 1986.
- Fox, J.L., Yu, D., Otsuka, M., Higuchi, W. I., Wong, J. and Powell, G. L. Initial dissolution rate studies on dental enamel after CO₂ laser irradiation. *Journal of Dental Research*. pp. 1389-1398, 1992.

Fraunhofer, J. A., Allen, D. J. and Orbell, G. M. Laser etching of enamel for direct bonding. *The Angle Orthodontist*. Vol. 63, No. 1, pp. 73-76, 1993.

Frentzen, M., Winkelsträter, C., Benthem, H. and Koort, H. The effects of pulsed ultraviolet and infrared lasers on dental enamel. *The European Journal of Prosthodontics and Restorative Dentistry*. Vol. 4, No. 3, pp. 99-104, 1996.

Fried, D. and Breunig, T. Hard tissue ablation and modification with IR lasers. <http://www-als.lbl.gov/als/compendium/AbstractManager/uploads/01049.pdf>, 2005

Fried, D. and Breunig, T. Infrared spectroscopy of laser irradiated dental hard tissues using the advanced light source. *Proceedings of SPIE*. Vol. 4249, Lasers in Dentistry VII, pp. 99-103, 2001.

Fried, D., Glana, R. E., Featherstone, J. D. B. and Seka, W. Permanent and transient changes in the reflectance of CO₂ laser-irradiated dental hard tissues at $\lambda = 9.3, 9.6, 10.3, \text{ and } 10.6 \mu\text{m}$ and at Fluences of 1–20 J/cm². *Lasers in Surgery and Medicine*. Vol. 20, pp. 22–31, 1997.

Fried, D., Ragadio, J. and Champion, A. Residual heat deposition in dental enamel during IR laser ablation at 2.79, 2.94, 9.6, and 10.6 μm . *Lasers in Surgery and Medicine*. Vol. 29, pp. 221-229, 2001.

Fried, D., Visuri, S. R., Featherstone, J. D. B., Walsh, J. T., Seka, W., Glana, R.E. and McCormack, S. M. Infrared radiometry of dental enamel during Er:YAG and Er: YSGG laser irradiation. *Journal of Biomedical Optics*. Vol. 1, No. 4, pp. 455-465, 1996.

Fried, D., Wheeler, C. R. and Le, C. Q. IR spectromicroscopy of laser irradiated dental hard tissues. www-als.lbl.gov/als/compendium/AbstractManager/uploads/02011.PDF, 2002.

Fuhrmann, R., Gutknecht, N., Magunski, A., Lampert, F. and Diedrich, P. Conditioning of enamel with Nd:YAG and CO₂ dental laser systems and with phosphoric acid: an in-vitro comparison of the tensile bond strength and the morphology of the enamel surface. *Journal of Orofacial Orthopedics*. Vol. 62, No.5, pp. 375-386, 2001.

García, F., Arias, J. L., Mayor, B., Pou, J., Rehman, I., Knowles, J., Best, S., León, B., Pérez-Amor, M. and Bonfield, W. Effect of heat treatment on pulsed laser deposited amorphous Calcium Phosphate coatings. *Journal of Biomedical Materials Research*. Vol. 43, No. 1, pp. 69-76, 1998.

Gibson, I. R., Rehman, I., Best, S. M. and Bonfield, W. Characterization of the transformation from calcium-deficient apatite to β -tricalciumphosphate. *Journal of Materials Science: Materials in Medicine*. Vol. 12, pp. 799-804, 2000.

- Glimcher, M. J., Mechanic, G., Bonar, L. C. and Daniel E. J. The amino acid composition of the organic matrix of the organic matrix of decalcified fetal bovine dental enamel. *The Journal of Biological Chemistry*. Vol. 236, No. 12, pp. 3210-3213, 1961.
- Gómez-Morales, J., Torrent-Burgués, J., Boix, T., Fraile, B. and Rodríguez-Clemente, R. Precipitation of stoichiometric hydroxyapatite by a continuous method. *Crystal Research and Technology*. Vol. 36, Issue 1, pp. 15-26, 2001.
- Goodman B. D. and Kaufman H. W. Effects of an argon laser on the crystalline properties and rate of dissolution in acid of tooth enamel in the presence of sodium fluoride. *Journal of Dental Research*. Vol. 56, No. 10, pp. 1201-1207, 1977.
- Groth, E. B., Mercer, C. E. and Anderson, P. Microtomographic analysis of subsurface enamel and dentine following Er:YAG laser and acid etching. *The European Journal of Prosthodontics and Restorative Dentistry*. Vol. 9, No.2, pp. 73-79, 2001.
- Harayaki, M., Hayakawa, K., Fukui, T., Isshiki, Y. and Powell, L. G. The Nd:YAG lasers is useful in prevention of dental caries during orthodontic treatment. *The Bulletin of Tokyo Dental College*. Vol, 42, No. 2, pp. 79-86, 2001.
- Harris, D. M., White, J. M., Goodis, H., Arcoria, C. J., Simon, J., Carpenter, W. M., Fried, D., Burkart, J., Yessik, M. and Myers, T. Selective ablation of surface enamel caries with a pulsed Nd:YAG dental laser. *Lasers in Surgery and Medicine*. Vol. 30, pp. 342-350, 2002.
- Hess, J. A. Scanning electron microscopic study of laser-induced morphologic changes of a coated enamel surface. *Lasers in Surgery and Medicine*. Vol. 10, pp. 458-462, 1990.
- Hicks, M. J., Flaitz, C. M., Westerman, G., Blankenau, R. J., Powell, G. L. and Berg, J. H. Caries-like lesion initiation and progression around laser-cured sealants. *American Journal of Dentistry*. Vol. 6, No. 4, pp. 176-180, 1993.
- Hollas, J. M. *Modern spectroscopy*, 2nd edition. Publisher: John Wiley & Sons Ltd., Oxford, England, 1992
- Hsu, C. Y., Jordan, T. H., Dederich, D. N. and Wefel, J. S. Effects of low-energy CO₂ laser irradiation and the organic matrix on inhibition of enamel demineralization. *Journal of Dental Research*. Vol. 79, No. 9, pp. 1725-1730, 2000.
- Hsu, C. Y., Jordan, T. H., Dederich, D. N. and Wefel, J. S. Laser-matrix-fluoride effects on enamel demineralization. *Journal of Dental Research*. Vol. 80, No. 9, pp. 1797-1801, 2001.
- Huang, G-F., Lan, W-H., Guo, M-K. and Chiang, C-P. Synergistic effect of Nd:YAG laser combined with fluoride varnish on inhibition of caries formation in dental pits and fissures in vitro. *Journal of Formosa Medical Association*. Vol. 100, No. 3, pp.181-185, 2001.

- Jalil, L. A., Labella, R. and Pearson G. J. Surface topography of enamel and dentine from primary teeth following infra-red Nd-YAG laser irradiation: An in vitro study. *Lasers in Medical Science*. Vol. 12, pp. 61-67, 1997.
- Johnson, S. Pulsed laser deposition of hydroxyapatite thin films. A master of science thesis. Georgia institute of technology, Georgia, Atlanta, 2005.
- Jones, F. H. Teeth and bones: applications of surface science to dental materials and related biomaterials. *Surface Science Reports*. Vol. 42, pp. 75-205, 2001.
- Kantorowitz, Z., Featherstone, J. D. B. and Fried, D. Caries prevention by CO₂ laser treatment: dependency on the number of pulse used. *Journal of American Dental Association*. Vol. 129, pp. 585-591, 1998.
- Keller, U. and Hibst, R. Effects of Er:YAG laser in caries treatment: a clinical pilot study. *Lasers in Surgery and Medicine*. Vol. 20, pp. 32–38, 1997.
- Khosroshahi, M. E. and Ghasemi, A. B. Interaction studies of multimode pulsed HF laser with enamel tissue using photothermal deflection and spectroscopy. *Lasers in Medical Science*. Vol. 18, pp. 196–203, 2004.
- Kimura, Y., Takahashi-Sakai, K., Wilder-Smith, P., Krasieva, T. B., Liaw, H.-H. L. and Matsumoto, K. Morphological study of the effects of CO₂ laser emitted at 9.3 μm on human dentin. *Journal of Clinical Laser Medicine and Surgery*. Vol. 18, No 4, pp. 197–202, 2000.
- Kimura, Y., Wilder-Smith, P., Arrastia-Jitosho, A. M. A., Liaw, L. L., Matsumoto, K. and Berns, M. W. Effects of nanosecond pulsed Nd:YAG laser irradiation on dentin resistance to artificial caries-like lesions. *Lasers in Surgery and Medicine*. Vol. 20, pp. 15-21, 1997.
- Kinney, J. H., Haupt, D. I., Balooch, M., White, J. M., Bell, W. L., Marshall, S. J. and Marshall, G. W. Jr. The threshold effects of Nd and Ho:YAG laser-induced surface modification on demineralization of dentin surfaces. *Journal of Dental Research*. Vol. 75, No. 6, pp. 1388-1395, 1996.
- Klein A. L. L., Rodrigues L. K. A., Eduardo C. P., Nobre dos Santos M., Cury J. A. Caries inhibition around composite restorations by pulsed carbon dioxide laser application. *European Journal of Oral Sciences*. Vol. 113, pp. 239 – 244, 2005.
- Koutsopoulos, S. Synthesis and characterization of hydroxyapatite crystals: A review study on the analytical methods. *Journal of Biomedical Materials Research*. Vol. 62, No. 4, pp. 600-612, 2002.
- Kuroda, S. and Fowler, B. O. Compositional structural and phase changes in vitro laser irradiated human tooth enamel. *Calcified Tissue International*. Vol. 36, pp. 361-369, 1984.

- Kuramoto, M. Jr., Matson, E., Turbino, M. L. and Marques, R.A. Microhardness of Nd:YAG laser irradiated enamel surfaces. *Brazilian Dentistry Journal*. Vol. 12, No. 1, pp. 31-33, 2001.
- Kwon, Y. H., Lee, J-S., Choi, Y-H., Lee, J-M. and Song, K-B. Change of enamel after Er:YAG and CO₂ laser irradiation and fluoride treatment. *Photomedicine and Laser Surgery*. Vol. 23, No. 4, pp. 389-394, 2005.
- Lakshmi, A., Shobha, D. and Lakshminarayanan, L. and Chen, N. Prevention of caries by pulsed CO₂ laser pre-treatment of enamel: an in-vitro study. *Journal of the Indian Society of Pedodontics and Preventive Dentistry*. Vol. 19, No. 4, pp. 152-156, 2001.
- Leroy, N. and Bres, E. Structure and substitutions in fluorapatite. *European Cells and Materials*. Vol. 2, pp. 36-48, 2001.
- Lewis, R. Lasers in dentistry. FDA Consumer. U.S. food and drug administration. <http://www.fda.gov/bbs/topics/CONSUMER/CON00296d.html>, 1995.
- Li, Y., Wiliana, T. and Tam, K. C. Synthesis of amorphous calcium phosphate using various types of cyclodextrins. *Materials Research Bulletin*. Vol. 42, issue 5, pp. 820-827, 2007.
- Lin C-P., Tseng, Y-C., Lin, F-H., Liao, J-D. and Lan, W-H. Treatment of tooth fracture by medium-energy CO₂ laser and DP-bioactive paste: the interaction of enamel and DP-bioactive glasee during irradiation by CO₂ laser. *Biomaterials*. Vol. 22, pp. 489-496, 2001.
- Malmström, H. S., McCormack, S. M., Fried, D., and Featherstone, J. D. B. Effect of CO₂ laser on pulpal temperature and surface morphology: an in vitro study. *Journal of Dentistry*. Vol. 29, pp. 521-529, 2001.
- Mann, S. The biomimetics of enamel: a paradigm for organized biomaterials synthesis. *Dental Enamel*. Ciba Foundation Symposium 205, pp. 261-274, 1997.
- Markovic, M., Fowler, B. O. and Tung, M. S. Preparation and comprehensive characterization of a Calcium hydroxyapatite reference material. *Journal of Research of the National Institute of Standards and Technology*. Vol. 109, No. 6, pp. 553-568, 2004.
- Mathew, M. and Takagi, S. Structures of biological minerals in dental research. *Journal of Research of the National Institute of Standards and Technology*. Vol. 106, No. 6, pp. 1035-1044, 2001.
- McClellan, G. H. Mineralogy of carbonate fluorapatites. *Journal of the Geological Society*. Vol. 137, No. 6, pp. 675-681, 1980.
- McMillan, P. F. and Hofmeister, A. M. Infrared and Raman spectroscopy, in Hawthorne, F. C., (Ed), *Review in Mineralogy*. Vol. 18, no. 99, 1988.

- Meister, J., Franze, R. and Apel C. Influence of the spatial beam profile on hard tissue ablation, Part II: pulse energy and energy density distribution in simple beams. *Lasers in Medical Science*. Vol. 19, pp. 112-118, 2004.
- Meister, J., Franze, R. and Apel C. Influence of the spatial beam profile on hard tissue ablation, Part I: Multimode emitting Er:YAG lasers. *Lasers in Medical Science*. Vol. 18, pp. 112-118, 2003.
- Mercer, C. E. and Anderson, P. X-ray microtomography: a novel technique for the quantification of effects in enamel following CO₂ laser application. *British Dental Journal*. Vol. 180, No. 12, pp.451-455, 1996.
- Meurman, J. H., Hemmerle, J., Voegel, J-C., Rauhamaa-Mäkinen, R. and Luomanen, M. Transformation of hydroxyapatite to fluorapatite by irradiation with high-energy CO₂ laser. *Caries Research*. Vol.31, pp. 397-400, 1997.
- Nammour, S., Rocca, J.-P., Pireaux, J.-J, Powell, G. L., Morciaux, Y. and Demortier, G. Increase of enamel fluoride retention by low fluence argon laser beam: a 6-month follow-up study in vivo. *Lasers in Surgery and Medicine*. Vol. 36, pp. 220–224, 2005.
- Nelson, D. G. A., Shariati, M., Glena, R., Shields, C. P. and Featherstone, J. D. B. Effect of pulsed low energy infrared laser irradiation on artificial caries-like lesion formation. *Caries Research*. Vol. 20, pp. 289-299, 1986.
- Nelson, D. G. A., Wefel, J. S., Jongebloed, W. L. and Featherstone, J. D. B. Morphology, histology and crystallography of human dental enamel treated with pulsed low-energy infrared laser radiation. *Caries Research*. Vol. 21, pp. 411-426, 1987.
- Noel, L., Rebellato, J. and Sheats, R. D. The effect of Argon laser irradiation on demineralization resistance of human enamel adjacent to orthodontic brackets: an in vitro study. *Angle Orthodontist*. Vol. 73, No. 3, pp. 249-258, 2003.
- Obata, A., Tsumura, T., Niwa, K., Ashizawa, Y., Deguchi, T. and Ito, M. Super pulse CO₂ laser for bracket bonding and debonding. *European Journal of Orthodontics*. Vol. 21, pp. 193-198, 1999.
- Oesterle, L. J., Shellhart, W. C. and Belanger, G. K. The use of bovine enamel in bonding studies. *American Journal of Orthodontics and Dentofacial Orthopedics*. Vol. 114, No. 5, pp. 514-519, 1998.
- Oho, T. and Morioka, T. A possible mechanism of acquired acid resistance of human dental enamel by laser irradiation. *Caries Research*. Vol. 24, pp. 86-92, 1990.

- Palamara, J., Phakey, P. P., Orams, H. J. and Rachinger, W. A. The effect on the ultrastructure of dental enamel of excimer-dye, argon-ion and CO₂ lasers. *Scanning Microscopy*. Vol. 6, No. 4, pp. 1061-1071, 1992.
- Penel, G., Delfosse, C., Descamps, M. and Leroy, G. Composition of bone and apatitic biomaterials as revealed by intravital Raman microspectroscopy. *Bone*. Vol. 36, No. 5, pp. 893-901, 2005.
- Penel, G., Leroy, G., Rey, C. and Bres, E. MicroRaman spectral study of the PO₄ and CO₃ vibrational modes in synthetic and biological apatites. *Calcified Tissue International*. Vol. 63, pp. 475-481, 1998.
- Patel, A. R. and Damle, S. G. The effect of carbon dioxide laser on acid resistance of human tooth enamel: an evaluation by wet chemical analysis and scanning electron microscopy. *Journal of the Indian Society of Pedodontics and Preventive Ddentistry*. Vol. 14, No. 2, pp. 31-35, 1996.
- Pogrel, M. A., Muff, D. F. and Marshall, G.W. Structural change in dental enamel induced by high energy continuous wave carbon dioxide laser. *Lasers in Surgery and Medicine*. Vol. 13, pp. 89-96, 1993.
- Rode, A. V., Gamaly, E. G., Luther-Davis, B., Taylor, B. T., Graessel, M. Dawes, J. M., Chan, A., Lowe, R. M. and Hannaford, P. Precision ablation of dental enamel using a subpicosecond pulsed laser. *Australian Dental Journal*. Vol. 48, No. 4, pp. 233-239, 2003.
- Ross, M. H., Kaye, G. I. and Pawlina, W. *Histology: a text and atlas*, 4th edition. Publisher: Lippincott Williams and Wilkins; Baltimore, Maryland, 2002.
- Sakae, T., Suzuki, K. and Kozawa, Y. A short review of studies on chemical and physical properties of enamel crystallites. *Tooth Enamel Microstructure*. Chap. 2. Balkema, Rotterdam, 1997.
- Santaella, M. R. L. A., Braun, A., Matson, E. and Frentzen, M. Effect of diode laser and fluoride varnish on initial surface demineralization of primary dentition enamel: an in vitro study. *International Journal of Paediatric Dentistry*. Vol. 14, pp. 199-203, 2004.
- Santos, R. V. and Clayton, R. N. The carbonate content in high-temperature apatite: An analytical method applied to apatite from the Jacupiranga alkaline complex. *American Mineralogist*. Vol. 80, pp. 336-344, 1995.
- Sato, K. Relation between acid dissolution and histological alteration of heated tooth enamel. *Caries Research*. Vol. 17, pp. 490-495, 1983.
- Schouten, J. R. The effect of Argon laser irradiation on etched and pumiced human enamel: an in vitro study. Ph. D. thesis. West Virginia University. Morgantown, West Virginia, 1999.

- Schulze, K. A., Balooch, M., Balooch, G., Marshall, G. W. and Marshall, S. J. Micro-Raman spectroscopic investigation of dental calcified tissues. *Journal of Biomedical Materials Research*. Vol. 69A, No. 2, pp. 286-93, 2004.
- Schumacher, G. E., Antonucci, J. M., O'Donnell, J. N. R. and Skrtic, D. The use of amorphous calcium phosphate composites as bioactive basing materials: Their effect on the strength of the composite-adhesive-dentin bond. *Journal of American Dental Association*. Vol. 138, no. 11, pp. 1476-1484, 2007.
- Sfihi, H. and Rey, C. 1-D and 2-D double heteronuclear magnetic resonance study of the local structure of type B carbonate fluorapatite. *Magnetic Resonance in Colloid and Interface Science, NATO ASI Series II*. Vol. 76, pp. 409-422, 2002.
- Shahabi, S., Brockhurst, P. J. and Walsh, L. J. Effect of tooth-related factors on the shear bond strengths obtained with CO₂ laser conditioning of enamel. *Australian Dental Journal*. Vol. 42, No. 2, pp.81-84, 1997.
- Shellis, R.P. and Wilson, R. M. Apparent solubility distributions of hydroxyapatite and enamel apatite. *Journal of Colloid and Interface Science*. Vol. 278, pp. 325-332, 2004.
- Shi, J. From dental enamel to synthetic hydroxyapatite-based biomaterials. Ph. D. thesis. University of Hamburg, Germany, 2004.
- Shi, J., Klocke, A., Zhang, M. and Bismayer, U. Thermal behavior of dental enamel and geologic apatite: An infrared spectroscopic study. *American Mineralogist*. Vol. 88, pp. 1866-1871, 2003.
- Shi, J., Klocke, A., Zhang, M. and Bismayer, U. Thermally-induced structural modification of dental enamel apatite: Decomposition and transformation of carbonate groups. *European Journal of Mineralogy*. Vol. 17, pp. 769-775, 2005.
- Skinner, H. C. W. Biominerals. *Mineralogical Magazine*. Vol. 69, No. 5, pp. 621-641, 2005.
- Skrtic, D., Antonucci, J.M. and Eanes, E.D. Amorphous calcium phosphate-based bioactive polymeric composites for mineralized tissue regeneration. *Journal of Research of the National Institute of Standards and Technology*. Vol. 108, pp. 167-182, 2003.
- Stern, R.H., Sognnaes, R.F. Laser beam effect on dental hard tissues. *Journal of Dental Research*. Vol. 43, pp. 73-77, 1964.
- Subramanya, K. S., Higuchi, W. I., Yu, D. C. and Motimaya, A. Comparative pulpal temperature studies using three dental lasers. *Journal of Undergraduate Research, University of Utah*. Vol. 3, No. 1 pp. 46-50, 1992.

- Sydney-Zax, M., Mayer, I. and Deutsch, D. Carbonate content in developing human and bovine enamel. *Journal of Dental Enamel Research*. Vol. 70, No. 5, pp. 913-916, 1991.
- Tagomori, S. and Iwase, T. Ultrastructural change of enamel exposed to a normal pulsed Nd-YAG laser. *Caries Research*. Vol. 29, pp. 513-520, 1995.
- Tang, R., Henneman, Z. J. and Nancollas, G. H. Constant composition kinetics study of carbonatedapatite dissolution. *Journal of Crystal Growth*. Vol. 249, pp. 614-624, 2003.
- Tao, J., Pan, H., Zeng, Y., Xu, X. and Tang, R. Roles of amorphous calcium phosphate and biological additives in the assembly of hydroxyapatite nanoparticles. *Journal of Physical Chemistry B*, ASAP article 10.1021/jp0732918 S1520-6106(07)03291-9, 2007.
- Tepper, S. A., Zehnder, M., Pajarola G. F. and Schmidlin, P. R. Increased fluoride uptake and acid resistance by CO₂ laser-irradiation through topically applied fluoride on human enamel in vitro. *Journal of Dentistry*. Vol. 32, pp. 635-641, 2004.
- Timlin, J. A., Carden, A. and Morris, M. D. Raman spectroscopic imaging markers for fatigue-related microdamage in bovine bone. *Analytical Chemistry*. Vol. 72, pp. 2229-2236, 2000.
- Tokonabe, H., Kouji, R., Watanabe, H., Nakamura, Y. and Matsumoto, K. Morphological changes of human teeth with Er:YAG laser irradiation. *Journal of Clinical Laser Medicine and Surgery*. Vol. 17, No. 1, pp. 7-12, 1999.
- Tsai, C-L., Lin, Y-T., Huang, S-T. and Chang, H-W. In vitro acid resistance of CO₂ and Nd-YAG laser-treated human tooth enamel. *Caries Research*. Vol. 36, pp. 423-429, 2002.
- Tsuda, H. and Arends, J. Orientational micro-Raman spectroscopy on hydroxyapatite single crystals and human enamel crystallites. *Journal of Dental Research*. Vol. 73, No. 11, pp. 1703-1710, 1994.
- Tudor, A. M., Melia, C. D., Davies, M. C., Anderson, D., Hastings, G., Morrey, S., Domingos-Sandos, J. and Barbosa, M. The analysis of biomedical hydroxyapatite powders and hydroxyapatite coatings on metallic medical implants by near-IR fourier transform Raman spectroscopy. *Spectrochimica Acta*. Vol. 49A, No. 5/6, pp. 675-680, 1993.
- Üsümez, S., Orhan, M. and Üsümez, A. Laser etching of enamel for direct bonding with an Er,Cr:YSGG hydrokinetic laser system. *American Journal of Orthodontics and Dentofacial Orthopedics*. Vol. 122, No. 6, pp. 649-656, 2002.
- Walsh, L. J. The current status of laser applications in dentistry. *Australian Dental Journal*. Vol. 48, No. 3, pp. 146-155, 2003.

- Watanabe, I-S., Lopes, R. A., Brugnera, A., Katayama, A. Y. and Gardini, A. E. C. Effect of CO₂ laser on class V cavities of human molar teeth under a scanning electron microscope. *Brazilian Dental Journal*. Vol. 7, No. 1, pp. 27-31, 1996.
- Wen, S. L. Human enamel structure studied by high resolution electron microscopy. *Electron Microscopy Reviews*. Vol. 2, No. 1, pp. 1-16, 1989.
- Wentrup-Byrne, E., Armstrong, C. A., Armstrong, R. S. and Collins, B. M. Fourier transform raman microscopic mapping of the molecular components in a human tooth. *Journal of Raman Spectroscopy*. Vol. 28, pp. 151-158, 1997.
- Wheeler, C. R., Fried, D., Featherstone, J. D. B. and Watanabe, L. G. Irradiation of dental enamel with Q-switched 355nm laser pulses: surface morphology, fluoride adsorption, and adhesion to composite resin. *Lasers in Surgery and Medicine*. Vol. 32, pp. 310-317, 2003.
- Wikipedia, the free encyclopedia. Infrared spectroscopy. http://en.wikipedia.org/wiki/Infrared_spectroscopy, 2006.
- Willms, L., Herschel, A., Niemz, M. H. and Pioch, T. Preparation of dental hard tissue with picosecond laser pulses. *Lasers in Medical Science*. Vol. 11, pp. 45-51, 1996.
- Wilson, R. M., Elliott, J. C. and Dowker, S. E. P. Rietveld refinement of the crystallographic structure of human dental enamel apatites. *American Mineralogist*. Vol. 84, pp. 1406–1414, 1999.
- Wu, C.-C., Roan, R.-T. and Chen, J.-H. Sintering mechanism of the CaF₂ on hydroxyapatite by a 10.6- μ m CO₂ laser. *Lasers in Surgery and Medicine*. Vol. 31, pp. 333–338, 2002.
- Wu, Q. G. Oral pathology 3rd edition (in Chinese). People's health publishing house, P. R. China, 1979. 吴奇光, 《口腔组织病理学(第三版)》, 人民卫生出版社, 1979年7月.
- Yin, X. and Stott, M. J. α - and β -tricalcium phosphate: A density functional study. *Physical Review. B*. Vol. 68, 205205, 2003.
- Ying, D., Chuah, G. K. and Hsu, C-Y. Effect of er:YAG laser and organic matrix on porosity changes in human enamel. *Journal of Dentistry*. Vol. 32, pp. 41-46, 2004.
- Yu, D.-G., Kimura, Y., Fujita, A., Hossain, M., Kinoshita, J.-I., Suzuki, N. and Matsumoto, K. Study on acid resistance of human dental enamel and dentin irradiated by semiconductor laser with Ag(NH₃)₂F solution. *Journal of Clinical Laser Medicine and Surgery*. Vol. 19, No. 3, pp. 141–146, 2001.
- Zezell, D. M., Bonk, P. A., Salvador, V. L. R., Rossi, W., Ranieri, I. M., Bachmann, L., Eduardo, C. P., Vieira, N. D. Jr., and Morato, S. P. Combined effect of Holmium laser and

Fluoride in prevention of dental caries 'in vitro'. *Revista de Fisica Aplicada e Instrumentacao*. Vol. 13, No. 2, pp. 21-23, 1998.

Zezell, D. M., Cecchini, S. C. M., Eduardo, C. P., Matsumoto, K., Rossi, W., Nogueira, G. E. C., Berretta, J. R., Viera, N. D. and Morato, S. Experimental studies of the applications of the holmium laser in dentistry. *Journal of Clinical Laser Medicine and Surgery*. Vol. 13, No. 4, pp. 283-289, 1995.

Zuerlein, M. J., Fried, D. and Featherstone, J. D. B. Modeling the modification depth of carbon dioxide laser-treated dental enamel. *Lasers in Surgery and Medicine*. Vol. 25, pp. 335-347, 1999.

Zuerlein, M. J., Fried, D., Featherstone, J. D. B. and Seka, W. Optical properties of dental enamel in the mid-IR determined by pulsed photothermal radiometry. *IEEE Journal of Selected Topics in Quantum Electronics*. Vol. 5, No. 4, pp. 1083-1089, 1999.

Acknowledgements

The work submitted in this dissertation had been done at the Mineralogy and Petrography Institute of the University of Hamburg during the period of Aug. 2004 to Oct. 2007.

I would like to thank Prof. Dr. Ulrich Bismayer, my supervisor, for his guidance. From the very beginning of this work to the end of dissertation, he gave the key idea and pointed out the right direction of this exploring research. Without him, no promising result could have been achieved. Besides the help in the academic field, he also gave me great help to live in the city of Hamburg.

I am also grateful to Prof. Dr. Arndt Klocke, my second supervisor from the University Hospital Eppendorf, for his great ideas, helpful discussion and materials supplied for my research.

I also would like to thank the following persons or organizations for their help:

Prof. Dr. Boriana Mihailova, Mineralogy and Petrography Institute of University of Hamburg, for her excellent lectures and her continuous help in Raman and Infrared spectroscopic analysis and results discussions.

Dr. Peter Henriot and Dr. Bodo Ritschel, Zahnärztliche Gemeinschaftspraxis, for the access to the dental laser instruments.

Dr. Biliana Gasharova, ANKA/Institute for Synchrontron Radiation, Forschungszentrum Karlsruhe, for his help in the samples analysis.

Dr. Rainer Stosch and Dr. Bernd Güttler, Physikalisch-Technische Bundesanstalt, Braunschweig, for their help with Raman spectroscopy.

Mr. Joachim Ludwig, Mineralogy and Petrography Institute of the University of Hamburg, for the powder X-ray diffraction measurements.

Dr. Jochen Schlüter, Mineralogical Museum of the University of Hamburg, for offering good geological samples.

Mr. Peter Stutz, Mineralogy and Petrography Institute of the University of Hamburg, for the preparation of specimens.

Mrs. Stefanie Heidrich, Mineralogy and Petrography Institute of the University of Hamburg, for her help in electronic microprobe analysis.

The Graduate School “Design and Characterization of Functional Materials” for offering me one and a half year funding to survive in Hamburg.

Mr. Reinhardt Kurtz, Dr. Carsten Paulmann, Mrs. Regine Köllner and other students and staff members of the Mineralogy and Petrography Institute who have created a helpful and friendly atmosphere during my stay.

and all those not mentioned here but also helped me with my work.

Curriculum Vitae

Family Name: Zhang
First name: Shengqiang
Gender: male
Date of birth: May 05, 1966
Place of birth: Heilongjiang Province, China
Nationality: Chinese
Email: Mica001@mineralogie.uni-hamburg.de
Zhang_shengqiang@hotmail.com

Educations:

- Aug. 2004-Oct. 2007 Ph. D. student, Mineralogy and Petrography Institute, University of Hamburg, Hamburg, Germany.
Title of the thesis: CO₂ laser induced structural changes of dental enamel.
- Oct.1998 ~ Jun. 2001 Master student of Environmental Chemistry, Turku University (Master thesis in Laboratory of Analytical Chemistry, Åbo Akademi University), Turku, Finland.
Title of the thesis: Use of birch sap as bio-indicator of environmental pollution.
- Sep. 1984 ~ Jul. 1988 Bachelor student of science at the Technical Physics Department, majoring in Applied Chemistry, Peking University, Beijing, China.
Title of thesis: Design of a non-power-driven ozone sampler.

Work experiences:

- Jul.1988 ~ Jun.1992 Analyst and researcher of Daqing City Environmental Protection Bureau, China, monitoring the air and physical pollution and carrying out environmental research.
- Jun.1992 ~ Sep.1998 Deputy Director of Small Enterprise Incubator, Daqing High-Tech industry Developing Zone, China, in charge of incubating small enterprises by means of new technology, employee training and technological research.

- Jun.1997 ~ Nov.1997 Researcher in a Personnel Exchange Programmed between the Finnish and Chinese Government. Worked at Environmental Research Institute----Väkipyörä Ltd. in Vaasa, Finland, analyzing the present situation of environment and energy, the existing policies on the relevant aspects in China. Presented a report of 'Market Research on Energy and Environment in China' as preliminary references.
- Oct. 1998 ~ Jun. 2001 Master student of University of Turku, Master thesis work in Laboratory of Analytical Chemistry, Åbo Akademi University, Turku, Finland
- Dec. 2000 ~ Oct. 2001 Working as a laboratory assistant in the Combustion and Materials Research Group, Åbo Akademi University. Black Liquor research, Finland.
- Nov. 2001 ~ Jul. 2002 Non-degree student at Åbo Akademi University, Chemistry Faculty, Finland
- Sep. 2002 ~ Nov. 2002 Guest researcher, 'plant fibre reinforced cement project', Built Environment Center, University of Gävle, Sweden
- Dec. 2002 ~ Apr. 2003 Laboratory assistant, Electrical conductive polymer research, Analytical Chemistry laboratory, Åbo Akademi University, Finland
- Aug. 2004 ~ Ph.D. student of Graduate school GK 611 'Design and characterization of functionalized materials', Hamburg, Germany

Academic activities since 2004:

- Feb. 2005 Jahrestagung der DGK & DGKK und NKK-ÖAW in Köln 2005, Köln, Germany,
Poster presentation: Laser Treatment of Dental Enamel for Orthodontics Bonding
- Feb. 2005 Meeting of reviewing graduate school GK 611 'Design and characterization of functionalized materials' by DFG, Hamburg
Poster presentation: Laser Treatment of Dental Enamel in Orthodontics
- Jun. 2005 Semester seminar of GK 611 'Design and characterization of functionalized materials'
Oral presentation: Laser Treatment of Dental Enamel in Orthodontics

- Jan. 2006 Group Seminar of Mineralogy and Petrography Institute, University of Hamburg.
Oral Presentation: Laser induced structural changes in dental enamel
- Apr. 2006 Jahrestagung der Deutschen Gesellschaft für Kristallographie 2006, Freiburg
Oral presentation: Laser-Induced Structural changes in Dental Enamel
- Aug. 2006 23rd European Crystallographic Meeting ECM23, Leuven, Belgium
Poster presentation: U. Bismayer B. Mihailova, S. Zhang, A. Klocke and B. Gasharova. Thansition of Laser-Treated Dental Enamel
- Sep. 2006 84th annual meeting of the German Mineralogical Society (DMG), Hannover, Germany.
Poster presentation: U. Bismayer B. Mihailova, S. Zhang, A. Klocke and B. Gasharova. CO₂ laser-irradiated dental enamel: A spectroscopic study
- Oct. 2006 Block Seminar of GK 611 'Design and characterization of functionalized materials'
Weißenhäuser Strand.
Oral presentation: Laser treatment parameters and their influence on Dental Enamel
- Oct. 2006 Klocke, A.; Mihailova, B.; Zhang, S.; Gasharova, B.; Stosch, R.; Güttler, B.;Henriot, P.; Ritschel, B.; Bismayer, U. CO₂ laser-induced zonation in dental enamel: a Raman and IR micro-spectroscopic study. Journal of Biomedical Materials Research: Part B: 81 (2007), 2, 499 - 507